

6

The Midsummer drought in the MOHC CMIP6 experiments

This chapter investigates the mechanisms associated with the bimodal seasonal cycle of precipitation, also known as Midsummer drought (MSD), of southern Mexico and Central America using CMIP6 experiments produced by the Met Office Hadley Centre. The chapter evaluates three relevant aspects of the seasonal cycle that are key for the MSD, according to the literature: SST and cloud-radiative feedbacks, the double crossing of the solar declination angle and the moisture transport associated with the Caribbean Low-level Jet (CLLJ). The wavelet transform method, introduced in the previous chapter, is used to evaluate the timings of the monsoon in the region and characterise the physical changes that are relevant for the MSD.

6.1 Introduction

A bimodal signal in the climatological seasonal cycle of precipitation has been documented in several regions of southern Mexico, Central America and the Caribbean; most commonly referred to as Midsummer drought (MSD Mosiño and García, 1966; Magaña et al., 1999; Gamble et al., 2008; Perdigón-Morales et al., 2018; Zhao et al., 2020). In spite of several decades of research, a clear depiction of the physical mechanisms that cause the two-peak

structure of precipitation remains elusive. Section 2.3 summarises the extensive literature on the mechanisms for the MSD, concluding that all the proposed mechanisms have shortcomings and have received criticism that question the extent to which these theories can explain the spatial and temporal variability of the bimodal signal in the seasonal cycle of precipitation.

Moreover, most global climate models from the CMIP5 cohort struggle to reasonably reproduce the seasonal cycle of precipitation in the region (Rauscher et al., 2008; Ryu and Hayhoe, 2014) which has limited their use to better understand these mechanisms and leading other studies to focus on regional models (Fuentes-Franco et al., 2015; Cavazos et al., 2020). Little attention has been given as to why some GCMs reproduce the bimodal seasonal cycle; for instance, Ryu and Hayhoe (2014) analysed how biases in large-scale features of CMIP3/5 models such as the North Atlantic Sub-tropical High could influence the representation of the MSD. Chapters 4 and 5 show that the CMIP6 MOHC simulations reproduce the timings and strength of the bimodal signal of precipitation with reasonable skill (Figure 6.1), albeit with a stronger first peak and a later onset of the MSD.

This chapter aims, firstly, to improve our understanding of the physical mechanisms associated with the 'real world' MSD of southern Mexico and northern Central America, also referred to as Mesoamerica. A second purpose of this chapter is to diagnose relevant processes that the CMIP6 MOHC accurately simulate in order to capture the seasonal cycle of precipitation. For this purpose, the wavelet transform (WT) method introduced in the previous chapter is used to separate the different stages of the rainy season in Mesoamerica in order to capture the dynamic and thermodynamic changes that occur during the seasonal cycle.

Three leading hypotheses (section 2.3) are investigated for the MSD of southern Mexico and Central America: the SST-cloud-radiative feedback proposed by Magaña et al. (1999), the solar declination angle hypothesis (Karnauskas et al., 2013) and the CLLJ as a modulator for moisture transport and convective activity in Mesoamerica (Herrera et al., 2015; Zermeño-Díaz, 2019). The main features of the three mechanisms are illustrated in Figure 6.2. Briefly, the cloud-radiative feedback mechanism (Fig. 6.2a) proposes that the peaks and trough of precipitation in the seasonal cycle are a result of a similar seasonality in the East Pacific SSTs and surface humidity. During the first peak of precipitation, cloud radiative effects

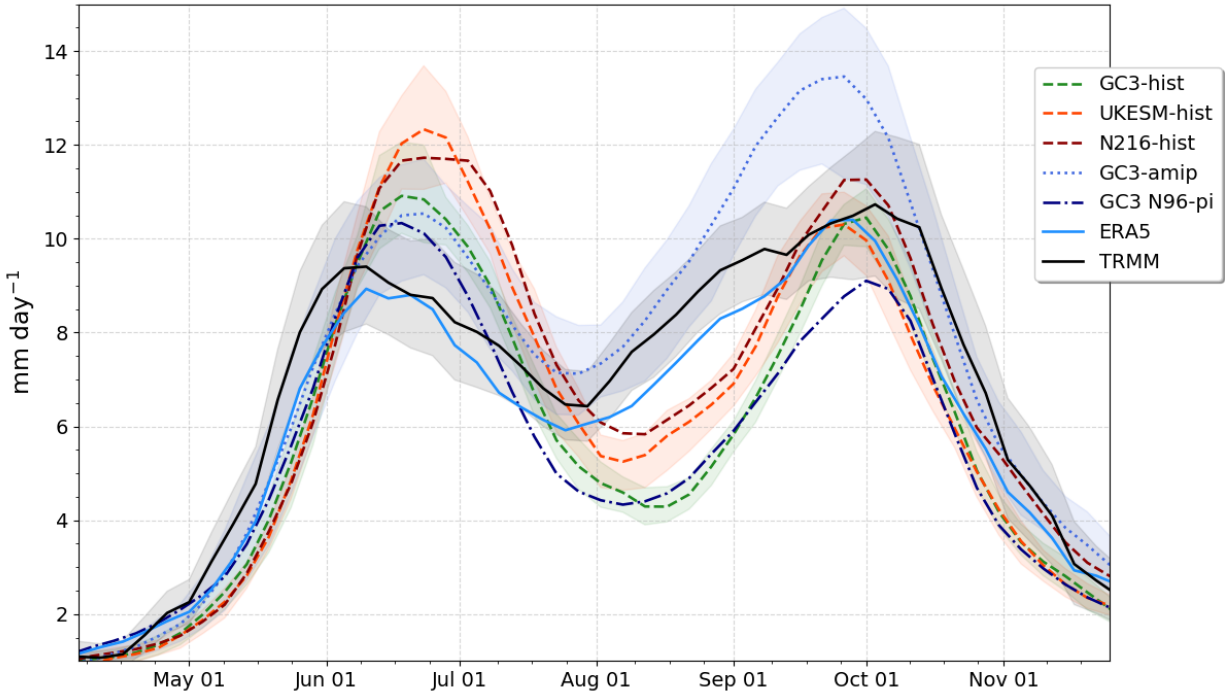


Figure 6.1: Pentad-mean precipitation in southern Mexico and northern Central America [95–86°W, 11–19°N]. The shading for the TRMM dataset is a measure of observational uncertainty obtained by bootstrapping the interannual variability whereas the shading for the CMIP6 experiments show the ensemble spread where multiple ensemble members were available.

block shortwave solar radiation from reaching the surface in addition to increased latent heat fluxes from the ocean to the atmosphere cooling the SSTs and leading to a decrease in convective activity and precipitation in the MSD. During this drier period, incoming shortwave increases again and raises East Pacific SSTs above 29°C and surface humidity leading to the second peak of precipitation.

The solar declination angle hypothesis (Fig. 6.2b) argues that total shortwave radiation absorption at the surface is the key element that controls the surface energy balance and the strongest control of the seasonal cycle of incoming shortwave is the solar declination angle. The total shortwave absorption by the surface modifies the surface moist static energy, specifically the surface moisture, which in this framework is the ultimate control of precipitation. In Central America, the solar declination angle crosses twice during the summer, once at the start and once at the end, and evidence by Karnauskas et al. (2013) suggests that precipitation follows the solar declination angle and surface moist

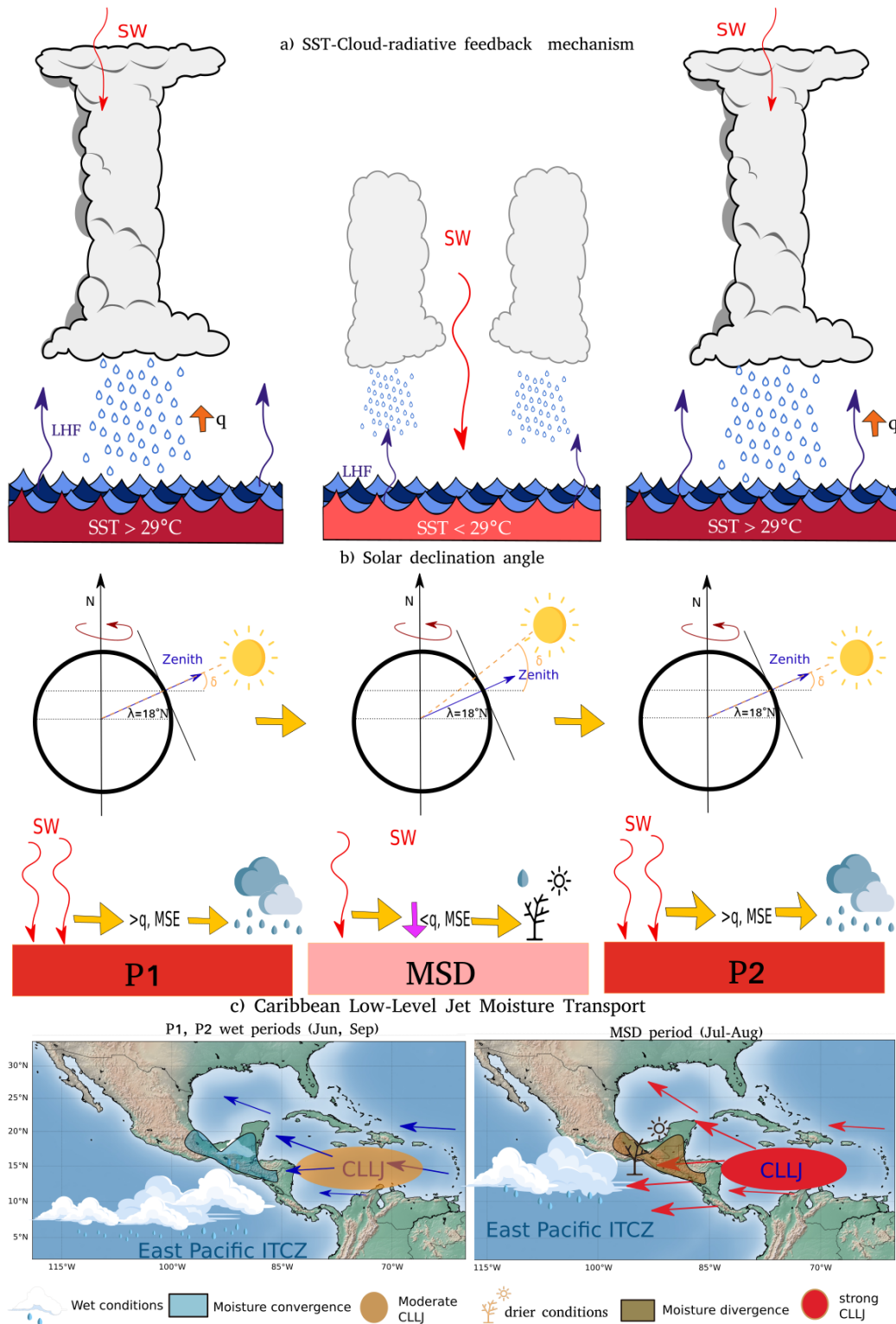


Figure 6.2: Schematic of the three mechanisms analysed in this chapter, a) the SST cloud-radiative mechanism, (b) the solar declination angle and (c) the moisture divergence mechanism driven by the CLLJ.

static energy with a lag of a few weeks.

Finally, the third mechanism investigated in this chapter argues that the seasonal cycle of the CLLJ, possibly influenced by the seasonal variations to the North Atlantic Subtropical High, modifies moisture transport in the region (Fig. 6.2c). In particular, studies have noted that the increase in the jet strength at the midsummer coincides with a reduction of rainfall over mainland, the MSD. This argument appears more frequently in studies to explain the MSD of the Caribbean (Martinez et al., 2019), but suggestions have also been made that the CLLJ variations could control the total moisture transport over the continent (Herrera et al., 2015). Specifically, the hypothesis is that during the MSD the strengthening of the CLLJ decreases the convergence of moisture over the continent and the total water content over western Central America, which ultimately explains the slight decrease in precipitation.

These hypotheses are tested in the newest reanalysis of ECMWF (ERA5) and in a subset of CMIP6 experiments with different representations of the MSD seasonal cycle (Figure 6.1). Furthermore, a moist static energy budget framework is implemented, toward the end of the chapter, to determine whether this methodology can provide new insight into the mechanisms that drive variability of precipitation within the rainy season.

The remainder of this chapter is presented as follows. Section 2 describes the observational data and the CMIP6 experiments used in this chapter and an overview of how the WT method is implemented to diagnose the timings of MSD. Then, section 3 evaluates the representation of the key features of the regional climate in the CMIP6 experiments and in ERA5. Then, the roles of the East Pacific SSTs (section 4), cloud-radiative effects and surface shortwave absorption (section 5) and the CLLJ and moisture transport (section 6) are investigated using composite and regression analysis. Finally, a short investigation of the MSD using the moist static energy budget is given in section 7. A summary and discussion is presented in the final section of this chapter.

6.2 Data and methods

6.2.1 Observations and reanalysis data

All the data used in this chapter are described in chapter 3. In particular, this chapter uses the gridded precipitation datasets of TRMM and CHIRPS. However, the main precipitation dataset will be the reanalysis ERA5. The remaining diagnostics are taken from ERA5 at the 0.75° resolution and for the period 1979-2019. ERA5 precipitation data is used throughout this chapter to compare against the models, and not observed datasets, because of two reasons. Firstly, observational (satellite or surface station) data of all diagnostics are not available on long periods at the daily resolutions required for this study, for example of the wind flow or moisture profiles over the ocean region. Secondly, ERA5 precipitation in the MSD region closely follows TRMM and CHIRPS (Fig. 6.1), and the previous chapter shows that ERA5 reasonably reproduces the mean timings for the MSD compared to TRMM and CHIRPS. Therefore, ERA5 can be compared to the simulations as another model; one that is more realistic as the reanalysis is partially driven by the observed state of the atmosphere through the assimilations of radiosondes taken in the region as well as satellite data of various quantities (Hersbach et al., 2020).

6.2.2 CMIP6 data

This chapter uses the output from realizations of the HadGEM3 GC3.1 run at two resolutions at N96 and N216 and from UKESM1. These experiments are described in section 3.2.2 and summarised in Table 3.2. This chapter follows the terminology and acronyms outlined in section 3.2.2. In addition to the pre-industrial, AMIP, and historical experiments used in previous chapters, this chapter uses experiments from the Cloud-Feedback MIP (CFMIP) (Webb et al., 2017) and ScenarioMIP (O'Neill et al., 2016) activities of CMIP6 (see Table 3.2). These are the GC3-amip lwoff, amip-p4K and amip-m4K from CFMIP, all run at N96 resolution for HadGEM3, and SSP1, SSP2 and SSP5 from the ScenarioMIP for UKESM1, HadGEM3 N96 and N216.

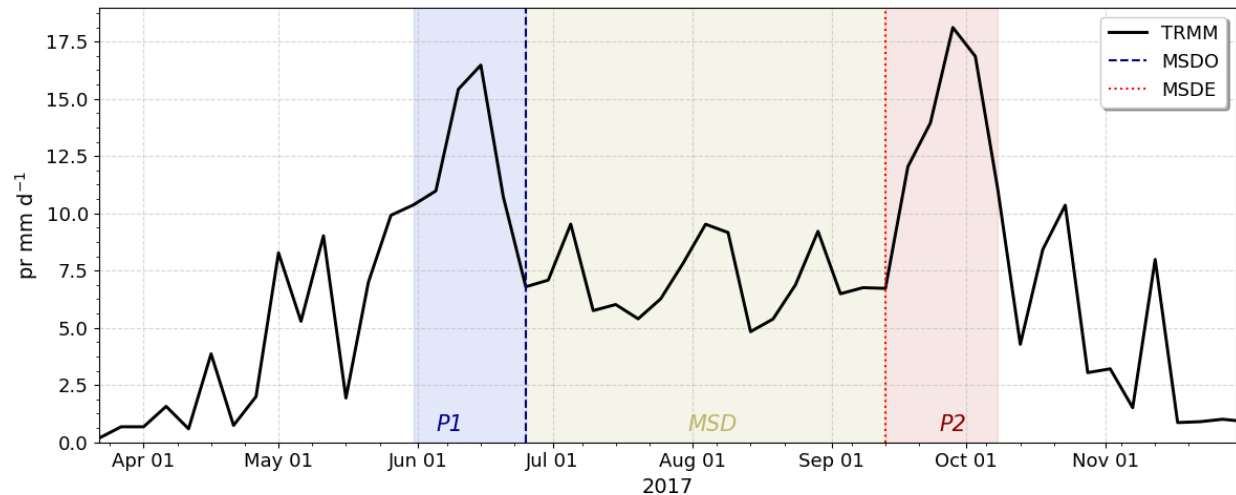


Figure 6.3: Pentad-mean precipitation averaged over the study region [95-86°W, 11-19°N] in the TRMM dataset for the summer of 2017. The timings of the onset (MSDO) and end (MSDE) of the MSD, as well as the first (P1) and second (P2) peak periods and the MSD periods are highlighted.

6.2.3 Determination of the timings of the MSD

Chapter 5 describes a wavelet transform (WT) method that can determine the timings of the MSD in observational gridded datasets, reanalysis and climate model precipitation time-series. This chapter uses the WT method to determine the onset (MO) and retreat (MR) of the monsoon rainy season, as well as the onset (MSDO) and end (MSDE) of the MSD.

To summarise MO and MR are determined by the maximum and minimum sum of WT coefficients computed from a dilation scale vector ranging from 24 to 54 pentads. After MO and MR are determined, a second WT is computed with dilation scales from 10 to 24 pentads and the minimum sum of the WT coefficients corresponds to the onset of the MSD and the maximum to the end of the MSD (MSDE). Similarly, the timings of the first (P1) and second (P2) peaks of precipitation are determined from the results of the WT method: P1 is defined as the period between the MSDO and the preceding 4 pentads or 20 days, whereas the second peak is defined as the period between the date of MSDE and the subsequent 4 pentads. An example of this separation of the MSD timings for each year is given in Figure 6.3, for precipitation observed from TRMM in 2017 over the study region.

The area of study of this chapter is in southern Mexico and northwestern Central America (depicted in Figure 6.4) a region with strong and robust MSD signals (see Chapter 5). The

WT method was applied to the TRMM, CHIRPS and ERA5 datasets and in the model precipitation time-series area-averaged over the study region.

6.3 Climatological features

The seasonal cycle of precipitation in the MSD region (Figure 6.1) is reasonably well simulated by the CMIP6 experiments and by ERA5, as shown in previous chapters. The two-peak structure of the MSD is observed in TRMM and ERA5 as two precipitation maxima, the first peak found during early to mid-June and the second peak at the end of September, separated by a drier period that spans from late June to late August. The precipitation in ERA5 not only closely follows the precipitation variations at the pentad scale but also generally agrees

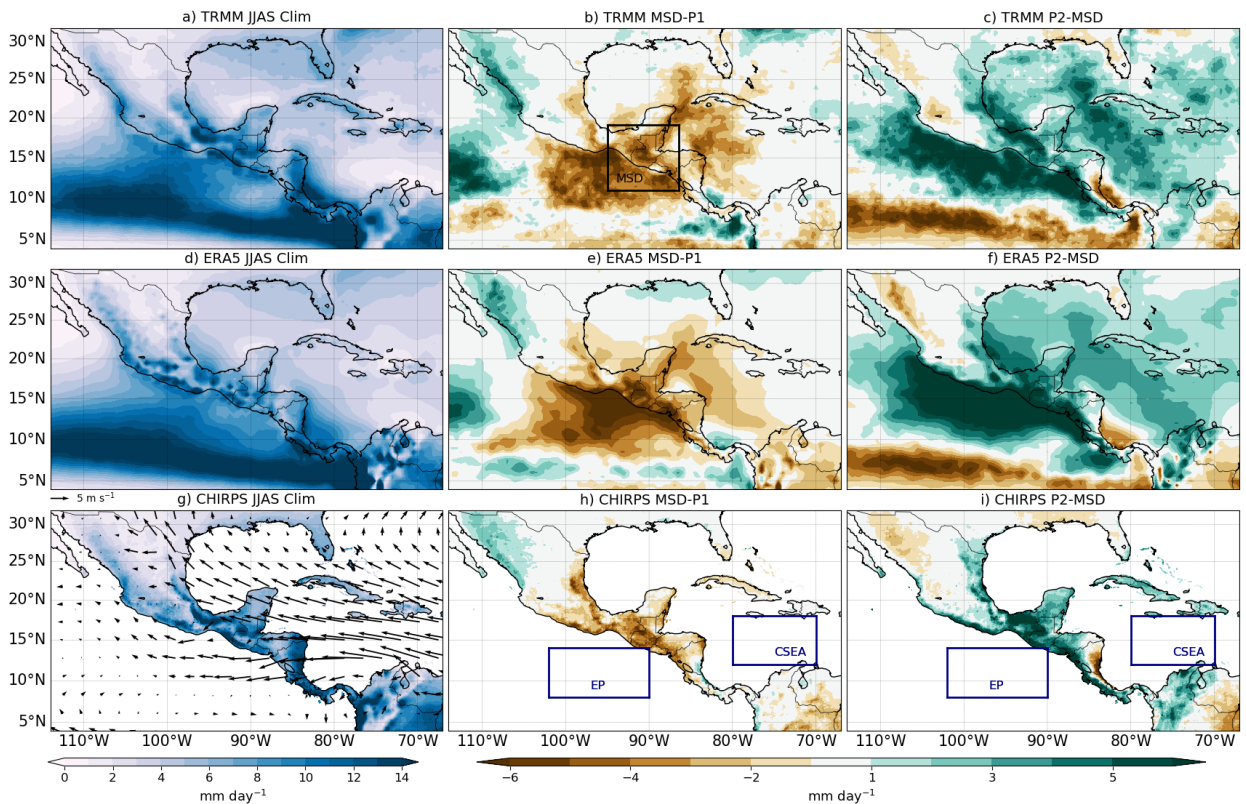


Figure 6.4: (a, d, g) Climatological JJAS rainfall and the difference between (b, e, h) the midsummer drought and the first peak (MSD-P1) periods and (c, f, i) between the second peak and the midsummer drought (P2-MSD) periods for (a-c) TRMM, (d-f) ERA5 and (g-i) CHIRPS. The climatological low-level winds (at 850 hPa) for JJAS in ERA5 are shown in c). The boxes in panels b, h and i show the definitions of the MSD, EP and CSEA regions that are used throughout this chapter.

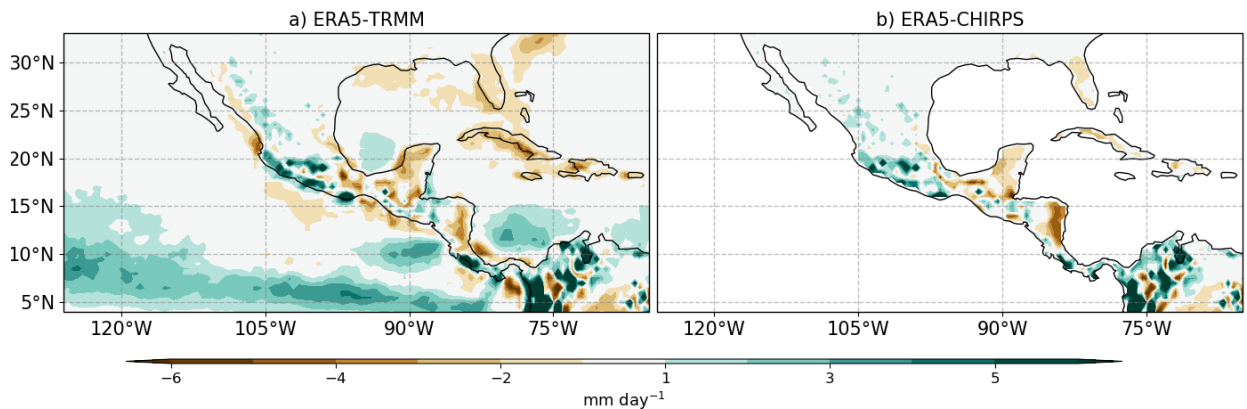


Figure 6.5: (a, b) JJAS precipitation biases in ERA5 when compared to (a) TRMM and (b) CHIRPS.

with the mean precipitation rate during the first peak, the MSD and second peak periods.

The MSD period in the CMIP6 experiments is observed one or two pentads after TRMM and ERA5 (see the mean values in the previous chapter) and shows a stronger variation of precipitation between the first peak and the Midsummer. A noteworthy difference is that the timing of the MSD is better represented in GC3-amip, particularly the MSDE date, suggesting a role for the SST variability or biases being relevant. In general, the pre-industrial control experiments show a higher magnitude of precipitation during the first peak and the MSD period whereas GC3-amip experiments are characterized by a wetter second peak.

The climatological distribution of precipitation and the temporal differences within the MSD timings in ERA5 agrees well with TRMM and CHIRPS (Figure 6.4). ERA5 reasonably captures the climatology of precipitation over land in Mesoamerica but also captures the strength and position of the East Pacific ITCZ, as shown by the precipitation maximum in the easternmost Pacific (panels a, d). Specifically, the biases of JJAS-mean precipitation in ERA5 are shown in Figure 6.5. While positive biases are found over the East Pacific Ocean, negative (weaker) biases are found over land in southern Mexico and Central America.

The patterns of the MSD-P1 and P2-MSD differences in ERA5 (Fig. 6.4) also agree well with TRMM. These two panels show that precipitation differences associated with the MSD measured by the area-averaged precipitation within the box in Figure 6.4b extends outside of the study region all over the Intra-Americas Seas comprising the easternmost Pacific Ocean, the entrance to the Gulf of Mexico and western Caribbean Sea, particularly

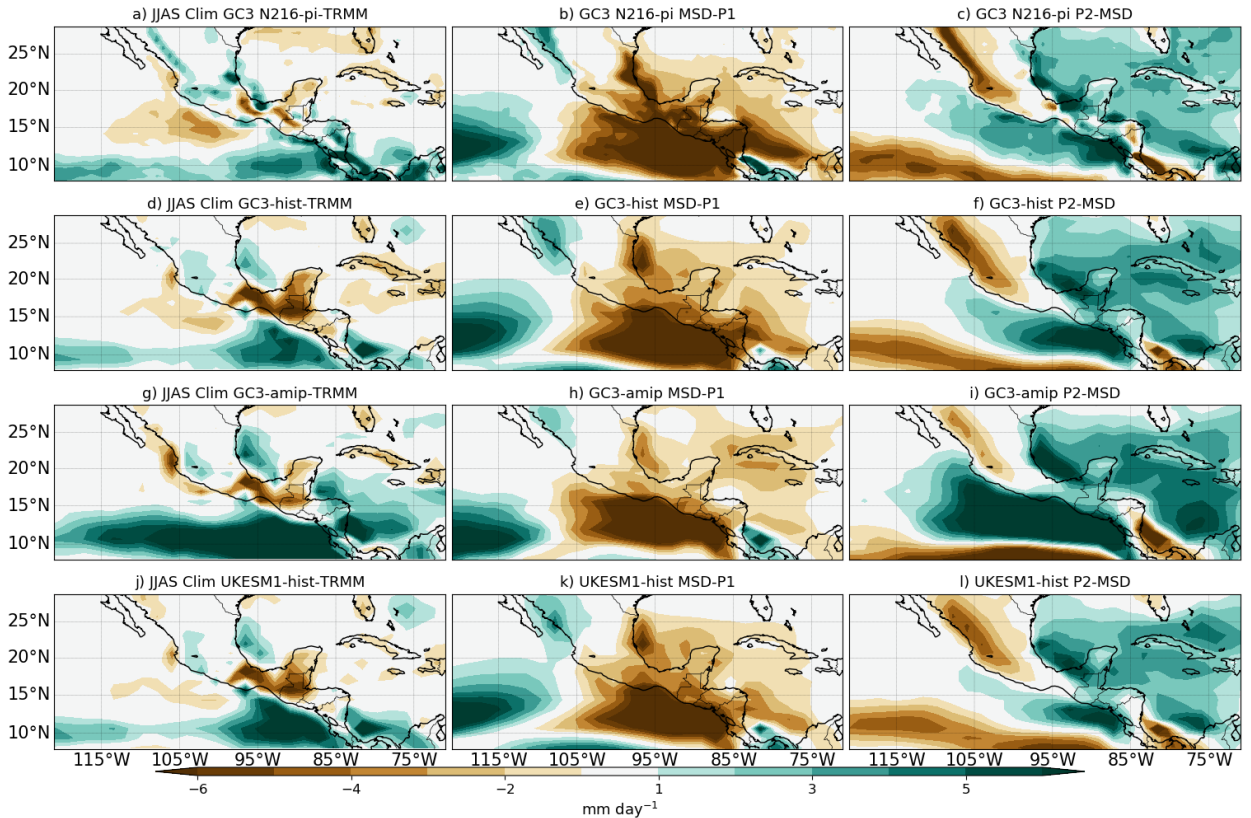


Figure 6.6: (a, d, g, j) JJAS model bias compared to TRMM and the difference between (b, e, h, k) the midsummer drought and the first peak periods and (c, f, i, l) between the second peak and the midsummer drought periods for four different simulations.

in the P2-MSD panel. Notably, the strongest differences for both panels are found on the western coast of Mesoamerica.

In turn, the simulations (Figure 6.6) have important biases in the magnitude of the precipitation in the East Pacific ITCZ with a positive bias of $3\text{--}6 \text{ mm day}^{-1}$ depending on the simulation as well as a dry bias over southern Mexico and Central America, as shown in chapter 4. These biases are much larger than the biases between ERA5 and TRMM and CHIRPS. The simulations capture the spatial patterns associated with the MSD stages, which also show the strongest differences are found on the west coast of the Mexican state of Chiapas, Guatemala and El Salvador. The negative differences in the MSD-P1 and positive differences in the P2-MSD extend to the Caribbean Sea, northeastern Mexico and the Gulf of Mexico. In agreement, with ERA5 and TRMM, the simulations show that the precipitation differences in the MSD region are always opposite to that of the North

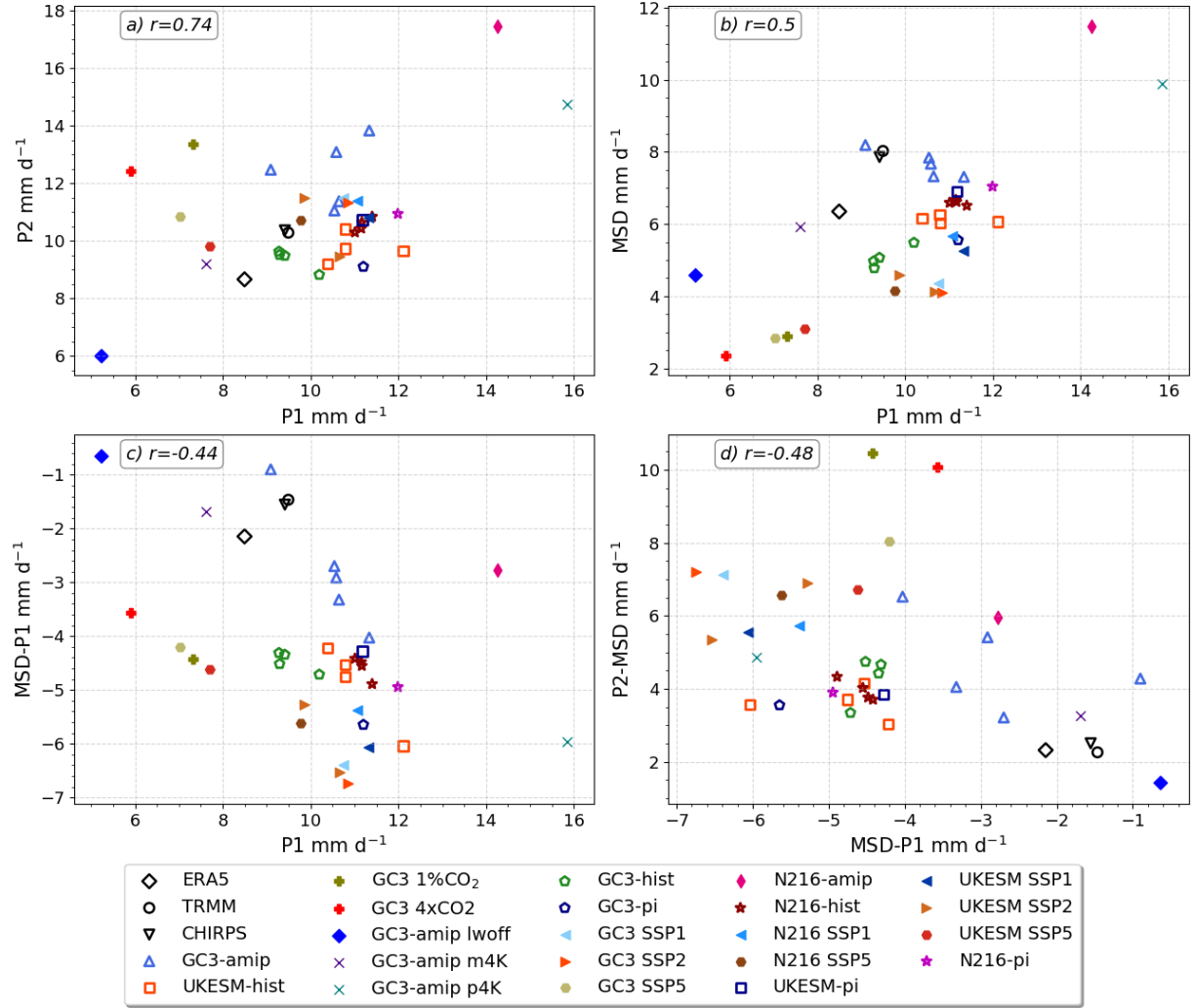


Figure 6.7: (a, b) Scatter plots of the mean values of precipitation [mm day^{-1}] for TRMM, ERA5, CHIRPS and the CMIP6 experiments (see 6.2.2) during the first peak (P1), the MSD and the second peak (P2) periods and (c, d) the precipitation differences between the three periods. The region used for this averages if illustrated in Figure 6.4.

American monsoon region, e.g., in Figures 6.4 and 6.6 the North American monsoon is wetter when the MSD period begins and Mesoamerica is drier.

The mean rainfall observed in the three periods (P1, P2 and the MSD) in the simulations varied notably between experiments done with different model configurations and with external forcing (Figure 6.7). The scatter of the first and second peak and the MSD mean rainfall rates shows, first, that the mean rainfall in each stage is not linearly related to another, i.e., a larger magnitude of the first peak of precipitation does not necessarily imply a wetter or drier MSD period. The atmosphere-only runs, GC3-amip, is a good example

of this behaviour as the mean rainfall during P1 is roughly the same as in the rest of the simulations but the mean rainfall during the MSD is slightly larger than in the rest of the simulations and the P2 precipitation is largest in GC3-amip.

Second, the magnitude of the first decrease in rainfall (MSD-P1) and the late-summer increase (P2-MSD) also show a significant spread amongst experiments, which also suggest that there is no clear association between the magnitude of the MSD and the magnitudes of the two peaks of precipitation in these simulations. The scatter of ERA5 in all panels is notably close to that of TRMM and CHIRPS, which is further evidence that the timings and strength of the MSD is well represented by this reanalysis. In contrast, the high resolution atmosphere-only run (N216-amip) shows the highest bias in precipitation throughout the three stages of the wet season. This result is noteworthy because this configuration uses the medium-resolution atmosphere and ocean, i.e., a higher resolution than GC3 amip and is forced by observed SSTs, the simulation cannot capture the observed precipitation rates and is strikingly the worst simulation overall.

The outgoing long-wave radiation (OLR) and vertical velocity (ω at 500 hPa) differences associated with the MSD were computed using the WT method for each dataset (Figure 6.8). These composite results also show that the MSD is not a local-scale feature but convective activity varies coherently in neighboring regions. From the first peak period to the MSD, OLR and ω , increase notably in the easternmost Pacific, southern Mexico and northern Central America and extend into the Caribbean islands and Sea, and in the case of OLR into the North Atlantic; because ω is defined as $\omega = DP/Dt$ these positive anomalies are indicative of weaker convection.

In contrast, two regions show opposite responses to the MSD. A region several degrees west of land (125°W) and another region north of the study region, i.e., the North American monsoon region, show signs of negative OLR and ω anomalies, in the MSD-P1 panels. These negative anomalies are indicative that, simultaneously to the onset of the MSD, convection is observed stronger and deeper in the North American Monsoon region and in the Pacific region west of the continent; the stronger convection found at around 125°W was also described by Herrera et al. (2015).

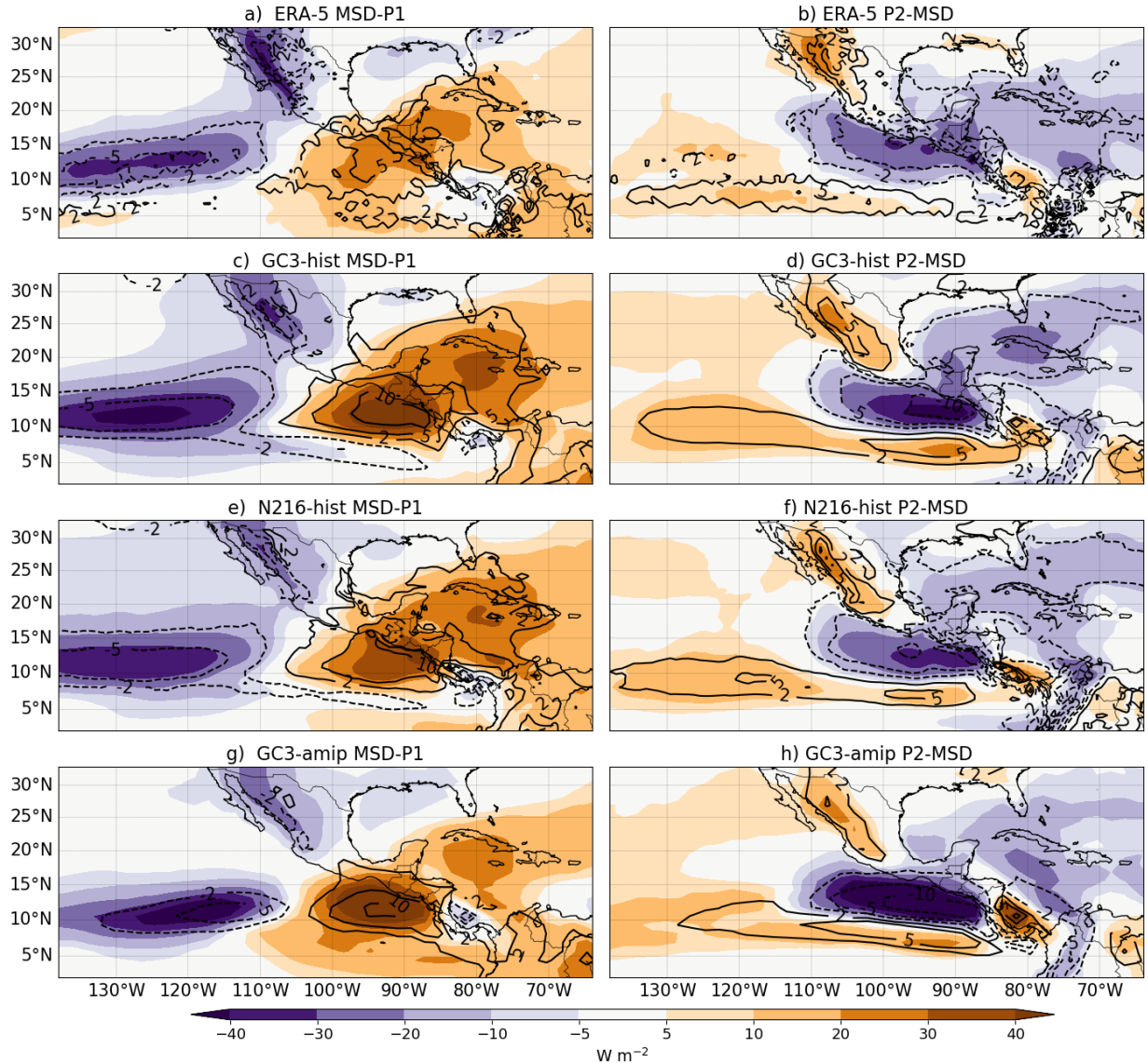


Figure 6.8: Outgoing long-wave radiation (OLR) [W m^{-2}] (shaded) and ω 500-hPa [$10^{-2} \text{ Pa s}^{-1}$] (line contours) differences between the MSD and first peak and the second peak and MSD.

The OLR and ω variations associated with the end of the MSD show a relatively opposite picture to the MSD-P1 differences (Fig. 6.8). OLR and ω decrease all across the central and south western coast of Mexico and northern Central America extending into the Caribbean Sea whereas positive differences are found in the North American Monsoon region and in the Pacific Ocean at around 125°W. These composites agree with the results of Herrera et al. (2015) that argues that ascending and descending anomalies in the MSD are closely related to ascent and descent elsewhere.

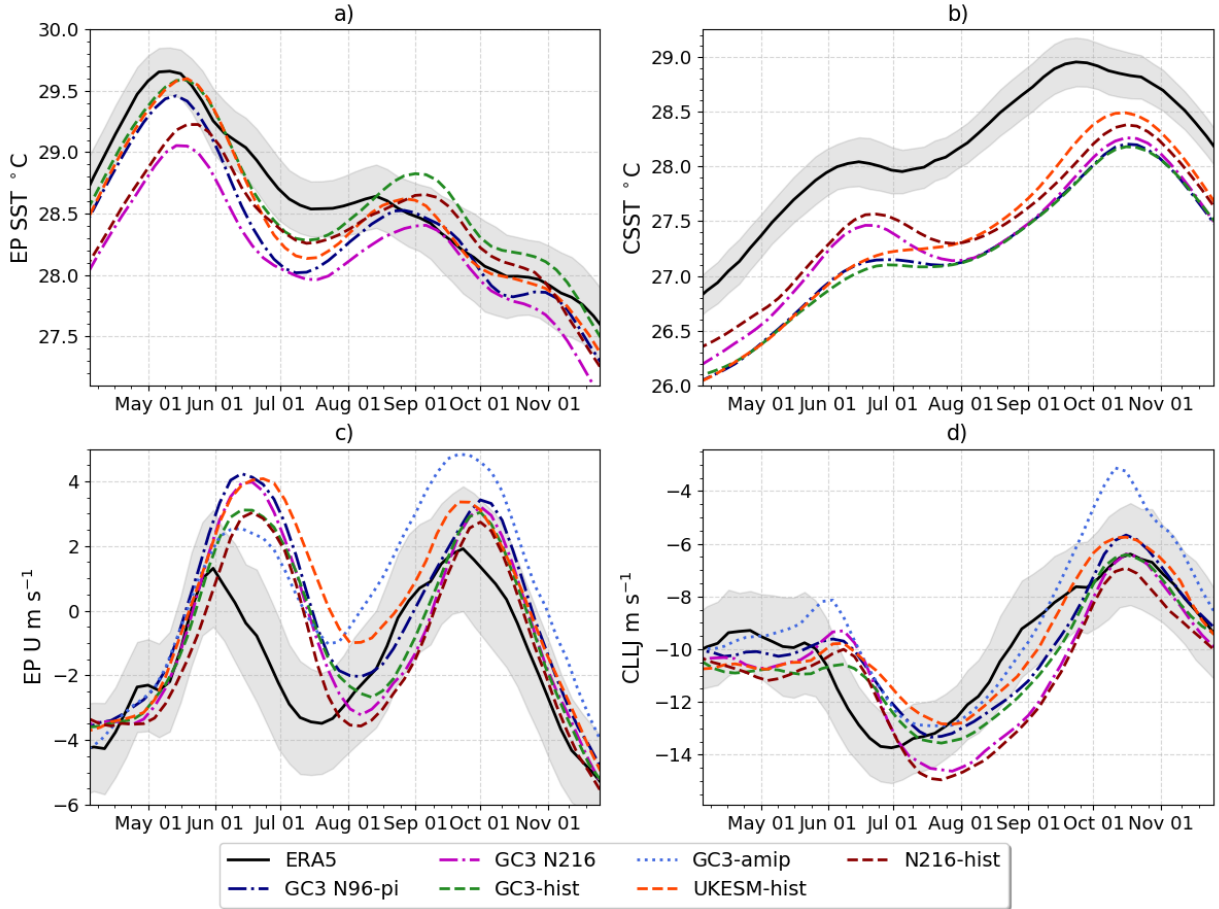


Figure 6.9: Pentad-mean seasonal march of the (a, b) SSTs [°C] and (c, d) the low-level (925-hPa) zonal wind flow [m s^{-1}] in (a, c) the easternmost equatorial Pacific and (b, d) the Caribbean Sea. The transparent shading is as in Figure 6.1. The regions used for EP and CSEA averages are illustrated in Figure 6.4h.

The literature suggests that a number of climatological features of the region play key roles for the MSD (Section 2.3). These climate features include the seasonal cycle of the East Pacific (EP) SSTs, the Caribbean Sea SSTs, the Eastern Pacific zonal wind flow and the CLLJ (Magaña et al., 1999; Amador, 2008; Herrera et al., 2015; Straffon et al., 2019; García-Martínez and Bollasina, 2020). The seasonal cycle of these features in ERA5 and the simulations (Figure 6.9) shows that the models are able to replicate the seasonal variations of the SSTs and the zonal wind flow of the region. However, some key biases are observed in the simulations.

The seasonal cycle of EP SSTs (Figure 6.9a) show the maximum peak SST in late May, prior to the first peak of precipitation in Mesoamerica. In contrast, the Caribbean

SSTs peak in early fall, about five months later, during late September. After the peak SST period in the EP, SSTs decrease to a local minimum found in July both for ERA5 and the simulations. The models show an overall cold bias in the SSTs in both regions, but this bias is most pronounced in the Caribbean Sea where throughout the wet season the SSTs in the models are colder than in ERA5.

The low-level wind flow in the EP shows a bimodal seasonal cycle in both ERA5 and the simulations (Figure 6.9c). The easterly flow in the EP during the spring becomes weaker turning westerly at the end of May and reaching a local maximum in early June in ERA5 and mid-June in the simulations. This local maximum then decreases during June and early July as the zonal wind becomes easterly again. The easterly flow peaks in mid July in ERA5 and about three weeks later in the simulations. The strength of this easterly flow magnitude during the midsummer varies greatly amongst the simulations. After the peak easterly flow in the midsummer, or zonal wind local minimum, the zonal wind becomes westerly again peaking at the end of September-early August in both ERA5 and simulations. This seasonality of the zonal wind in the EP is notably similar to the seasonal cycle of precipitation in the region, and the difference in the phase of ERA5 and the models is also the same between the zonal wind and precipitation.

The CLLJ seasonal cycle (Figure 6.9d) is reasonably replicated by the simulations, compared to ERA5, although the peak strength of the CLLJ, which is found during the last week of June in ERA5, is delayed in the simulations by about three weeks, as the simulated CLLJ peaks in mid-July in all the simulations. The simulations follow closely the late summer and fall seasonal cycle and magnitude of the CLLJ, except for a notable bias in GC3-amip in Oct-Nov characterised by a weaker than observed zonal wind.

6.4 The role of East Pacific SSTs

The East Pacific (EP) SSTs are a key element of the radiative-convective feedback mechanism of Magaña et al. (1999), which argues that the EP SSTs, cloud radiative effects and surface fluxes are part of a feedback mechanism that explains the two peak structure of the seasonal cycle of precipitation in Mesoamerica. A key prediction of this mechanism is that East

Pacific SSTs and surface fluxes exhibit a bimodal seasonal cycle in which EP SSTs and surface fluxes decrease during the first peak period and increase during the Midsummer drought period. In other words, this hypothesis predicts that the summer march of the EP SSTs should also exhibit a bimodal signal, similar to that observed for precipitation but out-of-phase, with the SSTs leading the precipitation. This section aims to evaluate these predictions for ERA5 and for the CMIP6 experiments.

According to the radiative convective feedback mechanism, the EP SSTs should cool

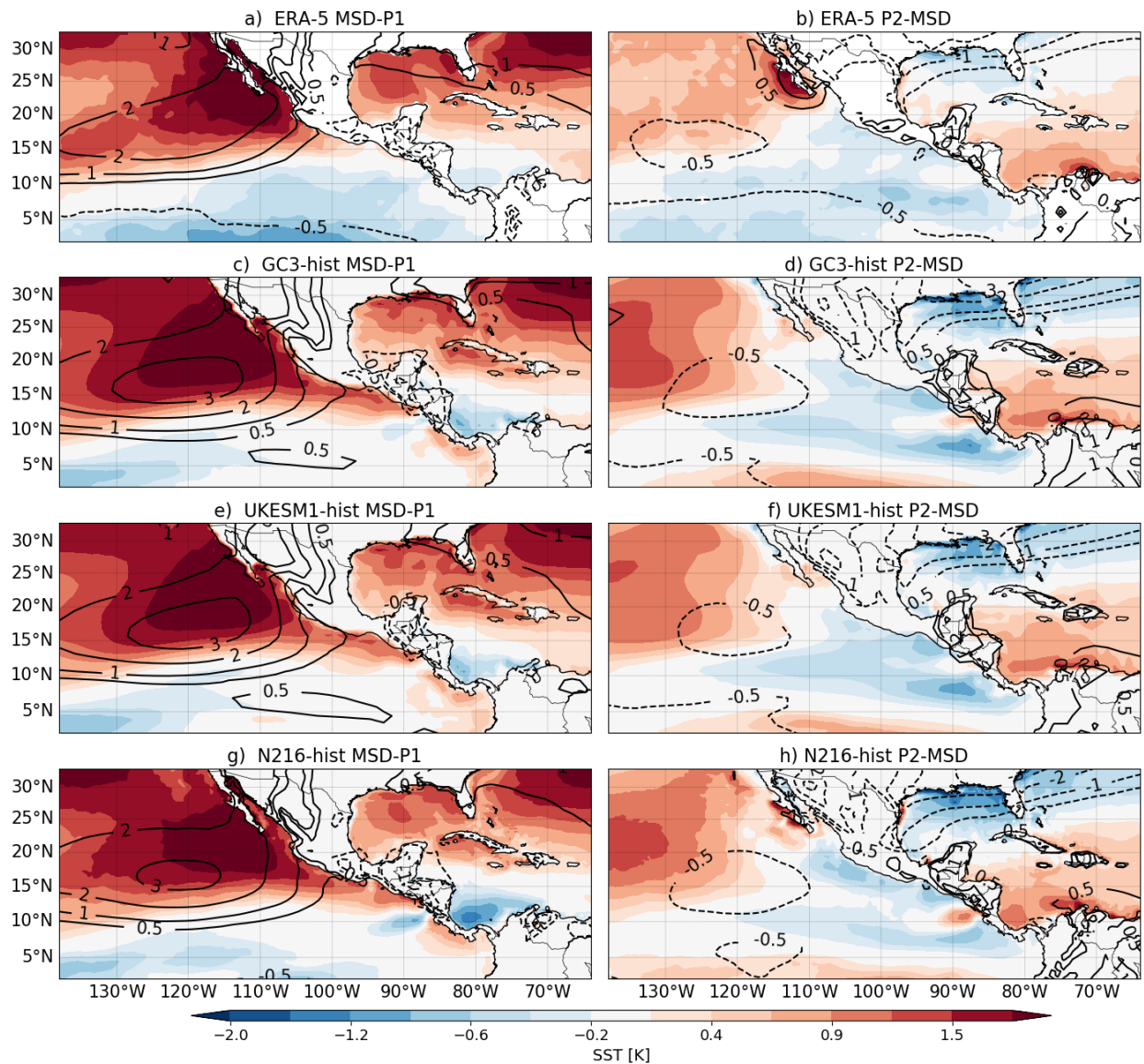


Figure 6.10: As in Figure 6.8 but the anomalies are shown for SSTs [K] (contours) and surface humidity [g kg^{-1}] (line-contours).

down during or slightly prior to the onset of the MSD and then increase during the local minimum of rainfall, i.e., during the MSD period which would lead enhanced precipitation and cause the second peak of precipitation in late summer. However, in ERA5 the EP SSTs only very slightly increase during the MSD (Jul-Aug) and instead of increasing in late summer rather cool again in late August and September. In fact, the EP SSTs in ERA5 decrease after mid-August, in synchrony with the second peak in deep convection and precipitation (Figs. 6.1 and 6.9a).

In the models, however, there is indeed a second peak in EP SSTs in late summer found in early September and therefore nearly synchronous to the second peak of precipitation. While EP SSTs clearly lead precipitation in May-June, the SST-precipitation relationship in mid and late summer is less obvious. In the models, the second peak of SSTs is nearly synchronous to the second peak in precipitation, which seems to contrast with the predictions of the radiative-convective feedback mechanism.

In order to better understand the relationship between EP SSTs and precipitation over the MSD region, the WT method is used to composite SSTs and surface humidity in the P1, MSD and P2 periods. The spatial distribution of SST and surface humidity changes associated with the MSD (Figure 6.10) suggest that the EP SSTs south of 10°N cool slightly between the first peak (P1) and the MSD periods, meanwhile the Gulf of California and the northern eastern Pacific significantly warms. At the end of the MSD (P2-MSD), the EP SSTs decrease in both ERA5 and the simulations. The P2-MSD panels also show that the Caribbean SSTs increase, associated with the peak Caribbean SSTs at the end of the summer (Fig. 6.9b).

The historical simulations generally agree with the composite differences of ERA5, with no appreciable warming in the EP region in the MSD-P1 panels, and cooling in the EP and the Gulf of Mexico and warming in the Caribbean Sea in the P2-MSD panels. These results suggest that while the seasonal cycle of EP SSTs show a bimodal signal, when each year of each simulation is examined using the WT method, which has proven to skilfully diagnose precipitation variations associated with the MSD, the EP SSTs do not synchronously warm during or after the MSD, as argued by the radiative-convective feedback.

An argument of the feedback mechanism is that the SST variability would force changes to the surface humidity and ultimately precipitation. The surface humidity in the EP

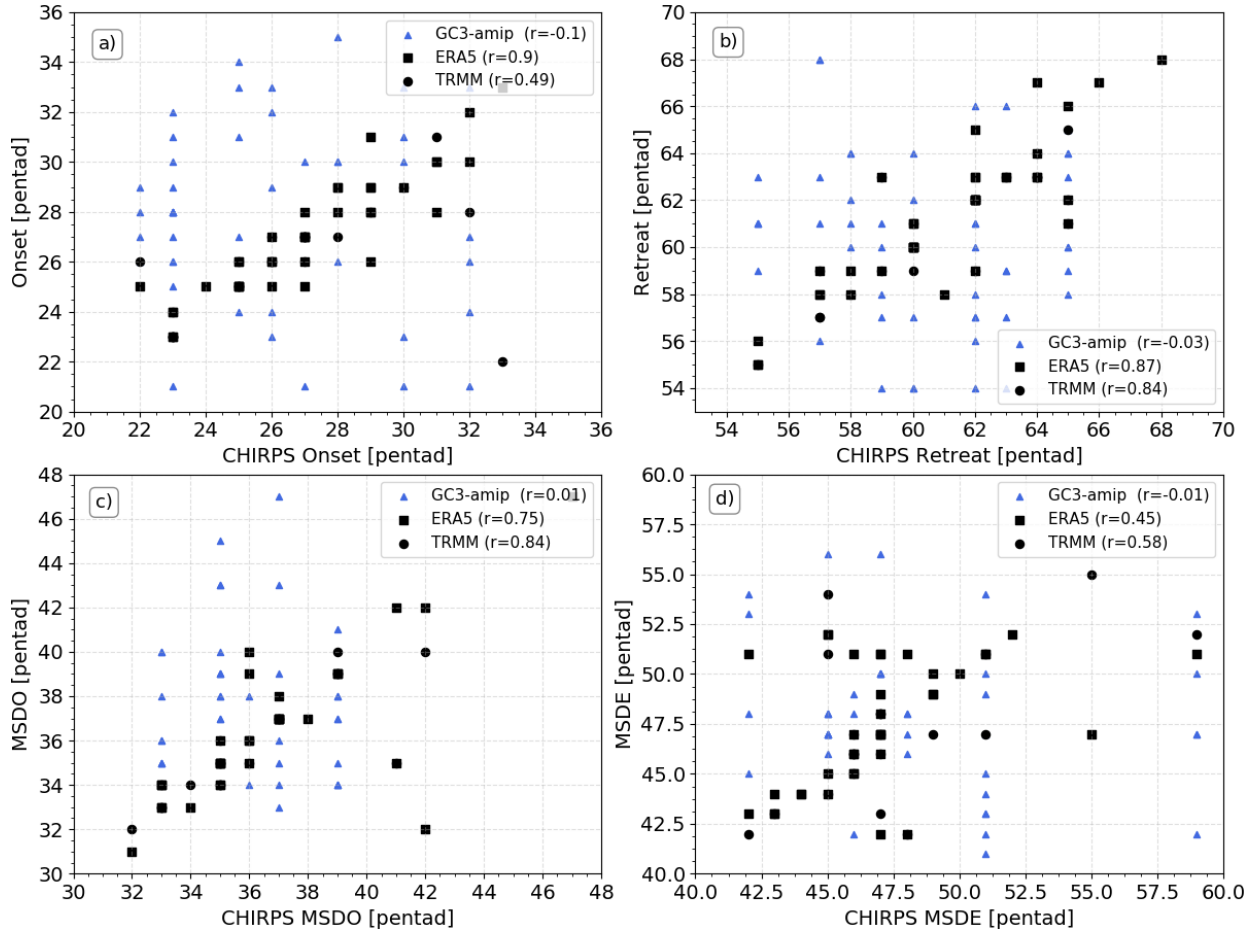


Figure 6.11: Scatterplots of the pentads diagnosed by the WT method as the dates of (a) monsoon onset (MO), (b) monsoon retreat (MR), (c) MSDO and (d) MSDE where the results of the CHIRPS dataset, on the x-axis, are compared with ERA5, TRMM and the GC3-amip simulation, on the y-axis. The legend shows the Pearson r coefficient for each comparison.

and MSD regions, however, is largely unchanged (less than 0.5 g kg^{-1}) during the various stages of the MSD (Figure 6.10), even though precipitation varies notably during these periods. Instead, the greatest variations in surface humidity are observed west of Baja California from the P1 to the MSD, and this region of increased surface humidity extends into the North American Monsoon region. Similarly, at the end of the MSD, the most notable variations in surface humidity is the drying of the North American monsoon region. The surface humidity variations in the simulations also agree well with those of ERA5 and are very similar amongst the realizations.

If the EP SSTs play a dominant role in the timings and strength of the MSD, as implied previously (Magaña et al., 1999; Magaña and Caetano, 2005; Herrera et al., 2015), then the

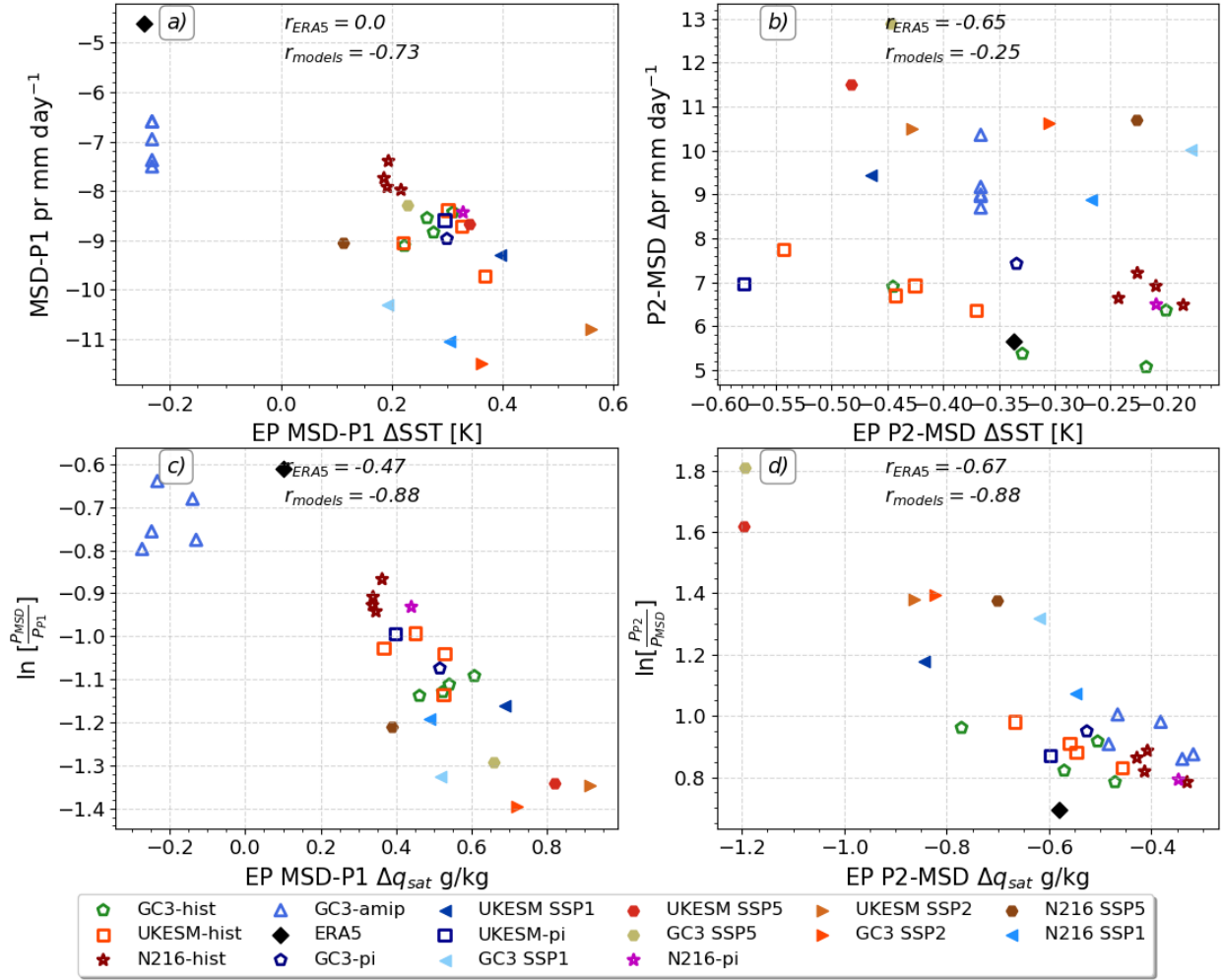


Figure 6.12: Scatterplots of the mean changes in the East Pacific (a, b) sea-surface temperatures (SSTs) and (c, d) surface saturation specific humidity q_{sat} in the x-axis with respect to precipitation variations in the MSD region on the y-axis for the (a, c) MSD-P1 and (b, d) P2-MSD periods. The correlation coefficient of the interannual spread in ERA5 and the multi-experiment correlation coefficient are shown in each panel.

simulations with imposed SSTs taken from observations, e.g., the GC3-amip experiment, may be further explored to evaluate the links between the timings or strength of the MSD in GC3-amip and ERA5. A scatter plot of the dates (pentads) of the MO, MR, MSDO and MSDE (Figure 6.11) for matching years between the CHIRPS dataset and TRMM, ERA5 and the five ensemble members of GC3-amip shows that the timings of the MSD in GC3-amip are unrelated to CHIRPS and ERA5. In fact ERA5, in spite of precipitation being largely a model-derived quantity in the reanalysis, produces MSD timings that agree fairly well with the CHIRPS and TRMM datasets. This evidence would suggest that the

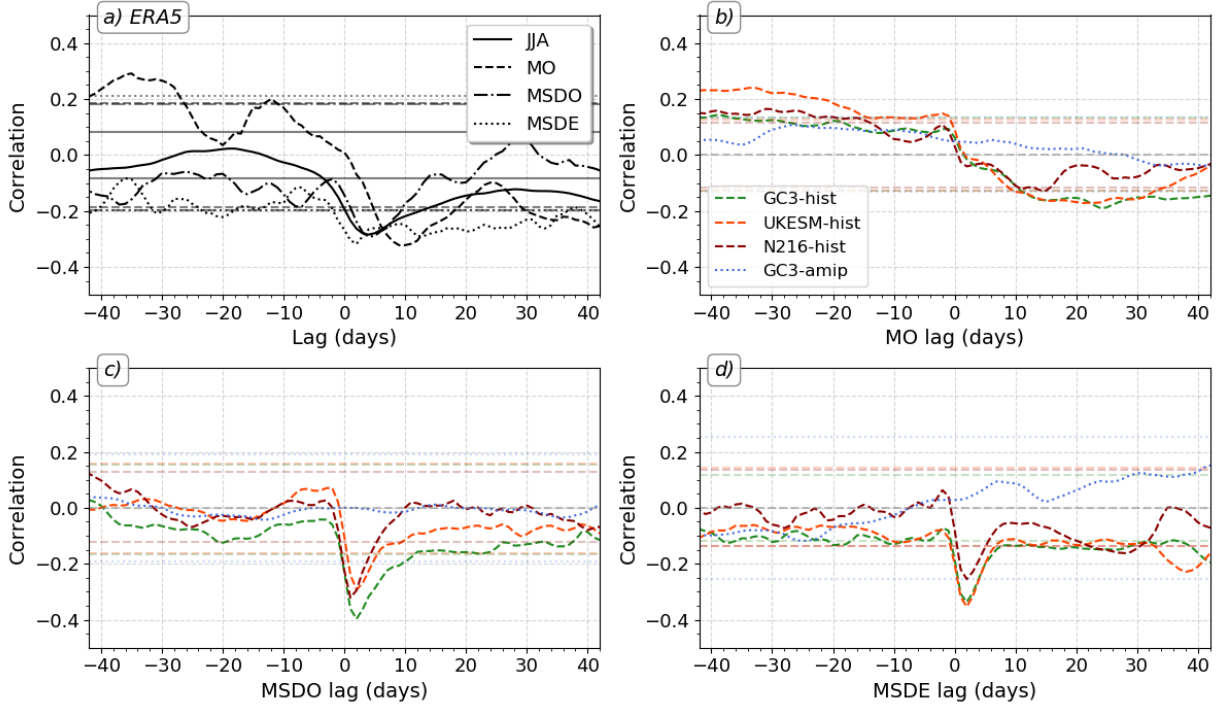


Figure 6.13: Lagged correlations between East Pacific SSTs and precipitation in the MSD region for (a) ERA-5 where the lag 0 date was used in four different ways: first, all the boreal summer JJAS SSTs and precipitation pairings, then lag 0 represents the monsoon onset (MO), MSD onset (MSDO) and MSDE dates. (b-d) as in (a) but for the simulations where the correlations are computed with the SST-precipitation timeseries lagged with respect to the b) monsoon onset date, the c) MSDO date and the d) MSDE date.

SSTs forcing the model in GC3-amip are not the dominant factor controlling the timings of the MSD in these atmosphere-only runs.

Alternatively, the interannual variability in ERA5 and the differences amongst the MOHC CMIP6 experiments may be further explored to understand whether the changes to the SSTs are related to changes in the precipitation. For this purpose, composite differences between the P1, MSD and P2 periods were computed for each variable for each year in each dataset and then averaged to provide a mean value that relates changes in precipitation to different diagnostics in different stages of the rainy season. For example, the mean difference in SSTs (Figure 6.12a) between the P1 and the MSD periods, show a cooling difference for ERA5 associated with a smaller precipitation reduction. In contrast, the coupled model simulations show a positive SST difference (warming) associated with a greater precipitation reduction during MSD compared to the P1 period.

The slight warming signal in the MSD-P1 difference (Figure 6.12a) in the coupled-model experiments agrees with the seasonal cycle (Fig. 6.9) and suggests that in the model, as precipitation decreases during the MSD, the EP SSTs warm even though this warming is fairly modest. At the MSDE stage, the EP SSTs cool (Figure 6.12b) associated with a positive increase in precipitation, suggesting an inverse relationship between EP SSTs and precipitation. However, the relationship does not seem to explain the inter-experiment spread or the inter-annual variability in ERA5 as the correlation coefficients are low and not significant, i.e., a stronger second peak is not associated with a cooler EP SSTs in late summer.

The feedback mechanism of Magaña et al. (1999) suggests that one of the main consequences of the SST changes would be changes to evaporation and surface humidity. Furthermore, evidence of tropical precipitation also suggests that the surface saturation specific humidity q_{sat} , which measures the maximum moisture that a parcel can hold, provides a strong link between precipitation and SSTs on seasonal time-scales over tropical oceans (Yang et al., 2019; Good et al., 2021). For these reasons, Figure 6.12 also shows the relationship between the saturation specific humidity and precipitation.

The temporal changes to q_{sat} associated with the MSD timings (Figure 6.12c,d) are not positively related to changes in the precipitation over the MSD region. Although the inter-annual variability of q_{sat} changes during the MSD-P1 period in ERA5 shows a positive correlation, the mean changes to q_{sat} during this stage are very small compared to the differences in the experiments and, furthermore, the relationship for the simulations shows an opposite relationship (negative correlation). For the P2-MSD differences, there is a negative correlation for both ERA5 and the experiments, an expected result since SSTs cool in this same period. A more direct local relationship between q_{sat} and pr was also investigated for the EP and the MSD regions individually (not shown). This analysis showed a weaker (but still negative) relationship in both regions between q_{sat} which suggests that changes to q_{sat} are not strong enough to explain the variability of precipitation.

The previous results have analysed synchronous changes between the EP SSTs, surface humidity, q_{sat} and precipitation over the MSD region, but the expected relationship may exist with some lags, in particular as suggested by the radiative-convective feedback mechanism the SSTs should be leading precipitation. Lag-lead correlations (Fig. 6.13) of the EP

SSTs and the precipitation in the MSD region show that only during monsoon onset are these two fields significantly positively correlated at lags of \approx -35 days in ERA5 and -40 to -20 days in the historical experiments.

In ERA5, the correlation for all the boreal summer (JJAS) sample is only significant for the SSTs leading precipitation region for negative lags from 30 to 40 days and is only significant (negative correlation) at positive lags at lag +5 days, indicative of an inverse SST-precipitation relationship where the SSTs follow precipitation. In the models (Fig. 6.13b-d), very similar results are found where significant positive correlations at negative lags, indicative of SSTs leading precipitation, are only found for the MO panel, whereas for MSDO and MSDE panels, the correlations are only significant at positive lags and for negative correlations, indicative of the precipitation leading the SSTs on the scale of 3-5 days and SSTs decreasing with increased precipitation.

This section investigated the radiative-convective feedback hypothesis by Magaña et al. (1999) by inspecting whether the seasonal cycle of SSTs in the East Pacific match the predictions of the theory. Results in this section show that in observations, the EP SSTs do not exhibit a double-peak seasonal cycle, so the second peak of precipitation over the MSD region cannot be driven by a second, late summer, peak in EP SSTs. Furthermore, there was no evidence found that the decrease of precipitation during the midsummer to be statistically related to the decrease of EP SSTs in observations/reanalysis or in the CMIP6 simulations.

6.5 On the role of cloud-radiative effects

The mechanisms proposed by Magaña et al. (1999) and Karnauskas et al. (2013) both suggest that the net shortwave energy absorbed by the surface is key in the driving mechanism of the MSD. Magaña et al. (1999) suggests that tall convective clouds influence the timings and net shortwave (SW) flux at the surface, and although not explicitly mentioned as such, Magaña et al. (1999) argues that the cloud-radiative effects (CRE) experience seasonal changes that occur at the same as the MSD. In turn, Karnauskas et al. (2013) argues that the seasonal march of solar insolation determined by the solar declination angle controls the net shortwave absorbed by the surface. These studies motivate a further

inspection of CRE in the simulations to understand whether there is evidence to support these previously proposed hypotheses.

CRE effects are coupled to the tropical circulation (Bony et al., 2004; Webb et al., 2017) and have been shown to be related to the timing and strength of regional (Guo et al., 2015) and axi-symmetric (Byrne and Zanna, 2020) monsoons. The long-wave (LW) CRE plays an important role in the convective heating and moistening of the atmospheric column in tropical regions and the short-wave (SW) CRE affects the surface absorption of energy (Allan, 2011). These studies motivate a deeper investigation of the CRE in the Mesoamerican region, specifically for the timings and strength of the MSD. The surface cloud radiative effect (CRE_{surf}) is computed from daily-mean fields following Allan (2011), as the sum of the LW and SW CREs, i.e.:

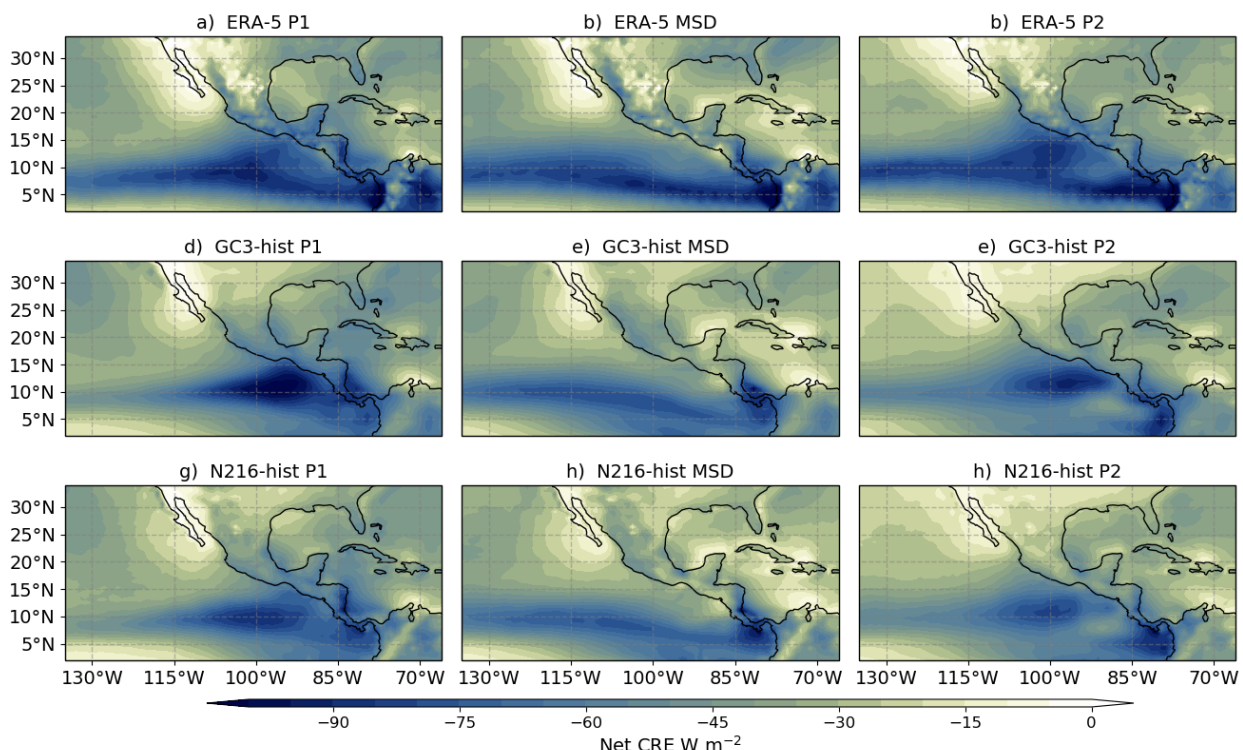


Figure 6.14: Composite mean cloud radiative effect (CRE) [W m^{-2}] during the periods of onset of the MSD, the MSD and the end of the MSD for (a-c) ERA5, and the ensemble mean of (d-f) GC3-hist and (g-h) N216-hist.

$$\begin{aligned} CRE_{surf} &= LWCRE_{surf} + SWCRE_{surf} \\ &= LDS - LUS - (LDS_{cs} - LUS_{cs}) + SDS - SUS - (SDS_{cs} - SUS_{cs}), \end{aligned} \quad (6.1)$$

where the fluxes are depicted as long-wave (L) or short-wave (S) and downwelling (D) or upwelling (U) at the surface (S) and the subscript $_{cs}$ denotes under clear-sky conditions. The long-wave upwelling at the surface (LUS) virtually cancels with the LUS_{cs} because the long-wave emission from the surface is minimally dependent on the presence of clouds (Allan, 2011). The net CRE at the surface is then given by:

$$CRE_{surf} = LDS - LDS_{cs} + SDS - SUS - SDS_{cs} + SUS_{cs}. \quad (6.2)$$

The net CRE during P1, MSD and P2 periods (Fig. 6.14) is negative and the minimum values are found in the East Pacific ITCZ region. The differences between the MSD timings closely follow the precipitation changes during these periods as the minimum CRE in the EP and the Mesoamerican region is found during the two peaks of precipitation with a weaker CRE over the Mesoamerican region and nearby basins during the MSD. The smallest CRE is found over the Baja California Peninsula. The results of the two historical experiments closely follow the results of ERA5, and the only notable difference between the lower (GC3) and the higher (N216) resolution historical experiments is that the CRE is stronger in GC3-hist than in N216-hist.

The individual contributions of the SW and LW surface CREs (Figures 6.15 and 6.16) show that the dominant term in the EP and Mesoamerican regions is the SW term. The negative SW CRE is strongest in the EP ITCZ region and the SW CRE varies with the MSD timings in similar fashion to the net CRE, i.e., in the MSD region, the SW term is notably larger ($< -90 \text{ W m}^{-2}$) during the two peak periods of precipitation than during the MSD. The historical experiments also show that the SW CRE is larger in magnitude in the EP ITCZ region and that the SW CRE over the MSD region varies notably in the three stages of the rainy season.

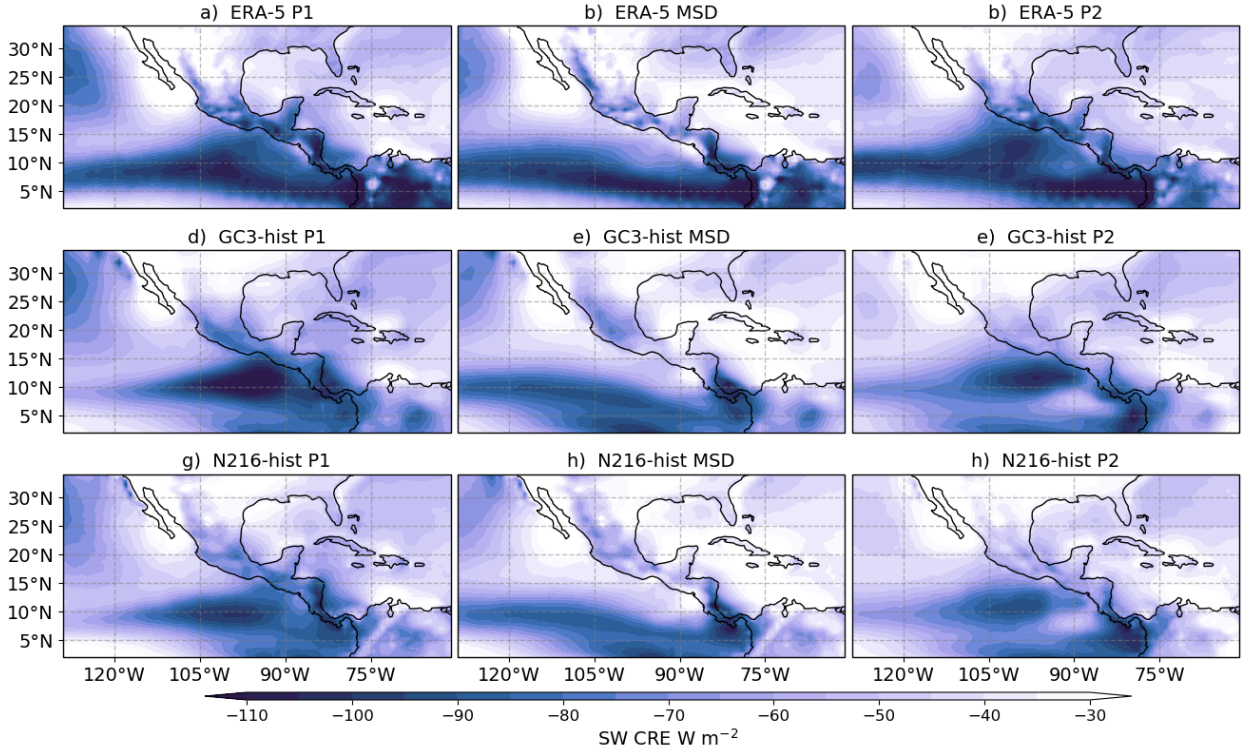


Figure 6.15: As in Fig. 6.14 but for the short-wave radiative effect.

In contrast, the LW term (Figure 6.16), is generally smaller in magnitude than the SW term and is largest over land and in the ocean west of the California. Over the EP and CSEA regions, the LW term shows very small horizontal gradients, indicative of a fairly horizontally homogenous effect of clouds. The differences of the LW between the stages of the MSD are smaller than the SW term variations, but both in ERA5 and the simulations, the LW term over the EP and the Caribbean Sea is visibly larger during the two peak periods than during the MSD.

These composites depict how the spatial distribution of the CRE varies with the MSD timings over the larger Intra-Americas Seas region, but how these terms actually within the season in the MSD region is not obvious. The seasonal cycles of the SW, LW and net CREs (Figure 6.17a-c) show bimodal signals characterized by stronger CREs during the two peak periods during June and September and a relative minimum in between found in late July in ERA5 and early August in the simulations. The simulations reasonably simulate the magnitude of the net and SW CRE during the early summer season but overestimate

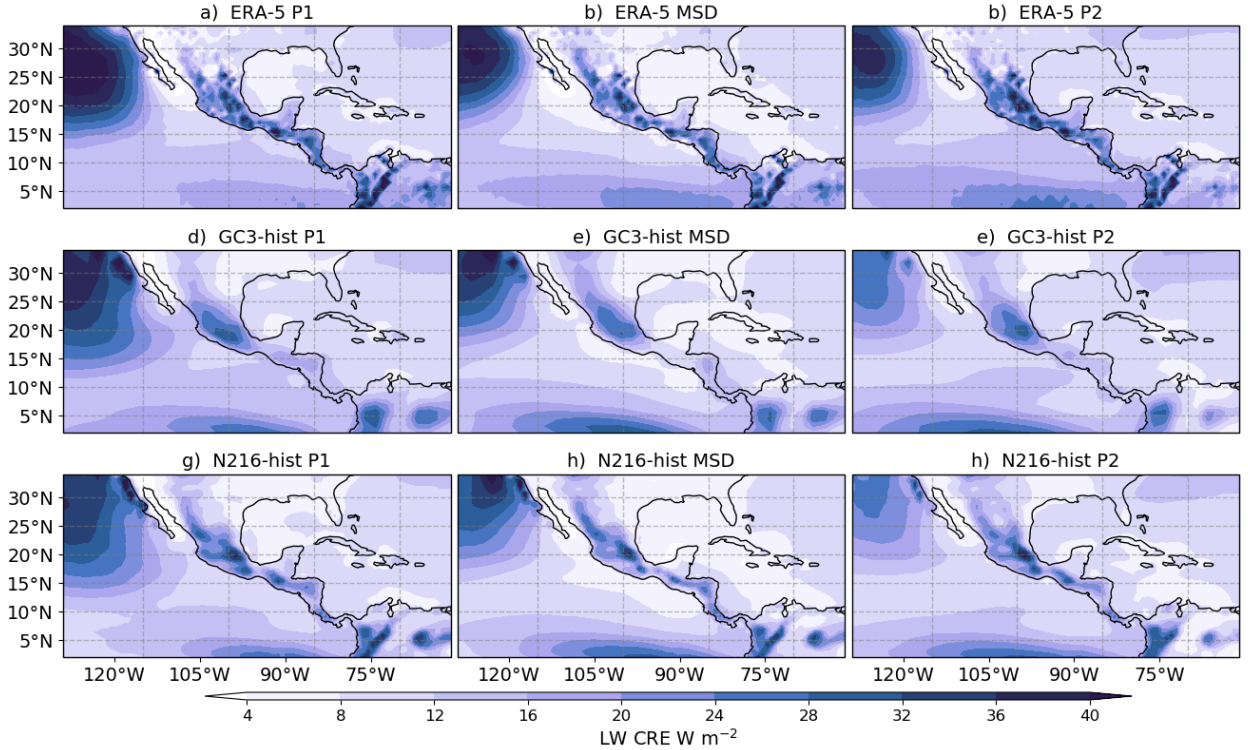


Figure 6.16: As in Fig. 6.14 but for the long-wave CRE.

the decrease in the net, SW and LW CRE during the midsummer, very likely associated with the underestimation of precipitation over this same period (Figure 6.1).

Regardless of CREs, according to Magaña et al. (1999) and Karnauskas et al. (2013), the net SW (the difference between upwelling and downwelling shortwave) at the surface should also present a bimodal seasonal cycle. In both ERA5 and the simulations, the net SW (Figure 6.17d) follows a two-peak seasonal cycle characterized by a first peak in late May, which coincides with the peak in East Pacific SSTs. This peak in SW is followed by a local minimum during June which is followed by a secondary increase in July in ERA5 and extending to August in the simulations. After this second local maximum, there is another sharp decrease in the net SW at the surface at the end of the summer, which coincides with the the second peak in precipitation and therefore possibly linked with less downwelling SW.

The spatial distribution of changes to the net SW at the surface (Figure 6.18) show that from the first peak to the MSD there is a positive difference net SW, indicative of more SW energy absorption at the surface of about 30 W m^{-2} in ERA5 and 40 W m^{-2} in the simulations. In contrast, for the P2-MSD differences, a notable reduction in net SW energy is

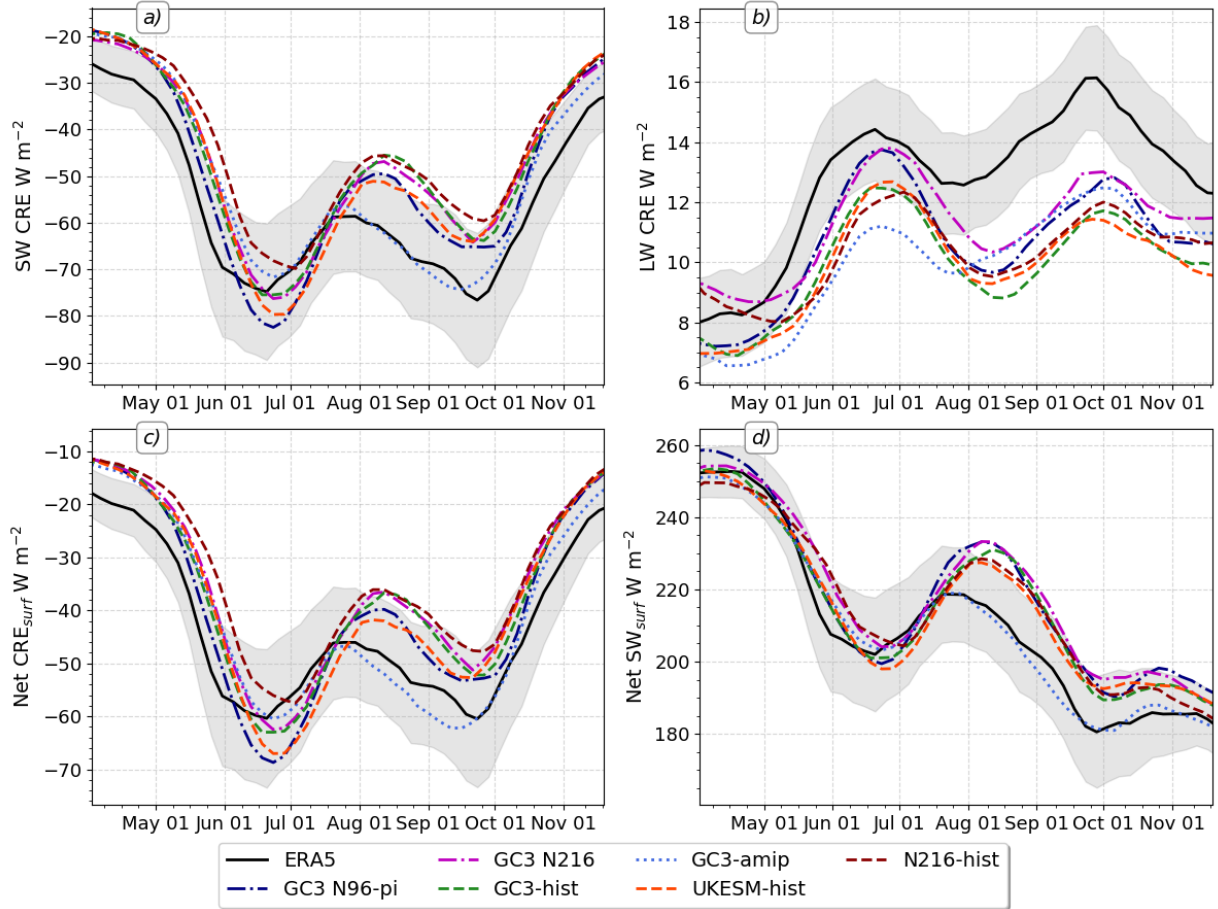


Figure 6.17: Pentad-mean seasonal cycle of the (a) SW and (b) LW CREs, (c) the net CRE, and (d) the net SW at the surface, signed positive to indicate surface absorption of SW radiation.

observed throughout the North American continent but the maximum reduction is found on the western coast of southern Mexico. One might reasonably then suspect that the increased SW absorption during the MSD may indeed be a cause or part of the mechanism for the second peak of precipitation, as suggested by both Magaña et al. (1999) and Karnauskas et al. (2013). However, this could just be a correlation that highlights the coupling between clouds, radiation and precipitation and not necessarily that SW heating is the driving mechanism.

These hypotheses are further tested through scatter and lag-lead regression analysis (Figure 6.19). The changes to the net SW at the surface are unrelated to the interannual variability of the changes to precipitation in ERA5. The reduction in SW in the MSD-P1 periods shows a 0.0 correlation with the changes of precipitation during the same stages, whereas the net SW absorbed in the EP during the MSD period is negatively correlated

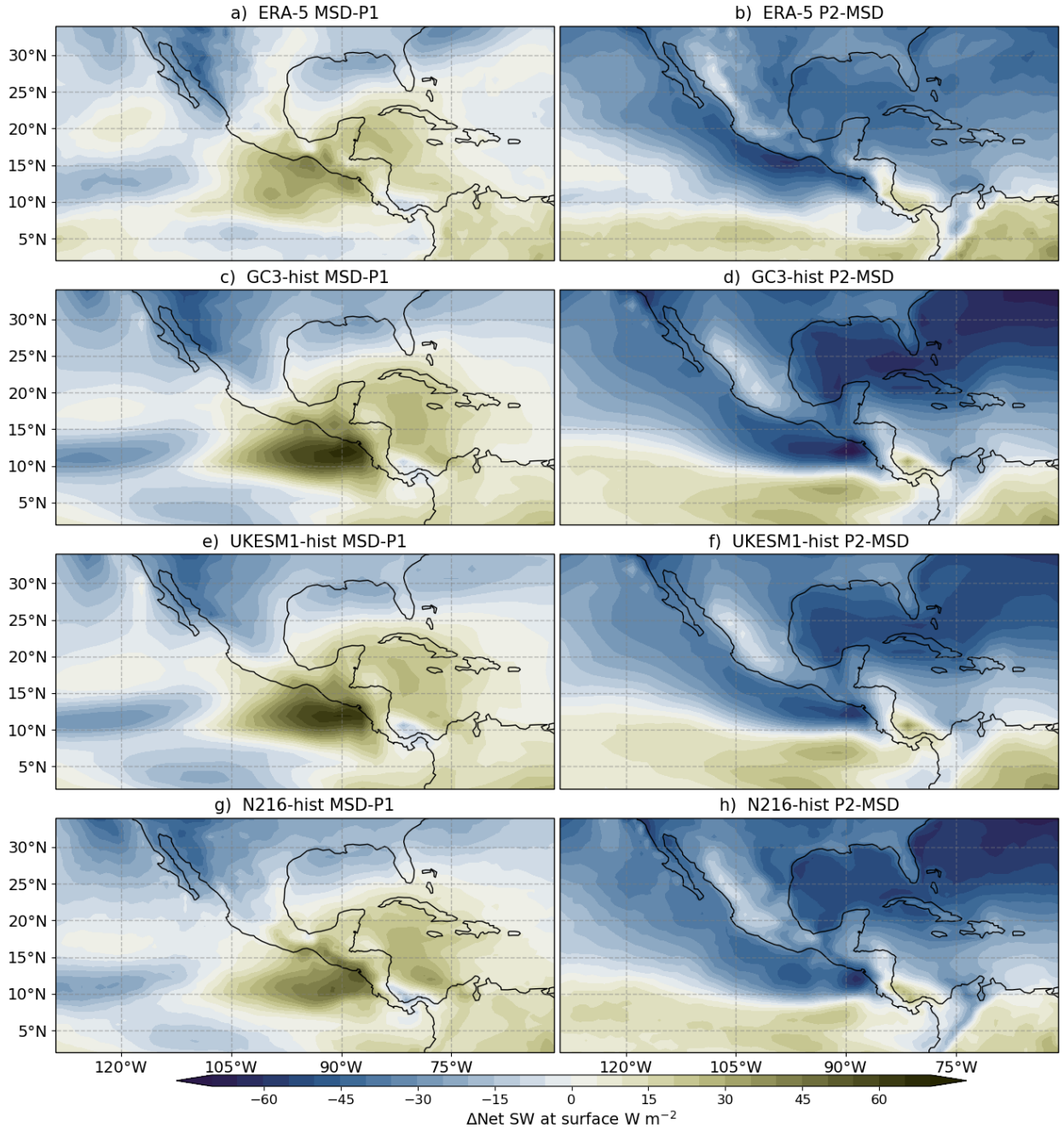


Figure 6.18: As in Fig. 6.8, but for the net shortwave radiation [W m^{-2}] at the surface.

with precipitation during the second peak. In other words, years where less shortwave is absorbed in the EP is associated with years stronger second peaks in the MSD region, in marked contrast to previous hypotheses.

Furthermore, in the MOHC CMIP6 experiments there appears to be only a modest relationship between net SW and precipitation. The changes to SW during the MSD-P1 are

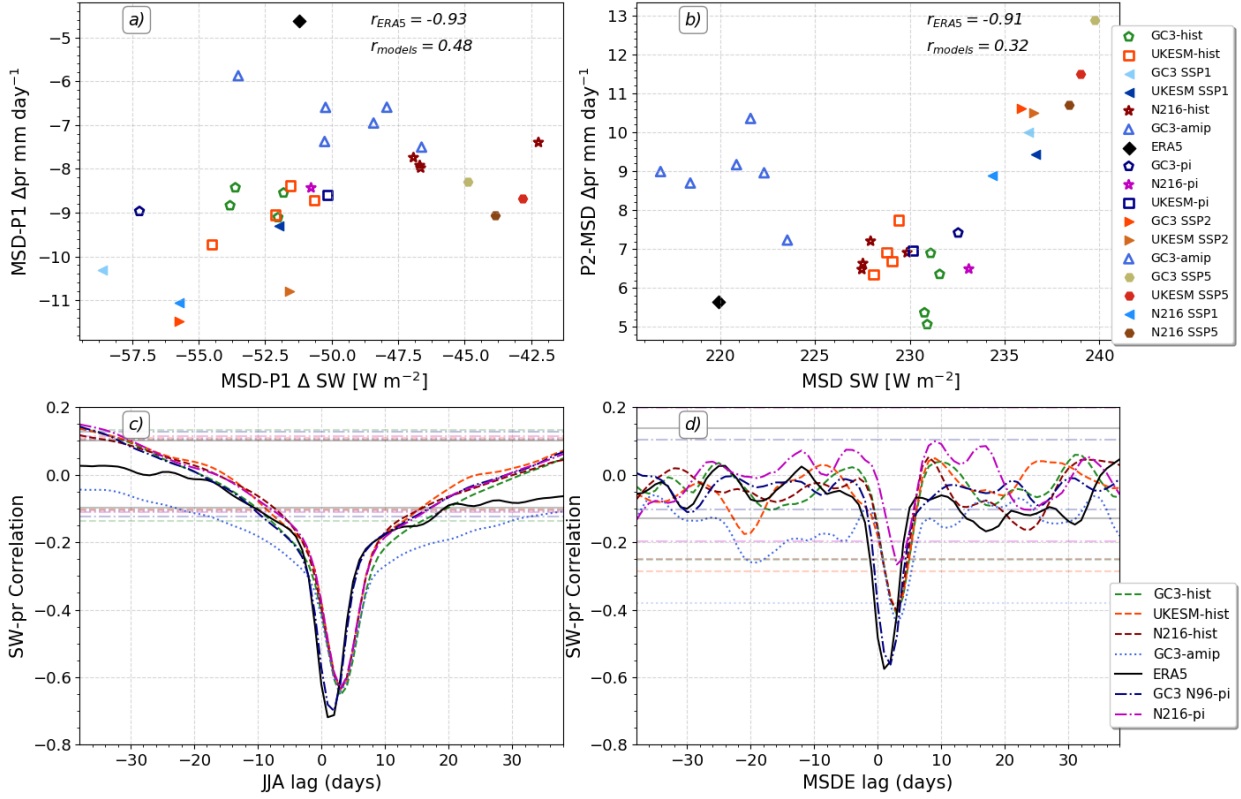


Figure 6.19: (a, b) Scatter of the mean changes to the net short-wave (SW) at the surface (abscissa) with respect to changes in precipitation for different MSD stages. (c, d) Lagged-regression coefficients between the net shortwave absorption in the East Pacific and precipitation over the MSD region for the (c) the JJA season and (d) around the MSDE date.

only modestly related to precipitation as simulations that have the smallest changes to net SW in this period do not exhibit the smallest changes to precipitation. Similarly, a very weak relationship between SW and precipitation is found within the different experiments to relate the net SW at the surface during the MSD and the strength of the second peak.

Lag-lead relationships (Figure 6.19c, d) confirm that there is a strong correlation between SW and precipitation but this is a negative correlation at lag 0. This negative correlation illustrates that strong precipitation periods are associated with less shortwave absorbed by the surface, due to the high clouds blocking incoming SW. Correlations are not significant outside of lag -5 to 5 days near the MSDE date, although they appear significant for some coupled simulations at lags of -40 days when the entire JJA season is considered. These results appear contradictory with the argument of Karnauskas et al. (2013) who argued a lagged relationship between shortwave absorption at the surface and precipitation at the end of the MSD.

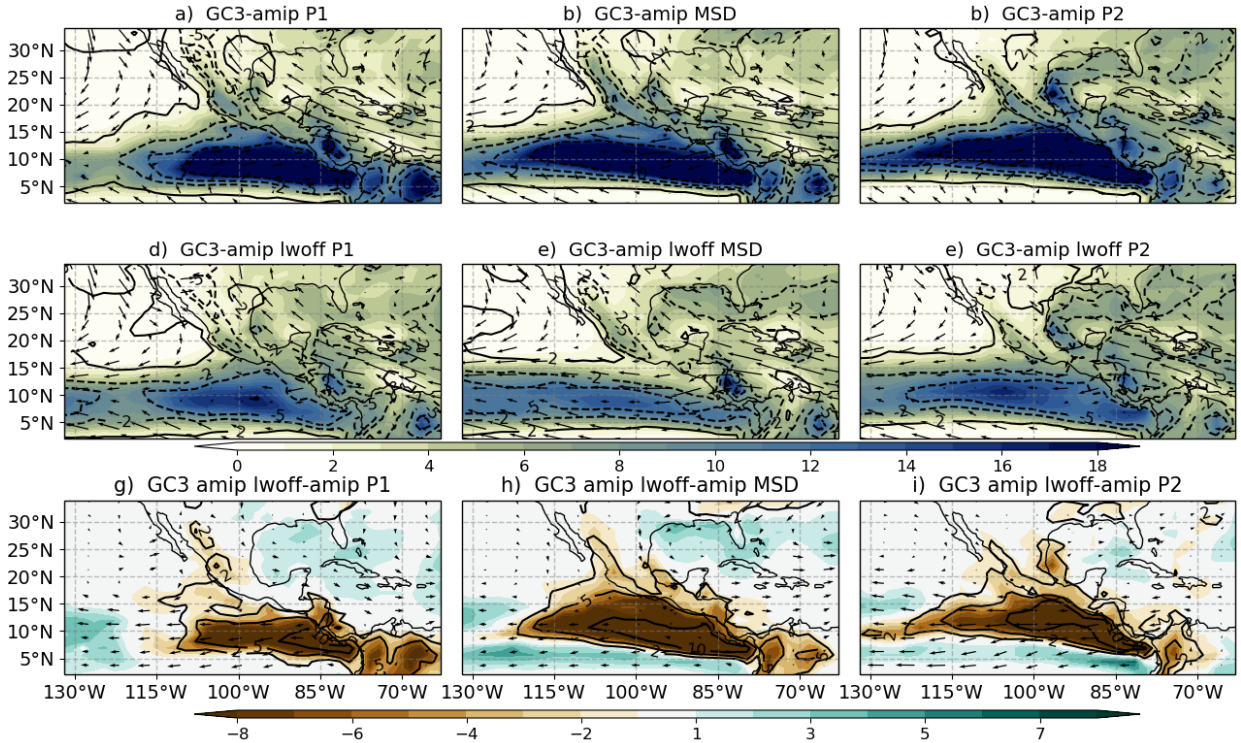


Figure 6.20: Composite mean precipitation (shading in mm day^{-1}), vertical velocity (contours in $10^{-2} \text{ Pa s}^{-1}$) and 850 hPa wind speed (vectors) for the P1, MSD and P2 periods in the (a-c) GC3-amip and (d-f) GC3-amip lwoff experiment. (g-i) shows the difference between the lwoff-amip and the amip experiments.

Finally, while the incoming SW radiation plays an important role in several theories for the MSD, the LW effects have important consequences in general monsoon dynamics (Guo et al., 2015; Byrne and Zanna, 2020). The GC3-amip lwoff experiment is part of the contributions from the Cloud Feedback MIP (CFMIP) (Webb et al., 2017) to CMIP6. This experiment is identical to the GC3-amip experiment except that the treatment of the LW in the radiation code in the model is not affected by the presence of clouds, in other words all LW fluxes are assumed to be under clear-sky conditions.

The impact of the LW CRE for precipitation in the Mesamerican region is critical (Figure 6.20). When the LW effects of clouds are ignored, precipitation over the whole domain is greatly reduced (50-80%), ascent becomes weaker and the low-level circulation also weakens. These results are in agreement with previous studies (Guo et al., 2015; Byrne and Zanna, 2020) that show that cloud radiative heating strengthens the local and regional circulation in a monsoon. The circulation and precipitation is so diminished in

GC3 amip-lwoff that this is the driest simulation found in this chapter (Figure 6.7). The monsoon precipitation is so diminished that small variations between the MSD and the two peak periods of precipitation are almost undistinguishable.

This section diagnoses the seasonal cycle and spatial variability of CRE at the surface as depicted by ERA5 and the CMIP6 simulations. The net CRE at the surface is dominated by the SW term, indicating the strong effect that convective clouds have to block SW radiation from reaching the surface throughout the summer. The total absorbed SW shows a double-peak structure, with the second peak appearing at the end of the MSD period for both ERA5 and CMIP6 simulations, as suggested in the solar declination angle hypothesis Karnauskas et al. (2013). However, the strength and timing of the changes to the SW absorption suggest that the relationship between SW heating and precipitation is more of a correlation than a causal link from the SW to the precipitation.

6.6 The role of the Caribbean Low-Level Jet

The previous sections evaluate the radiative-convective feedback and the solar declination angle hypotheses, in addition, this section examines the role of the Caribbean Low-Level Jet (CLLJ) for the MSD of Mesoamerica. Section 6.3 shows that the seasonal cycle of the low-level zonal wind, i.e., the CLLJ, is well represented by the simulations (see Figure 6.9d), but the timing of the peak magnitude of the CLLJ in the models is delayed by about three weeks with respect to ERA5. The timing of the start of the MSD is notably also delayed in the models by around 10 days, according to Table 5.3 in the previous chapter. This evidence is suggestive that the CLLJ may be playing a role in the timings of the MSD in the simulations, which would be consistent with previous studies (e.g. Herrera et al., 2015; Martinez et al., 2019).

The main dynamical argument that links the MSD in southern Mexico and Central America and the CLLJ is centred around variations in the moisture flux convergence (MFC), and subsequently in the total water content (TWC) (see e.g. Gamble et al., 2008; Herrera et al., 2015; Martinez et al., 2019; Zermeño-Díaz, 2019). For this reason, this section examines the CLLJ magnitude as measured by the 850 hPa zonal wind in the Caribbean Sea (see box in Figure 6.4), and the integrated moisture flux convergence (IMFC) and

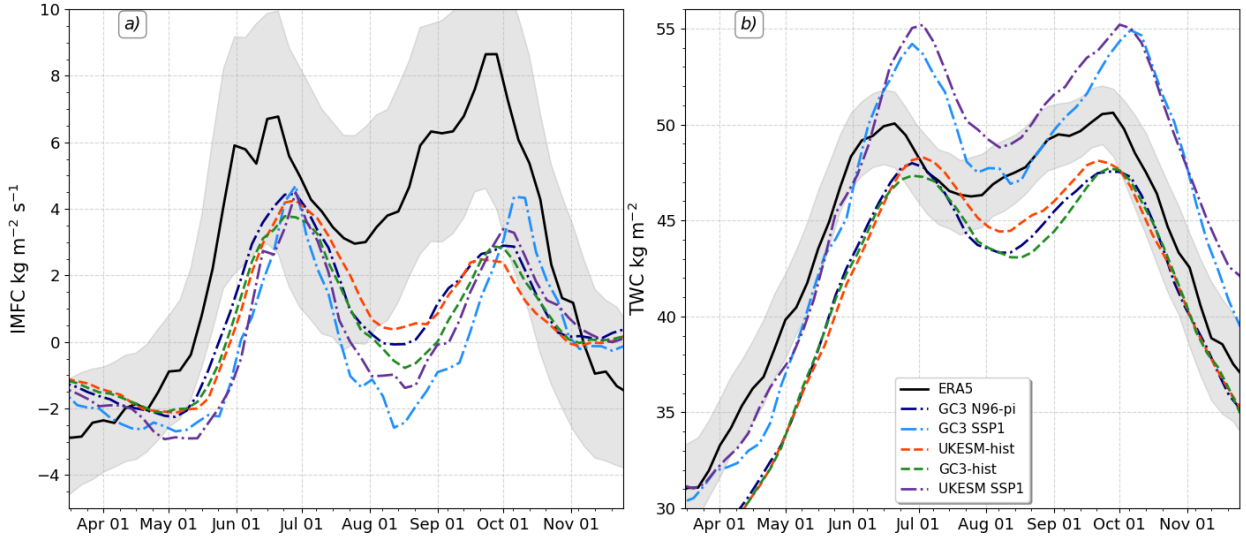


Figure 6.21: Seasonal cycle of (a) IMFC and (b) TWC averaged over the MSD region.

TWC in the MSD region. The IMFC was calculated using the following equation from daily ERA5 data and daily data from the simulations:

$$IMFC = -\left\langle \nabla \cdot \vec{u}q \right\rangle \quad (6.3)$$

where q is the specific humidity at each pressure level, \vec{u} is the wind vector and ∇ is the horizontal divergence operator and the $\langle \rangle$ operator denotes column integrals in the troposphere.

The seasonal cycle of the IMFC and TWC (Figure 6.21) averaged over the region of the MSD shows a strong bimodal signal, with two maxima in IMFC and TWC occurring roughly at the same time as the two peaks in precipitation and a minimum found during Midsummer. The simulations follow closely the variations of the seasonal cycle of ERA5, but with a weaker IMFC over the region in all the simulations, particularly after the period of the first peak of precipitation.

The magnitude of the two peaks of IMFC is fairly similar for all the simulations, in contrast with the asymmetry between the first and second peaks of precipitation, e.g., the historical experiments show a wetter first peak than the second peak. The IMFC during MSD, in contrast, shows notable differences amongst experiments, with the SSP1 experiments showing a smaller IMFC compared to the historical and piControl experiments, in fact in early August the IMFC is negative (indicative of moisture divergence) in the SSP1 experiments.

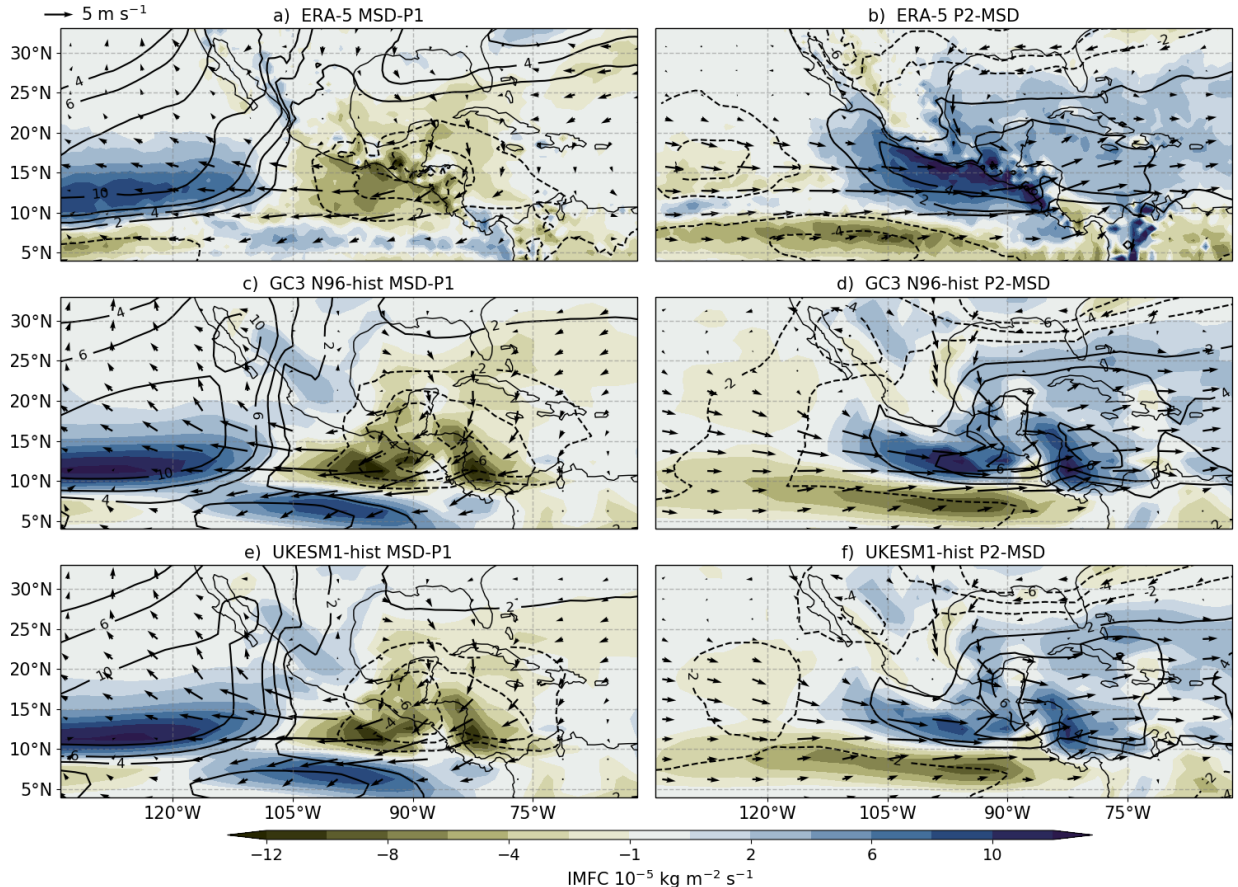


Figure 6.22: As in Figure 6.10, but showing variations in the IMFC (shading), TWC (contours in units of kg m^{-2}) and 850-hPa wind (vectors).

The magnitude and timings of the two peaks in TWC is fairly similar amongst the piControl and historical experiments and fairly similar to ERA5, however, notable differences exist. Firstly, the drying of the column in the simulations during midsummer occurs weeks after the drying in ERA5, which agrees with the differences in the seasonal cycle of precipitation. Secondly, the low-emission scenario (SSP1) runs show a higher TWC indicative of a moistening of the column throughout all the seasons for a relatively low greenhouse forcing. However, the SSP1 experiments show the strongest decrease in TWC from the P1 to the MSD period of all the simulations, likely associated with the negative IMFC found during this period. Similarly, the SSP1 experiments show the strongest moistening of the column in late summer of all the simulations.

The IMFC, TWC and 850-hPa wind variations associated with the MSD (MSD-P1 and

P2-MSD) are shown in Figure 6.22 for ERA5 and two simulations. The patterns observed in the low-level wind vectors associated with the MSD timings follow closely the previously reported "MSD patterns" described by Zermeño-Díaz (2019), which confirms that the WT method is able to extract similar patterns in the low-level wind associated with the MSD to other techniques. The wind flow pattern in the MSD-P1 panel is characterised, both in ERA5 and the simulations, by modest northeasterly anomalies in the Gulf of Mexico and the CSEA and strong easterly anomalies over the EP region. These wind anomalies indicate that as the wetter first peak period transitions to the drier MSD, the wind field changes from a weak low-level westerly wind to an easterly wind (see also Figure 6.9c). At the end of the MSD, the wind direction changes again to a westerly direction in the East Pacific, whereas the wind anomalies in the Caribbean Sea turn to westerlies indicative of a weakening of the CLLJ, coincident with the second peak of precipitation observed in the MSD region.

IMFC and TWC show coherent variations with the timings of the seasonal cycle of precipitation in the MSD region, with less moisture convergence and precipitable water in the column during the drier period compared to the two peak periods. In contrast, west of the coast, at around the 125°W, during the MSD there is increased TWC and IMFC in ERA5 and in the simulations, in agreement with the previous sections which showed increased convective activity in this region. Simultaneous to the drying of southern Mexico and Central America during the MSD, the North American monsoon region moistens as shown by the increased TWC and IMFC.

In turn, the IMFC and TWC anomalies associated with the end of the MSD period, depicted by the P2-MSD panel, show positive differences in the MSD region and negative anomalies southward, suggesting increased IMFC and TWC over southern Mexico and northern Central America, in agreement with the secondary increase in precipitation. Positive TWC and IMFC differences extend from the MSD region to the east into Cuba, the Caribbean Sea and the Gulf of Mexico. This moistening coincides with increased moisture divergence to the south of the MSD region in the East Pacific (120-90°W, 3-10°N) and decreased TWC.

Furthermore, a scatter plot of the mean changes to the IMFD, TWC and the CLLJ and their relationship to the synchronous variations in precipitation (Figure 6.23) confirm that these diagnostics are deeply related to the timings and strength of the three stages in the

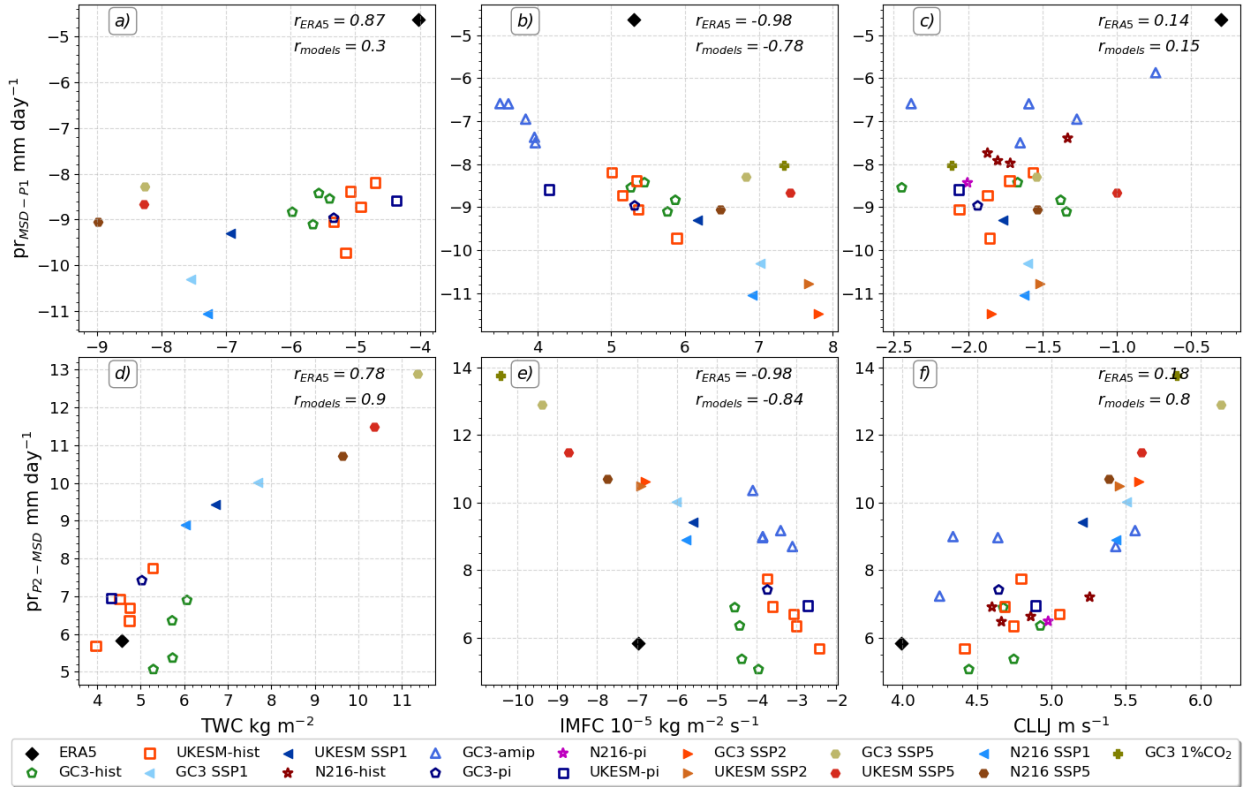


Figure 6.23: As in Figure 6.12, showing the scatter of mean changes (a-c) MSD-P1 and (d-f) P2-MSD periods, but using the (a, d) IMFD and (b, e) TWC in the MSD region and the (c, f) CLLJ on the x-axis and precipitation in the MSD region in the y-axis.

seasonal cycle of precipitation. The interannual variability of the precipitation differences between the first peak and the MSD periods in ERA5 are very well explained by the interannual variability of the TWC ($r = 0.87$) and the IMFC ($r = -0.98$) but less so by the CLLJ ($r = 0.14$). The inter-experiment variability in the MSD-P1 precipitation differences can largely be explained by the inter-experiment differences in IMFC changes during the MSD-P1 periods ($r = 0.78$). However, the changes in the CLLJ and IMFC in the simulations can not explain the precipitation differences between the runs in the MSD-P1 panels.

The changes from the MSD to the second peak of precipitation (lower row in Figure 6.23) in the simulations are very well explained by the mean variations to the CLLJ, the TWC and the IMFC. However, for the interannual variability of ERA5, only changes to the TWC and IMFC show significant and relatively high correlations. These results would suggest that variability in the CLLJ can explain several differences in the magnitude of the P2-MSD differences in the models, possibly through the modulation of the CLLJ on the

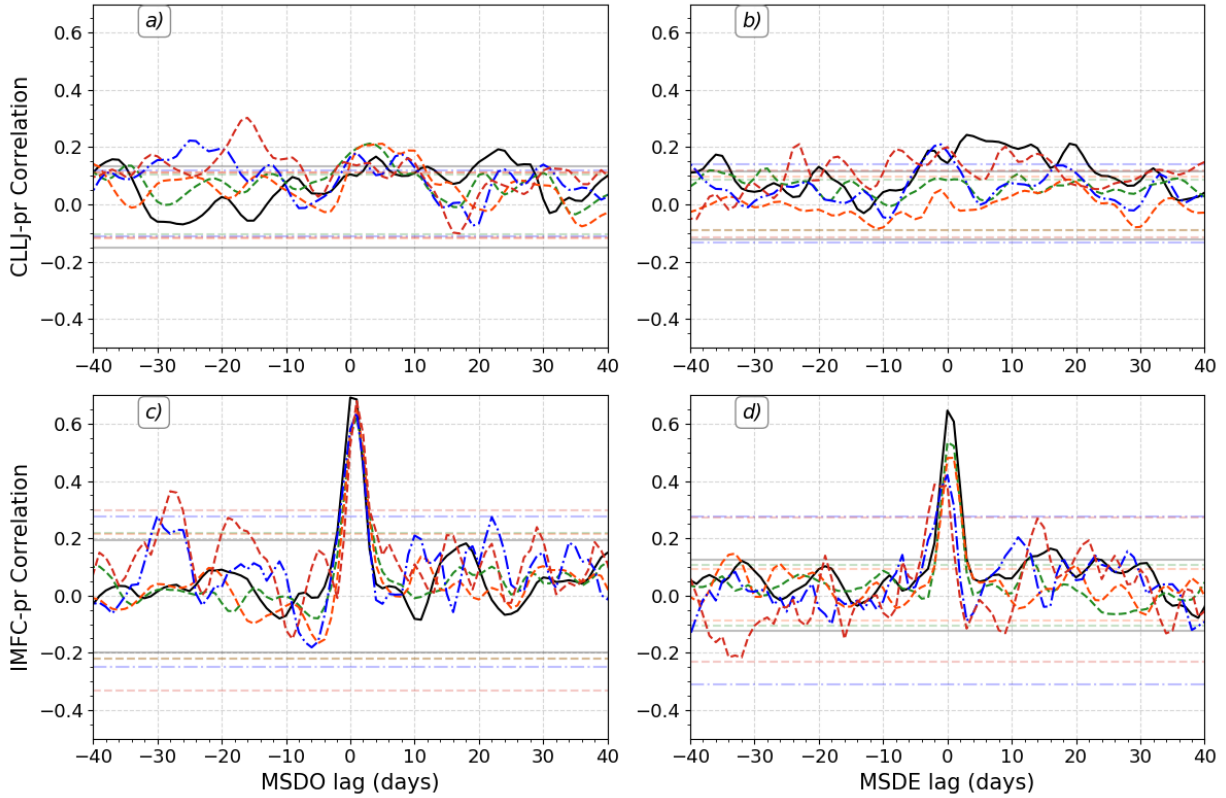


Figure 6.24: Lagged correlations between precipitation in the MSD and the (a, b) CLLJ, defined as the 925 hPa zonal wind averaged over the CSEA region, and (c, d) the IMFC over the MSD region. Correlations are shown with lags computed with respect to the (a, c) onset and (b, d) end dates.

TWC and the IMFD over the continent; nevertheless, the observed interannual variability of the CLLJ cannot explain the interannual variability in the strength of the second peak.

The synchronous relationship found in the previous scatterplot is further tested via lagged correlations, shown in Figure 6.24. These correlations do not show any evidence that the nature of the relationship between the CLLJ or the IMFC with precipitation over the MSD is of a lagged nature. In particular, the correlations of precipitation with the CLLJ are not higher than 0.3 at any lag and only become significant for a few days in some simulations. In particular, around the MSDE date, no correlation at negative lags is notably positive or significant which is at odds with the hypothesis that CLLJ is responsible for the end of the MSD.

However, the strength of the CLLJ may not be the relevant factor, but rather the influence of the CLLJ on the IMFC. The correlation of IMFC with precipitation shows a

strong positive correlation, both at MSDO and MSDE in reanalysis and models around lag 0, and similar results are found for TWC-pr correlations (not shown). However, there is little evidence that this relationship is of a lagged nature, as the correlations are not significant far away from the 0 lag.

6.7 A short look at the MSD through the lense of the moist static energy budget

The previous sections have tested three leading hypothesis for the Midsummer drought, with results suggesting that only elements of the CLLJ hypothesis can explain the interannual variability in the strength of the MSD in reanalysis, as well as in the differences between the CMIP6 experiments. However, changes to the CLLJ and IMFC appear to be unrelated to the strength and time of the onset of the MSD, which means that other processes are responsible for the start of the drier MSD period. To further explore the processes that control the start of the MSD, the moist static energy (MSE) budget is used in this section to disentangle how the column MSE budget terms vary over the wet season.

The computation of the MSE budget terms is done as described in section 3.3. The budget terms are obtained from daily-mean values at all available levels within the troposphere for reanalysis and climate model output. It should be noted that the radiative heating terms are not available from the CMIP archive on daily scales so a full budget was not feasible with model data. In turn, we focus on the vertical and horizontal advection of MSE, the total column MSE, the surface fluxes and the gross moist stability.

First, the seasonal cycle of the column budget terms, as well as the boundary layer or near surface MSE (h_b), is shown in Figure 6.25 with some quantities shown for the EP region and others for the MSD region. The vertical advection of dry (s) and moist (h) static energy shows a clear bimodal seasonal cycle, with two peaks at the start and end of the summer season, separated by a local minimum that occurs at the end of July or early August. The simulated vertical advection of MSE corresponds well with ERA5 during the wet season (JAS) for all the simulations, although the vertical advection of s is smaller in the historical and SSP1 experiments during the MSD and second peak periods. The vertical

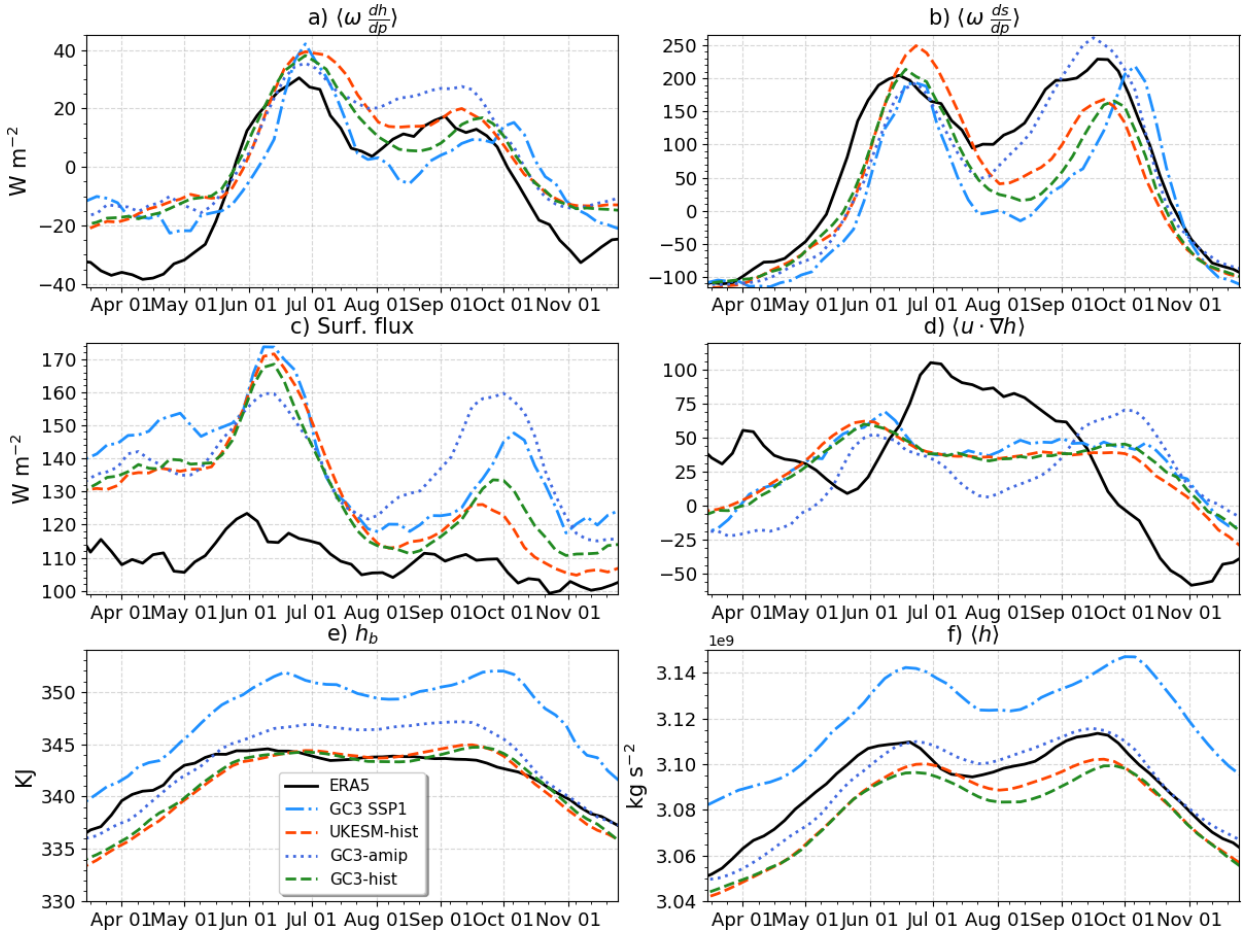


Figure 6.25: Pentad-mean seasonal cycle of the moist static energy budget terms. Vertical advection of (a) moist and (b) dry static energy, (c) the sum of the latent and sensible heat fluxes, (d) horizontal advection of MSE, (e) boundary layer MSE (h_b) and total column MSE ($\langle h \rangle$). The quantities in panels c,d were averaged over the EP region and the rest of the panels over the MSD region.

advection of s is not underestimated by the GC3 amip experiment during late summer, which has a wetter second peak as shown in previous sections.

The sum of the latent and sensible heat fluxes in the EP region show a clear bimodal signal in the experiments but not in ERA5. The experiments also show very large biases during both periods of peak precipitation in June and Sep-Oct. In late summer, this bias is particularly notable in the GC3 amip experiment. These biases in the surface fluxes in the EP are arguably one of the reasons for the very wet bias found in the EP ITCZ in these models.

One component of the theory by Karnauskas et al. (2013) involved the net shortwave part of the surface energy balance being notably different during the various stages of the

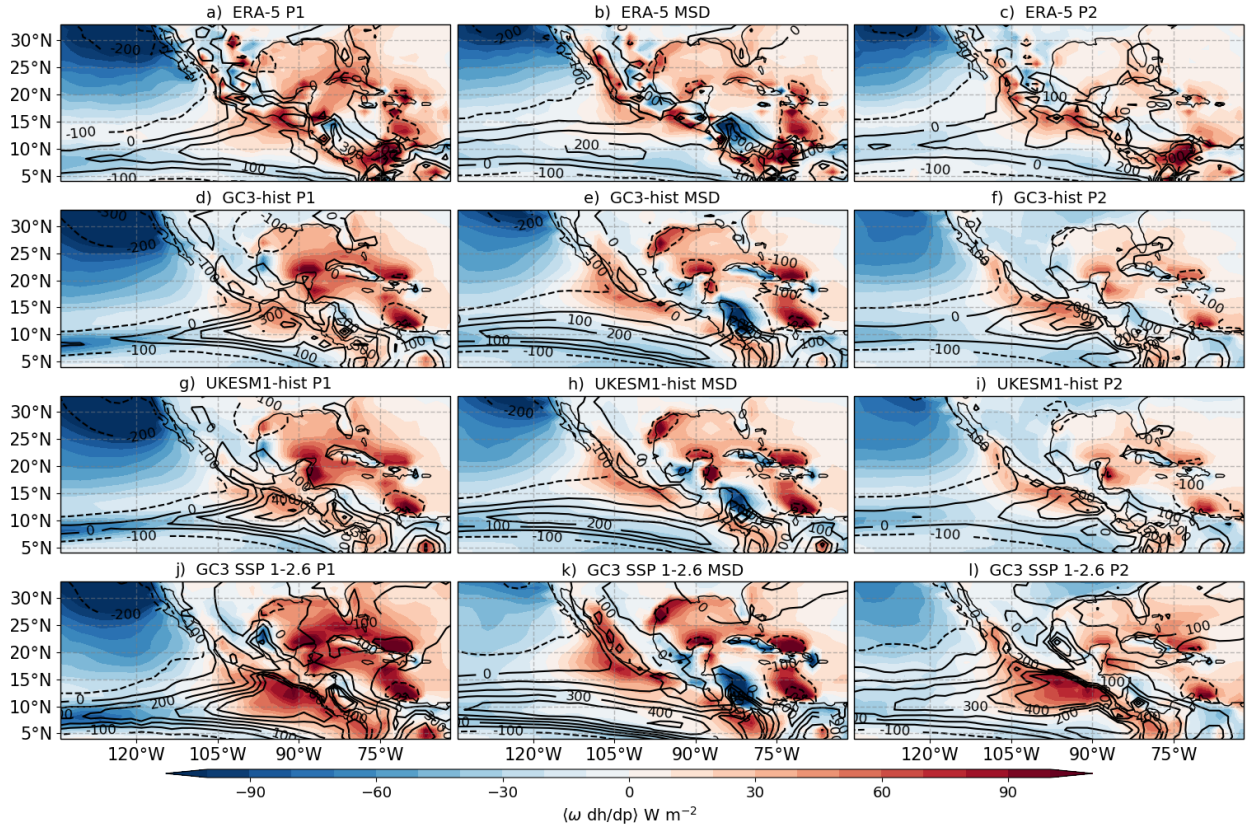


Figure 6.26: Composites of mean $\langle wdh/dp \rangle$ (shading in $W m^{-2}$) and $\langle wds/dp \rangle$ (contours in $W m^{-2}$).

MSD. A direct implication from this hypothesis is that the shortwave ultimately influences the surface or boundary layer MSE (Fig. 6.25e). However, in most of the simulations and ERA5, h_b in the MSD region follows a plateau-like seasonal cycle with a clear increase during spring, a plateau during summer and a sharp decrease in October at the end of the rainy season. The SSP1 experiment shows a decrease in h_b in August but this is fairly modest compared to the magnitude of the change in h_b at the end and start of the summer.

Similarly, the total column h shows a modest bimodal seasonality in reanalysis and simulations, i.e., $\langle h \rangle$ decreases at the midsummer. The low-emission scenario shows a notable increase in total column h compared to historical and pre-industrial experiments, and higher emission scenarios (SSP2 and SSP5) showed that total h scales with greenhouse forcing (not shown). One key aspect of this increase in total column h is that total precipitation is not increased uniformly over all the stages of the wet season (see Fig. 6.7).

The spatial distribution of the mean $\langle wdh/dp \rangle$ and $\langle wds/dp \rangle$ (Figure 6.26) during the

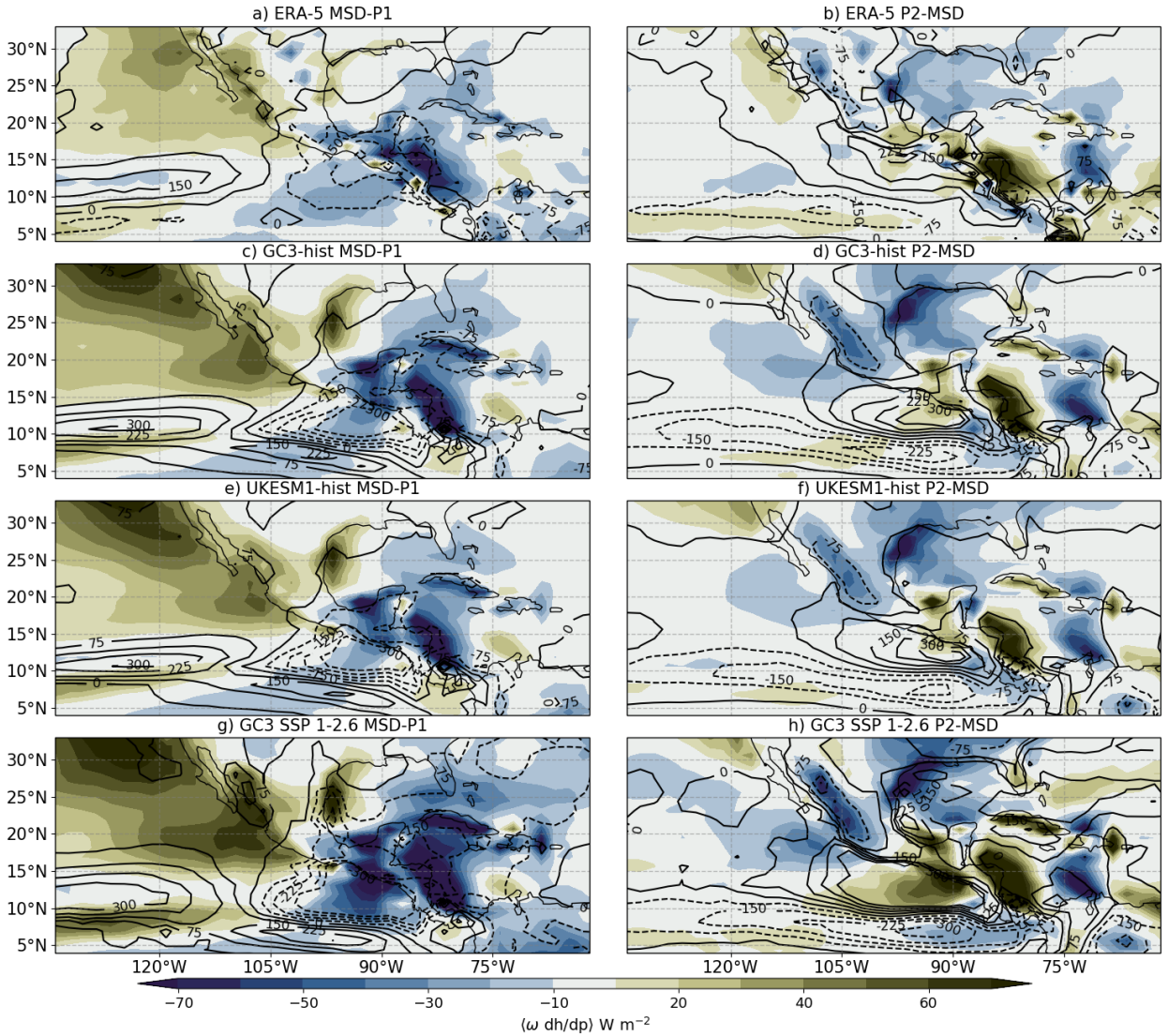


Figure 6.27: Composites of the differences (a, c, e, g) MSD-P1 and (b, d, f, h) P2-MSD of $\langle \omega dh/dp \rangle$ (shading in W m^{-2}) and $\langle \omega ds/dp \rangle$ (contours in W m^{-2}).

three stages of the MSD seasonal cycle show a good agreement between the experiments and reanalysis. The highest values of $\langle \omega ds/dp \rangle$ are found on the western coast of northern Central America, in the easternmost position of the ITCZ. Positive values of $\langle \omega dh/dp \rangle$ are found in the Caribbean Sea, the Gulf of Mexico and over the Mesoamerican region throughout the three stages of the MSD. Negative values of $\langle \omega dh/dp \rangle$ and $\langle \omega ds/dp \rangle$ are found over the coast of California throughout the wet season.

The changes to the $\langle \omega dh/dp \rangle$ and $\langle \omega ds/dp \rangle$ during the MSD periods are best illustrated in Figure 6.27, which shows the differences between MSD-P1 and P2-MSD. In the Mesoamerican

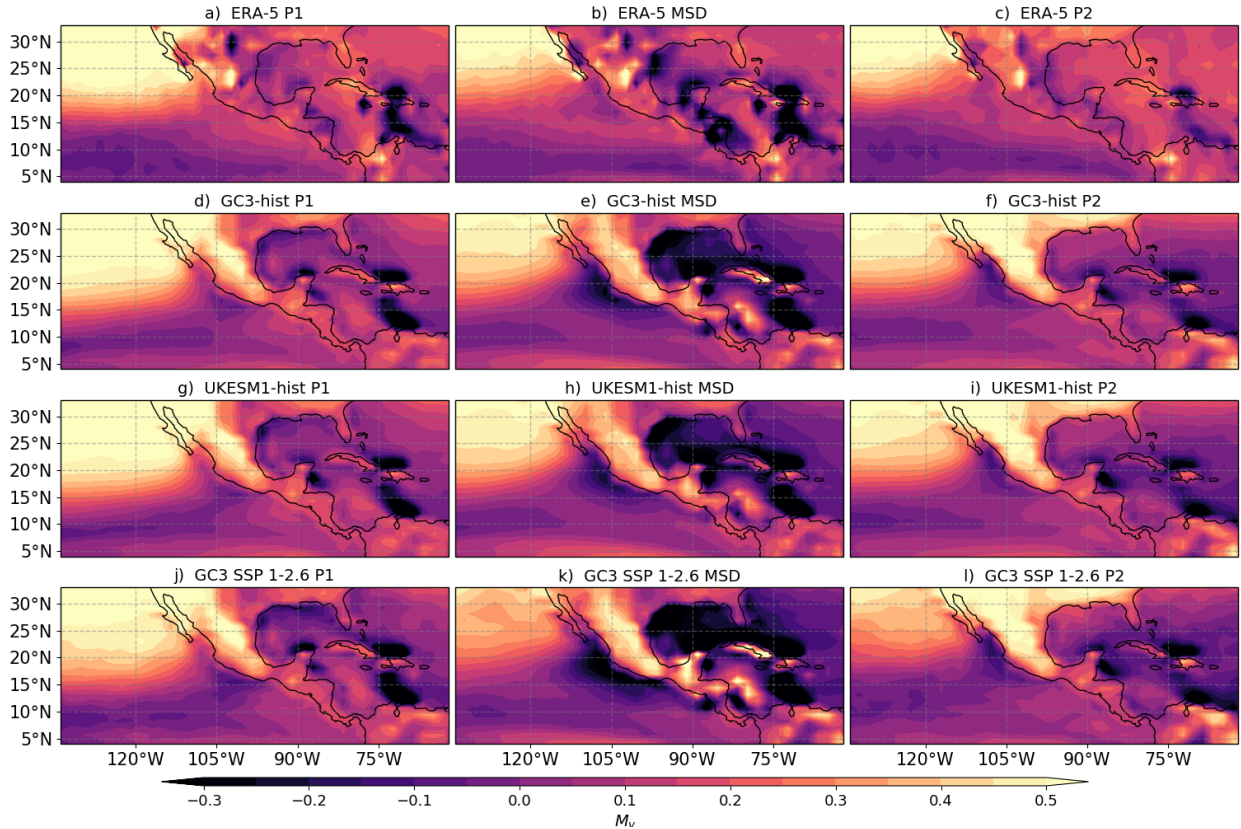


Figure 6.28: Composites of vertical gross moist stability (M_v) in the three stages of the Midsummer drought for ERA5 and three experiments.

region, $\langle \omega dh/dp \rangle$ and $\langle \omega ds/dp \rangle$ are reduced during the MSD period compared the first peak period, this difference is maximized right at the exit of the Gulf of Tehuantepec, in southwestern Mexico. Simultaneously, from the P1 to the MSD period, $\langle \omega ds/dp \rangle$ notably increases west of the Mesoamerican region near the 125°W region whereas $\langle \omega dh/dp \rangle$ increases in northern Mexico and in the Gulf of California.

At the end of the MSD, illustrated by the P2-MSD panels in Figure 6.27, $\langle \omega dh/dp \rangle$ and $\langle \omega ds/dp \rangle$ increase notably in the Mesoamerican region. Again, the maximum difference of $\langle \omega ds/dp \rangle$ is found in the Gulf of Tehuantepec region. The North American monsoon region show a decrease in both $\langle \omega dh/dp \rangle$ and $\langle \omega ds/dp \rangle$. Both for the P2-MSD and MSD-P1 panels, the experiments are able to reproduce the spatial patterns of these changes to these budget terms. Furthermore, the SSP1 experiment shows larger differences between the MSD stages compared to the historical experiments.

The normalized gross moist stability (NGMS) is a useful quantity to better understand

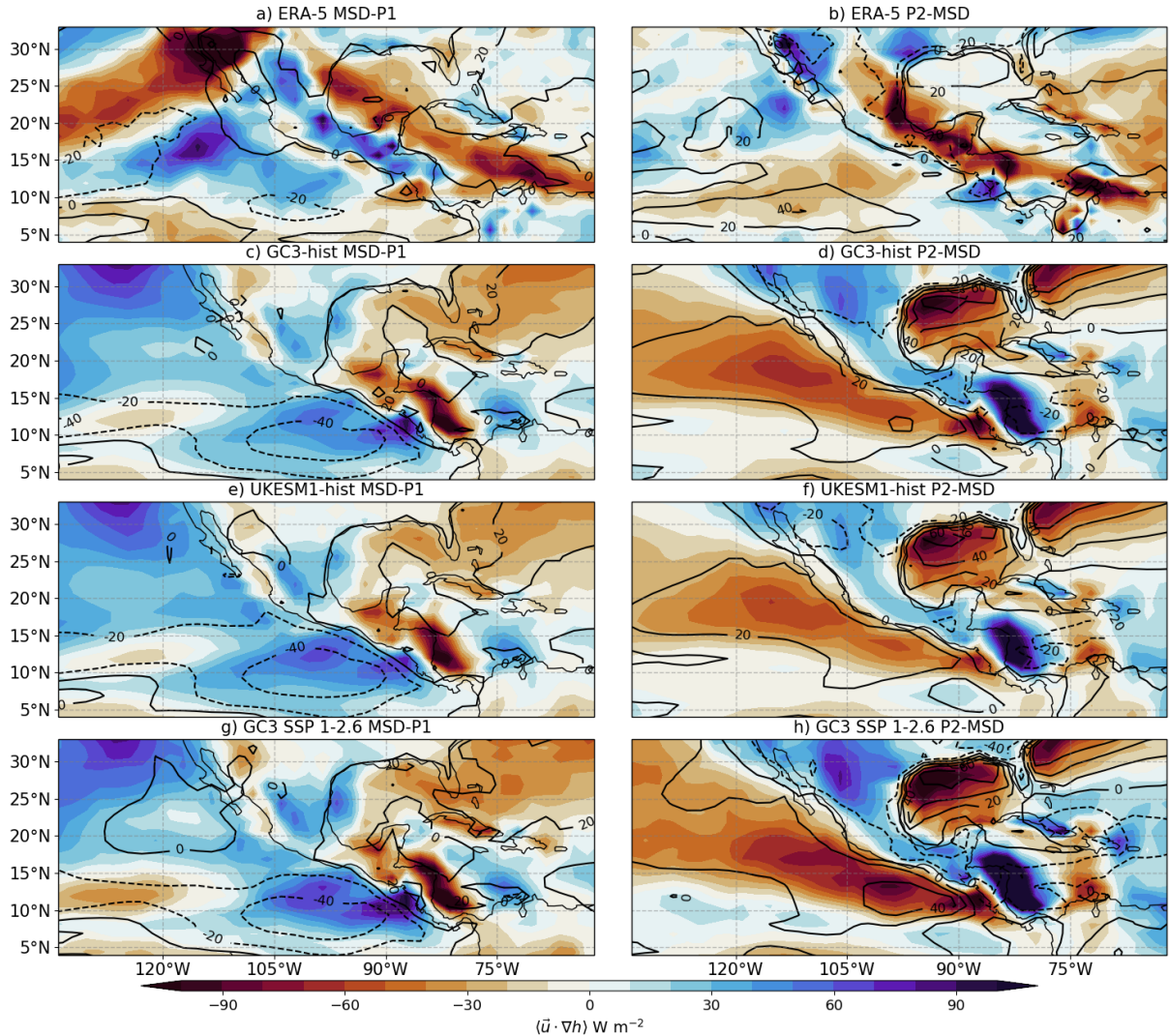


Figure 6.29: Composites of the differences (a, c, e, g) MSD-P1 and (b, d, f, h) P2-MSD of $\langle \vec{u} \cdot \nabla h \rangle$ (shading in W m^{-2}) and total surface fluxes (F) (contours in W m^{-2}).

how convection is redistributing h vertically (see equation 3.6). Figure 6.28 shows the temporal and spatial variability of the vertical component of the NGMS (M_v) during the three stages of the MSD. The reanalysis and the simulations show that M_v is generally close to 0 in the easternmost Pacific (5°N - 15°N) and into the MSD region, and positive on the western coast of Mexico and over the continental North America.

The most noteworthy variations of M_v associated with the MSD timings occur over the western coast of Mexico, the Gulf of Mexico and the Caribbean. From the first peak period to the drier MSD period, M_v decreases in these regions and then increases again from the dry period to the wetter second peak period. Negative and minimum M_v is then

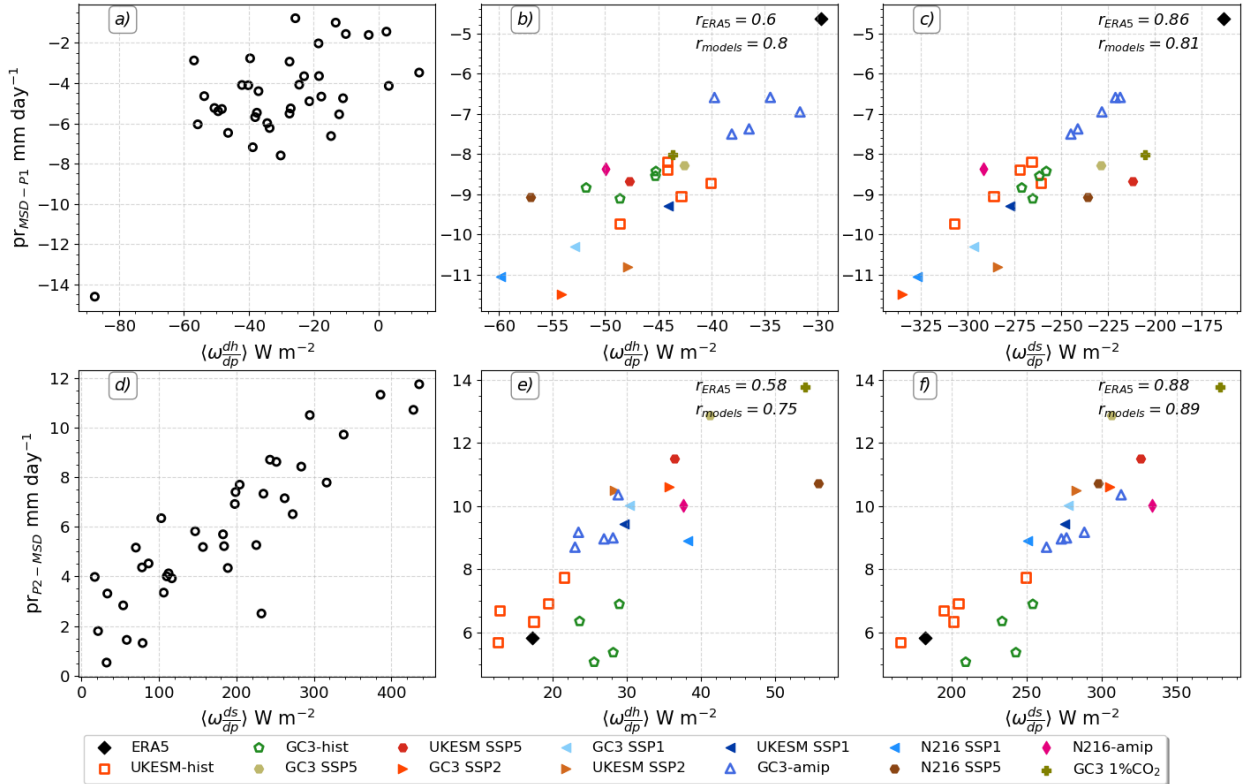


Figure 6.30: Scatterplot of the relationship between the area-averaged mean vertical advection of dry and moist static energy and precipitation over the MSD region. In panels a, d, each dot represents the differences in the mean values between a) MSD-P1 and (d) P2-MSD for precipitation in the y-axis and vertical advection of h and s in the x-axis. In the rest of the panels, the differences are shown for the dataset-mean for all years in each dataset.

found during the MSD period over most of the so-called Intra-Americas Seas region. This result is important because these changes point to seasonal variations in the relationship between convection and the large-scale dynamics (Raymond et al., 2009), including the shape of the vertical velocity profile.

The horizontal advection term and the surface fluxes also show notable differences associated with the MSD timings (Figure 6.29). In the MSD-P1 period, decreased surface fluxes in the easternmost Pacific Ocean are observed in the three simulations and, to a lesser degree, in ERA5. These differences suggest that in the models, surface fluxes decrease as precipitation decreases from the wet first peak period to the dry MSD period. In the simulations, these negative surface flux anomalies are collocated with negative differences of the horizontal advection of MSE term.

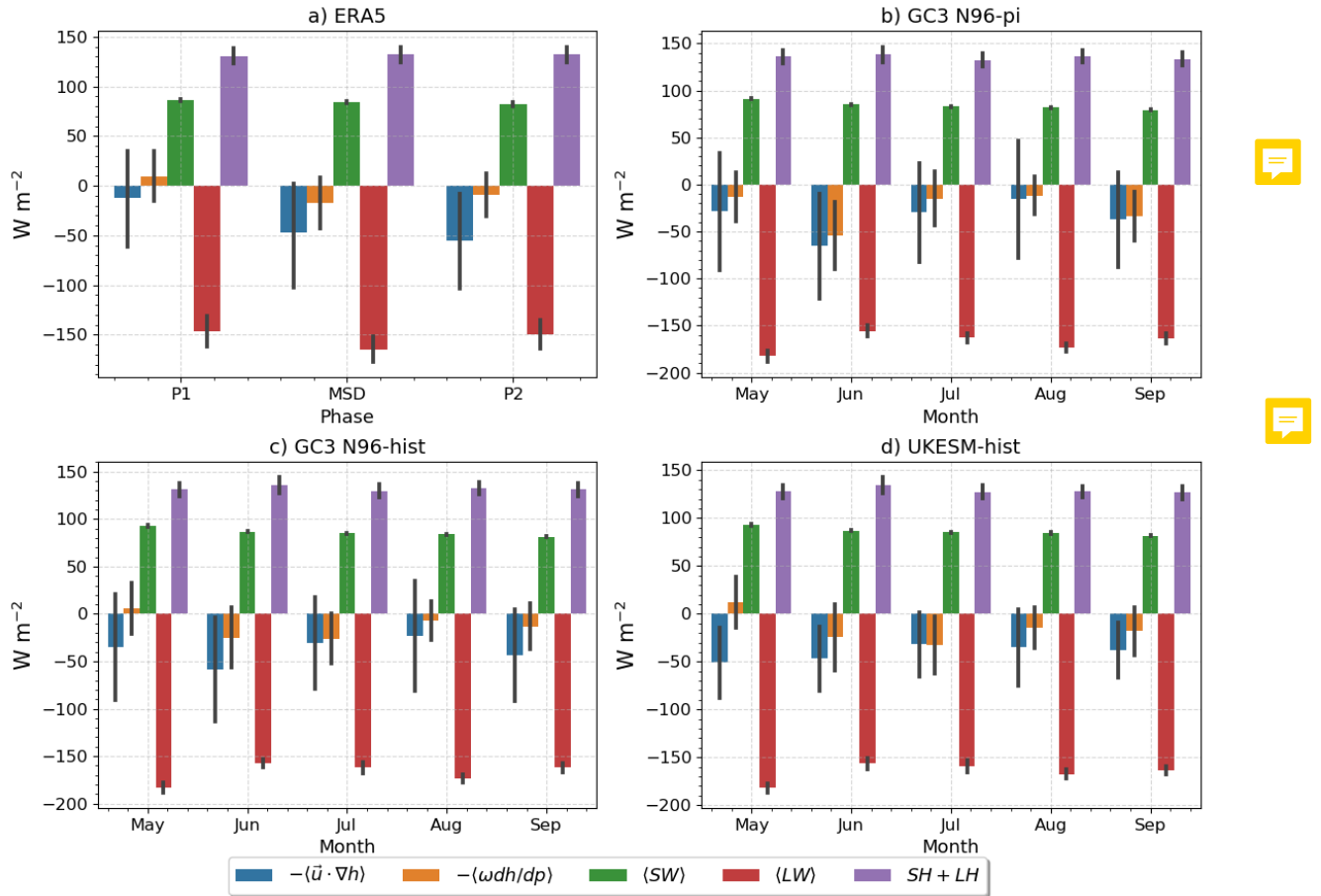


Figure 6.31: Barplots of the area and time-averaged MSE budget terms: horizontal advection ($\langle \vec{u} \cdot \nabla h \rangle$) and vertical advection ($\langle wdh/dp \rangle$), longwave ($\langle LW \rangle$) and shortwave($\langle SW \rangle$) and the sum of sensible (SH) and latent heat (LH) fluxes. (a) shows the budget terms computed from ERA5 in the MSD region in the P1, MSD and P2 periods. (b-d) show the monthly-mean values of the budget terms.

A key question then is how the MSE budget equation is balanced in the different stages of the seasonal cycle, i.e., which terms balance the horizontal and vertical advection of MSE during the early and late wet periods and in the MSD period. Figure 6.31 shows the mean values of each budget term in the MSD in ERA5 and the simulations. The results in the simulations are shown per month because the radiative heating data from the CMIP6 archive was only available for monthly-mean frequencies.

In ERA5 (Fig. 6.31a), the positive contributions of MSE from the shortwave heating and the surface fluxes are balanced mostly by the negative contribution from the longwave heating (radiative cooling of the column) and to second order by the horizontal and vertical

advection terms. The differences in the budget terms between the P1, MSD and P2 periods are most pronounced for the vertical and horizontal advection terms which total contribution increases during the MSD compared to the other two periods. However, from P1 to the MSD stage, the longwave radiative heating notably decreases and increases again from the MSD to P2 periods whereas the shortwave heating term appears to change very little between the stages of the rainy season.

In the CMIP6 simulations (Fig. 6.31b-d), a similar balance is observed with the largest contributions arising from the terms of radiative heating and surface fluxes. From May to September some seasonal variations in each term are observed, for example, stronger longwave cooling in May than in June-July. The vertical advection term also increases notably during the early rainy season (June-July) compared to the rest of the wet season. As in ERA, the contribution from the vertical advection term increases during the MSD with minima found in June or July in all the simulations. The horizontal advection increases during the months of the two peak of precipitation (May and September) and decreases during the MSD.

The scatter of the relationship between precipitation and the vertical advection of dry and moist static energy during the wet season (Figure 6.30) indicates that the shape of the vertical profile of the vertical velocity is strongly linked to precipitation variations, both in ERA5 as in the simulations. Figure 6.30a, d shows that the interannual variability of vertical advection of dry and moist static energy in ERA5 is strongly related to interannual variations in the precipitation changes during the MSD. Negative differences of $\langle \omega dh/dp \rangle$ and $\langle \omega ds/dp \rangle$ are observed in MSD-P1 panel, in agreement with the previous composite analysis whereas increases of these terms occur from the MSD period to the second peak period in ERA5 and in the experiments. Specifically, $\langle \omega ds/dp \rangle$ is the term that best explains interannual variability of the strength of the MSD, measured by the difference MSD-P1 in ERA5. The budget analysis shows that the variability of the horizontal advection and longwave heating terms within the rainy season is stronger than for the shortwave heating and surface fluxes. This evidence suggests that LW CRE and moisture transport may be more important than surface fluxes of total shortwave incoming to the troposphere, which supports the mechanism that links the CLLJ to the precipitation in the MSD. These budget

terms could also be interpreted as evidence that cloud-radiative feedback mechanism and the solar declination angle are less likely to explain the MSD.

6.8 Summary and discussion

The Midsummer drought (MSD) is a key element of past, present and future climates of southern Mexico, northern Central America and the Caribbean with important implications for agriculture and water management (Hellin et al., 2017; de Sousa et al., 2018; Harvey et al., 2018). However, a complete description of the physical mechanisms that explain the spatial and temporal variability of the MSD is not yet clear. This lack of understanding is magnified when investigating the MSD in global climate models that are used for projections of future climate, as little is known as to why only some models can reproduce the MSD (Ryu and Hayhoe, 2014).

This chapter tackled these shortcomings in the literature by investigating the processes that are linked to the MSD in CMIP6 experiments of the MOHC models, an investigation that was motivated by the two previous chapters which showed that these models reasonably reproduced the main features of the MSD signal. The first contribution of this chapter is the diagnosis of MSD timings and patterns on a sub-monthly scale, a step forward from previous studies that diagnosed the MSD on monthly-mean timescales, possibly missing key information in the process. For this purpose, the wavelet transform method (WT; Chapter 5) was used to determine the timings of the MSD on a 5-day (pentad) scale.

The WT method proved useful to separate the wet season in each dataset into three stages: the first and second peak periods (P1 and P2) and the drier period (MSD). This approach using the WT method was able to reproduce the so-called MSD pattern reported in previous studies (Zermeño-Díaz, 2019; Zhao et al., 2020) using various diagnostics such as OLR, ω and the low-level wind flow. This pattern is characterised by strong changes to the zonal wind flow crossing from the Caribbean Sea into the easternmost Pacific Ocean, as well as by anomalous vertical velocities found west of the coast at around 125°W, in agreement with previous findings (Herrera et al., 2015; Zermeño-Díaz, 2019).

The chapter first evaluates key climate features in the region such as the seasonal cycle of the Caribbean Low-Level Jet (CLLJ) and East Pacific SSTs. Results show that the simulations agree well with the observed seasonal cycle and that the experiments show very similar MSD patterns to observations. The following sections in the chapter test three of the leading hypotheses put forth to explain the MSD, this investigation is the second key contribution from this chapter. Each hypothesis is evaluated using the WT method in two different ways. The first question was whether a hypothesis could explain the interannual variability in the strength and timing of the MSD in ERA5. The second approach focused on the CMIP6 experiments and aimed to test whether the elements of each hypothesis could explain the differences in precipitation at each stage of the seasonal cycle between the realizations.

The first mechanism proposed by Magaña et al. (1999) argues that SST-cloud-radiative feedbacks explain the MSD. In this hypothesis, the SSTs in the East Pacific should also exhibit a bimodal seasonal cycle, with a second peak in SSTs found in September. Even though Magaña and Caetano (2005) analysed this for a specific year and found no evidence of a second peak in SSTs, no study to date robustly evaluated whether observations or models confirm their hypothesis. This chapter provides evidence that in ERA5, SSTs not only do not increase at the later stages of the summer but rather decrease. While the seasonal cycle in the simulations do show a two peak structure, the composite analysis shows that as precipitation transitions from the drier MSD to the second peak periods, SSTs decrease in the Pacific coast of Central America, in contrast to the prediction of the SST-cloud feedback mechanism. No evidence is found that the variability of the East Pacific SSTs is directly associated with the precipitation over the MSD region in ERA5 or in the CMIP6 experiments.

The feedback mechanism also suggests that the second peak is a result of a second increase in downwelling shortwave radiation at the surface that results from cloud cover during the drier MSD. The solar declination angle mechanism of Karnauskas et al. (2013) also suggests that shortwave absorption has two peaks in the seasonal cycle, which leads to the two precipitation peaks. The shortwave absorption at the surface does show a bimodal seasonal cycle in ERA5 and in the simulations, as predicted by these two mechanisms.

However, the interannual variability in ERA5 and inter-experiment differences in the absorbed shortwave at the different stages of the seasonal cycle cannot explain the changes over precipitation. Moreover, no significantly positive correlation is found between the shortwave absorption at the surface and precipitation at any lags but rather a strong anticorrelation signal is found, which is a result of stronger convective activity leading to more cloud cover and less downwelling shortwave at the surface. Therefore, while this chapter found some evidence of strong correlations between SW and precipitation, there is little evidence found that the SW drives precipitation, as argued by the solar declination angle mechanism.

Cloud-radiative effects (CRE) are known to be key for precipitation in monsoon regions and the central argument of Magaña et al. (1999) is that precipitation and CRE (at the surface) are part of a feedback mechanism that explains the MSD. This chapter presents the first regional evaluation of the net CRE at the surface as well as the long-wave and short-wave contributions. The net CRE at the surface over the wet season is negative following the regions of maximum precipitation, i.e., the East Pacific ITCZ and the MSD region reaching values of -100 W m^{-2} over the core ITCZ region in both the models and ERA5.

The net CRE is dominated by the short-wave component that acts to cool the surface due to the effect of cloud cover associated with convection. Over the MSD region, the net, short-wave and long-wave CRE at the surface show a bimodal regime that closely follows the evolution of precipitation. Finally, an experiment part of CFMIP in which the long-wave effects of clouds are turned-off from the radiative scheme shows that the longwave radiative effects are key for monsoon precipitation in Central America and southern Mexico, where long-wave effects are decoupled from the simulation, shows that the long-wave component of CRE are key for sustaining the monsoon circulation and precipitation irrespective of the bimodal MSD signal.

This section showed that CRE have a strong seasonal cycle associated with the MSD in ERA5 and the MOHC experiments. However, further research into CRE in present and future climates in the region is warranted, for example, further work could include a detailed examination of the CRE at the top of atmosphere and at the surface in the MSD, particularly to understand the relationship between CRE and the large-scale circulation,

and how this relationship is different over land in Mesoamerica than over the Caribbean Sea and the East Pacific Ocean.

One alternative hypothesis is that the MSD is caused by the modulation of the transport of moisture by the CLLJ (Herrera et al., 2015; Zermeño-Díaz, 2019; Martinez et al., 2019). The integrated moisture flux convergence and the total column water content are found to better explain observed and simulated differences in precipitation, compared to the previous hypotheses. Evidence is presented that the low-level wind flow variations on the west coast of Central America is linked to the variations in the strength and direction of the CLLJ. Changes to the CLLJ and moisture convergence allow skillful predictions of precipitation changes at the end of the MSD period but these are less skilful for changes at the start of the MSD.

A moist static energy (MSE) budget is implemented to investigate whether this technique could provide additional insight into the mechanisms of the MSD. The total column MSE, as well as the vertical advection terms of the budget show a clear bimodal signal that closely follows that of precipitation. The vertical advection of dry and moist static energy are found to have the strongest relationship to the interannual variability and the inter-experiment differences of precipitation in the MSD region.

In particular, $\langle \omega ds/dp \rangle$ is able to explain interannual variability in ERA5 as well as the precipitation differences between the range of experiments considered in this chapter. While these results do not directly point to any theory or hypothesis, the strong correlations in reanalysis and simulations indicate that MSE budgets would be useful in future research to better understand the key mechanism underpinning the MSD. Specifically, this result points to a possible modulation of the strength of convection by the shape of the vertical velocity profile, which is the key modulator of these terms. How the vertical velocity profile changes during the rainy season, and whether there are notable trends in ERA5 or significant changes between historical and Scenario experiments warrants further research.

7

The tropical route of QBO teleconnections in UKESM1 and HadGEM3

Evidence in a previous chapter suggests that the QBO plays a role in tropical ENSO teleconnections associated with the Walker circulation in the CMIP6 experiments of the MOHC models. In this chapter, the influence of the QBO on the tropical mean circulation and teleconnections is more closely examined in these models. An analysis of the CMIP6 experiments from the MOHC shows how the tropical circulation, monsoons and the ITCZ are influenced by the QBO. Results are discussed in the context of existing observational evidence of QBO tropical teleconnections.

7.1 Introduction

Long-distance effects or teleconnections associated with the stratospheric quasi-biennial oscillation (QBO) have been well documented in the subtropics and extratropics, for example for the stratospheric polar vortex (Holton and Tan, 1980; Anstey and Shepherd, 2014; Lu et al., 2020), the subtropical jets (Garfinkel and Hartmann, 2011; Hansen et al., 2016) and the North Atlantic Oscillation (Hansen et al., 2016; Gray et al., 2018; Andrews et al., 2019b). Observational and modelling evidence suggests that there is also a tropical route of influence of the QBO to surface climate, for example, over tropical convective phenomena such as

monsoons (Giorgetta et al., 1999; Liess and Geller, 2012), the ITCZ (Gray et al., 2018), tropical cyclones (Gray, 1984; Chan, 1995) and most recently, the Madden-Julian Oscillation (MJO) (Lee and Klingaman, 2018; Wang et al., 2019; Martin et al., 2020), see section 2.5.2.

Several observational and modelling studies have found evidence of QBO-related influence over convective activity in monsoon regions, such as in the South American, East Asian, Australian and Indian monsoons (Giorgetta et al., 1999; Collimore et al., 2003; Liess and Geller, 2012; Gray et al., 2018). In observations, these responses have been found in satellite-derived fields such as cloud height, occurrence and out-going longwave radiation (Collimore et al., 2003; Liess and Geller, 2012), as well as in surface precipitation diagnosed from gridded datasets or from reanalysis (Gray et al., 2018). However, the observational evidence shows zonally asymmetric impacts, indicative that the impact of the QBO depends on longitude, which has been explained (e.g. by Collimore et al., 2003; Liess and Geller, 2012) through a QBO modulation of the Walker circulation.

In models, Giorgetta et al. (1999) finds that boreal summer monsoon regions exhibit a significant response in cloudiness to QBO winds within the GCM ECHAM4. Nie and Sobel (2015) further finds in a modelling framework that the influence of the QBO may depend on the strength of convection and SST forcing, suggesting a non-linear effect of the QBO over a convective profile. In CMIP5/CMIP6 models, only a relatively small number of studies have analysed tropical QBO teleconnections (Serva et al., submitted), as most studies focus on the polar and subtropical routes (Richter et al., 2020; Anstey et al., 2021).

Although the polar and subtropical routes of influence of the QBO to the surface are relatively well established, the impact of the QBO over tropical convective phenomena remains less well understood for various reasons. First, the short observational record limits the confidence in any analysis that seeks to investigate differences between the two QBO phases in a 30-40-yr long dataset. Tropical circulation variability on QBO time-scales is largely dominated by ENSO, which makes it difficult to separate the effects of ENSO and the QBO, other than by multi-variable regression analysis as in Gray et al. (2018). In addition, there is also evidence that ENSO and convection in the Pacific influence the QBO, so there is a two-way relationship that would difficult a separation of cause and effect (Schirber, 2015; Christiansen et al., 2016).

In addition, the specific physical mechanisms through which the QBO could influence tropical convection at the grid-scale or the large-scale tropical circulation are also not well understood. While early studies (Gray, 1984; Collimore et al., 2003) suggest that changes to the vertical wind shear or static stability in the upper-troposphere lower-stratosphere (UTLS) region are the cause of these teleconnections, there is a lack of evidence in the literature to support any mechanism over another. As such, studies have struggled to pin-point direct impacts and mechanisms by which the QBO may modulate any aspect of tropical climate.

This chapter investigates QBO tropical teleconnections in the pre-industrial control experiments of the MOHC UM: GC3 N96-pi, GC3 N216-pi, UKESM-pi. These simulations are ideal to investigate variability associated with the QBO because these experiments are very long integrations where external forcing is kept constant within the simulation and the UM is a model that reasonably simulates the QBO (Richter et al., 2020). The remainder of this chapter is presented as follows. First, the data and methods used are described, after which the results analysing the QBO impacts over the seasonal precipitation and surface temperatures is given. Then, a more detail investigation on the effects on the East Pacific and Atlantic ITCZs is presented and finally, the impacts over ENSO, the Indian Ocean and the Walker circulation are given. A discussion is given at the end of the chapter.

7.2 Methods and data

The observational datasets and reanalysis (ERA5) used in this chapter are described in section 3.1 and consist of the HadSST3 dataset for SST, GPCP for precipitation and ERA5 for the rest of the diagnostics that include the zonal and meridional winds, air temperature, etc.

7.2.1 CMIP6 data

The three pre-industrial control experiments of the MOHC submitted to CMIP6 are used in this chapter: GC3 N96-pi, GC3 N216-pi and UKESM-pi. UKESM-pi and GC3 N96-pi are run with the same resolution (N96) of $1.875^\circ \times 1.25^\circ$ and GC3 N216-pi is considered a medium-resolution simulation (N216) with atmospheric resolution of $0.83^\circ \times 0.56^\circ$. The period of 1850-2350 is used for GC3 N96-pi and GC3 N216-pi and 2050-2650 for the UKESM-pi.

7.2.2 Indices

The indices for ENSO and the QBO are diagnosed exactly as in section 4.2, i.e., the 70-hPa zonal mean zonal wind index is used for the QBO with a threshold of 2 m s^{-1} for each phase and the EN3.4 index is used with a threshold of ± 0.65 to define positive or negative events.

7.2.3 Analysis techniques

Composite analysis is the preferred technique used throughout this chapter. For each QBO or ENSO phase, composite samples are drawn for specific seasons using the indices and definitions mentioned above. Statistical significance is estimated in various ways, in some cases through standard Student or Welch t-test's where specified, and in some other cases a randomised resampling or bootstrapping method is also implemented in several sections of the chapter. The bootstrapping method is performed in all cases by drawing random samples from the entire simulation and repeating the process 10,000 times to evaluate the likelihood of obtaining a relationship by chance.

Linear regression analysis has proven useful to understand the effect of one or more aspects of the climate over a region or a time-series, and was used to investigate the surface impacts of the QBO in observations by Gray et al. (2018). A simple linear regression model can be written as:

$$Y(t) = X_0 + X_i(t)\beta_i + \epsilon, \quad (7.1)$$

where Y is the measured or dependent variable, X_0 is a constant coefficient, β_i is the regression coefficient between X_i and Y and ϵ represents random error or a residual. A multivariate regression model can be used to study the joint effect of two or more predictors over a variable (Y) such that the model can be written as:

$$Y(t) = X_0 + \sum_j^N X_j(t)\beta_j + \epsilon \quad (7.2)$$

where $X_j(t)$ is any predictor with an associated regression coefficient β_j . As in previous studies (Gray et al., 2018; Misios et al., 2019), the regression coefficient can be rescaled to evaluate the total effect that a predictor (X_j) can have on the variance of the measured

variable (Y) using the standard deviation (σ_j) and the maximum ($X_{j,max}$) and minimum ($X_{j,min}$) values of X_j so that the rescaled coefficient β'_j can be written as:

$$\beta'_j = \beta_j \frac{X_{j,max} - X_{j,min}}{\sigma_j}. \quad (7.3)$$

7.3 Teleconnections in the pre-industrial control experiments

Surface impacts of the QBO in the tropics have scarcely been investigated in CMIP models, as most studies focus on the general representation of the QBO (e.g Schenzinger et al., 2017; Bushell et al., 2020), or the extratropical teleconnections (e.g. Anstey et al., 2021; Dimdore-Miles et al., 2021). However, studies that have investigated teleconnections between the QBO and tropical convective phenomena in relatively [novel](#) GCMs (e.g. Lee and Klingaman, 2018; Martin et al., 2021; Serva et al., submitted) have found that model biases in representing the variability of temperature and winds in the tropopause layer may hinder a possible interaction between the QBO and tropical convection.

This section examines more closely how the MOHC piControl experiments simulate the effect of the QBO over seasonal-mean precipitation, monsoons and the ITCZ. The three simulations chosen use the same model setup, with constant year 1850 forcing, but differ in their horizontal resolution or the treatment of aerosol-chemistry processes (see section 3.2).

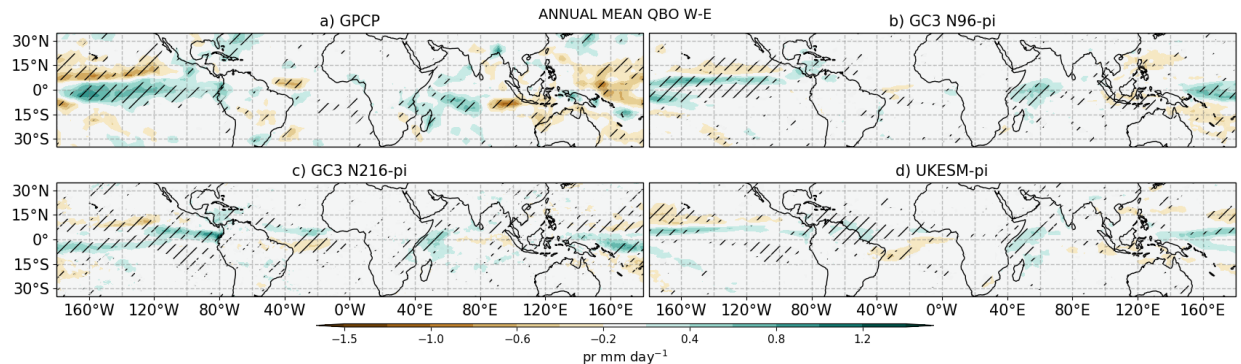


Figure 7.1: Annual mean precipitation difference between QBO W-E phases in (a) GPCP, (b) GC3 N96-pi, (c) GC3 N216-pi and (d) UKESM-pi. Hatching denotes statistical significance to the 95% confidence level using bootstrapping with replacement for each composite sample.

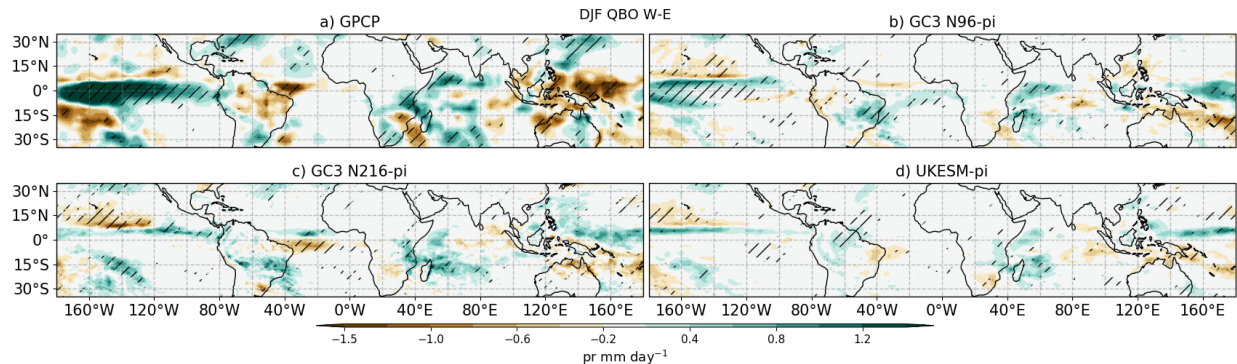


Figure 7.2: As in Figure 7.1 but for DJF.

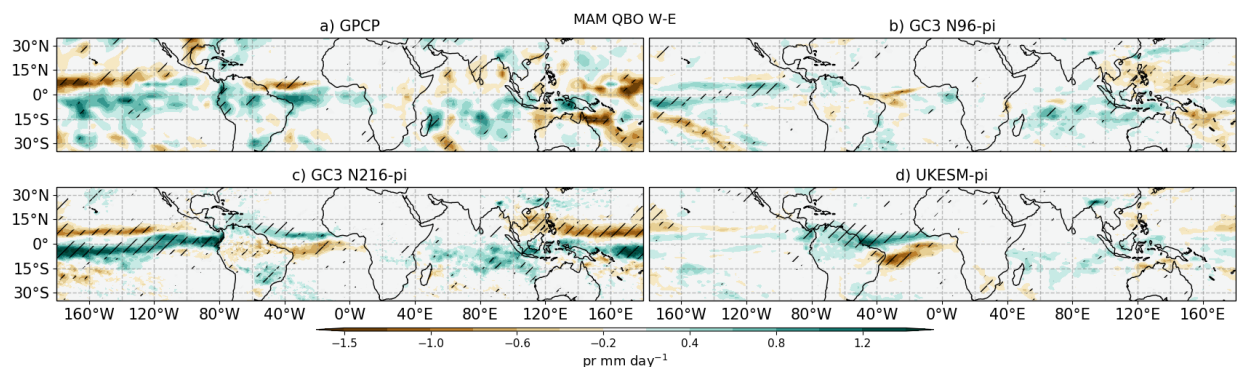


Figure 7.3: As in Figure 7.1 but for MAM.

7.3.1 Seasonal variability

The composite difference in annual mean precipitation between QBO W and E phases (Figure 7.1) shows that in observations (GPCP) the tropical Pacific, equatorial Atlantic and the Indian Oceans are the regions of possibly largest influence of the QBO, which agrees with previous studies (Liess and Geller, 2012; Gray et al., 2018). The three GCM simulations agree well with the pattern in GPCP, as all three simulations show a positive difference (QBO W-E) in the Central Pacific and the Indian Ocean, albeit the differences are smaller in the simulations. However, the patterns and magnitudes of the impacts become larger when analysed over specific seasons.

For example, during DJF (Figure 7.2), the pattern over the Central Pacific is stronger in GPCP and the simulations relative to the annual mean difference. The positive difference in the western Indian Ocean and the South Pacific Convergence Zone is also observed in this season and is significant in all the datasets. Results in GC3 N216-pi suggest a weakening of

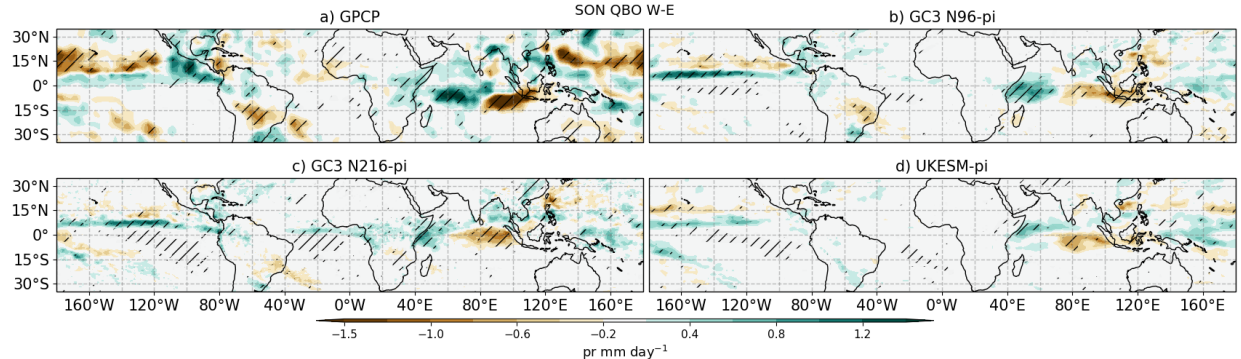


Figure 7.4: As in Figure 7.1 but for SON.

the Atlantic ITCZ as in GPCP, whereas UKESM-pi and GC3 N96-pi show little and not significant responses in that region. The response in the East Pacific during DJF matches the results of Serva et al. (submitted), and suggests a southward shift of the ITCZ.

Similarly, during MAM (Figure 7.3), the strongest response arises in the East Pacific and Atlantic ITCZ regions. In GC3 N216-pi the East Pacific ITCZ is shifted southwards whereas in the Atlantic the ITCZ is displaced northward. UKESM-pi agrees with the northward shift of the Atlantic ITCZ and suggests a wetter northern South America during QBO W than E. In GC3 N96-pi, the differences are smaller and the most noteworthy pattern is found in the Western Pacific.

In boreal fall (Figure 7.4), all datasets show relatively large and significant differences in the Indian Ocean, characterized by a dipole of wet anomalies to the west and dry anomalies to the east. These dipole anomalies may be an indication that the QBO influences the Indian Ocean Dipole (IOD), characterized by a zonal gradient of SSTs in the Indian Ocean. In addition, results for GC3 N96-pi and GC3 N216-pi suggest a similar response in the Central and Eastern Pacific as in the other seasons, characterized by a wet anomaly at about 10°N .

Finally, the JJA seasonal mean pattern (Figure 7.5) shows a weak response in GPCP whereas the simulations show a number of significant differences. Specifically, the three experiments suggest a wet anomaly in the Caribbean Sea and the Indian Ocean; the former, likely related to the northward shift of the Atlantic ITCZ observed in the same season particularly in UKESM-pi. West of the Caribbean Sea, in the easternmost Pacific Ocean a seemingly southward shift of the ITCZ is observed with a negative precipitation response on

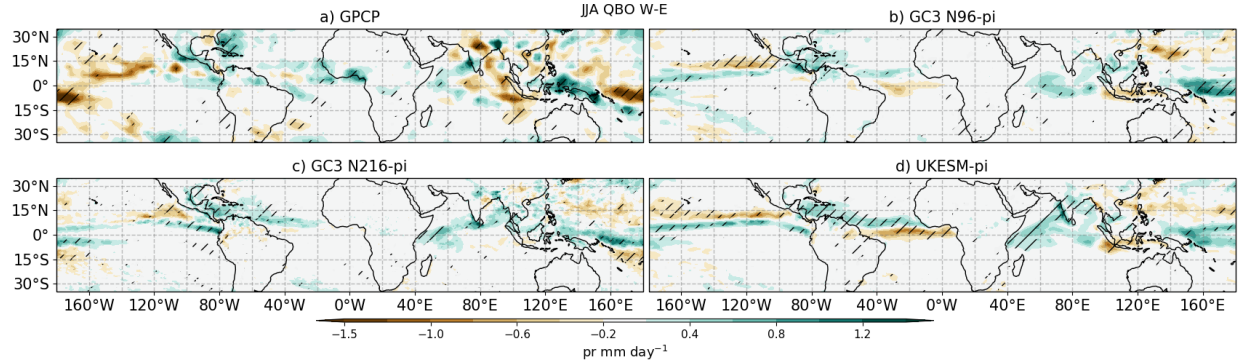


Figure 7.5: As in Figure 7.1 but for JJA.

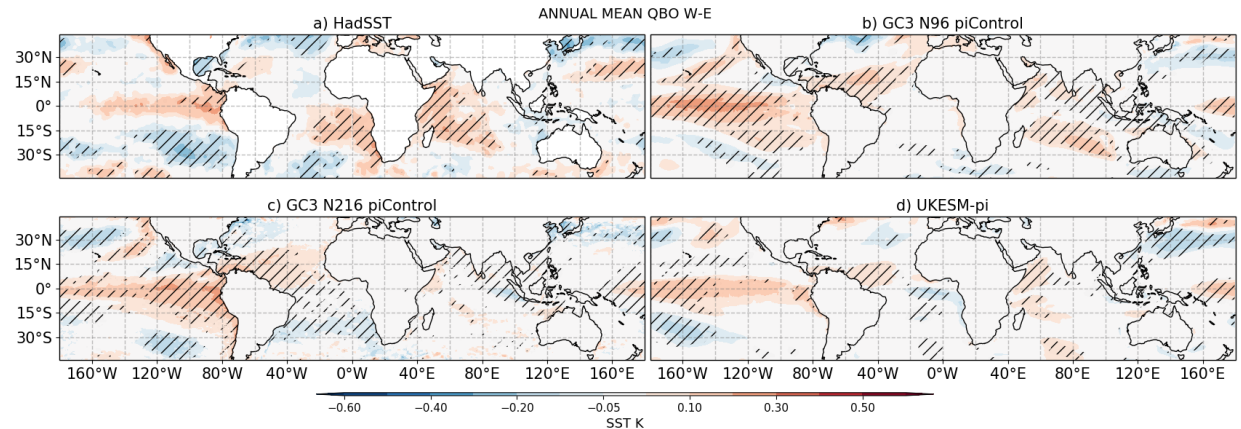


Figure 7.6: As in Figure 7.1 but for SSTs.

the western coast of Mexico. A wetter Indian Ocean is observed in all the simulations and in UKESM-pi the wet anomaly extends over land into the Indian monsoon region.

Note that in the annual and seasonal mean patterns there little or no differences over land in most seasons, however, two exceptions are observed in Figure 7.5. A positive and significant response over land is observed in southern Mexico and Central America in all three simulations. Another positive and significant response is observed over the Indian monsoon region, although this signal is only present in UKESM-pi.

The simulated and observed precipitation responses in the Central Pacific resemble an El Niño pattern, especially during DJF. In observations, this pattern is likely a result of the increased frequency of El Niño events for QBOW than in QBO-E (Liess and Geller, 2012). For this reason, similar differences are obtained for SSTs (Figure 7.6) which show that the QBO W-E SST appear as an El Niño pattern characterized by increased SSTs

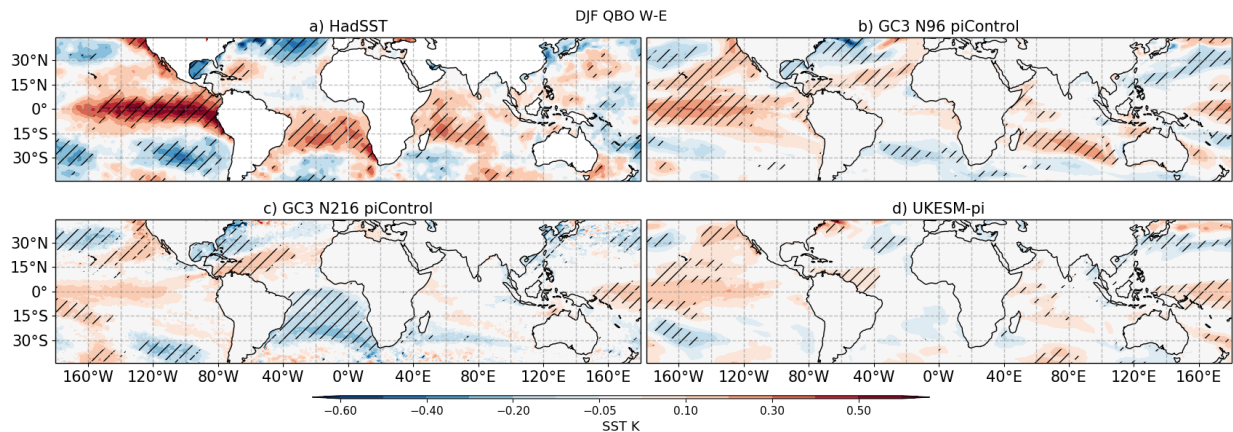


Figure 7.7: As in Figure 7.6 but for DJF.

over the Central and Eastern Pacific, extending to the equatorial Atlantic. Although these differences are much weaker than the signal for a typical El Niño event, these differences are significant in all the simulations.

The specific SST pattern for DJF confirms that the SST pattern seen in the annual mean difference is stronger during the boreal winter season, particularly for GC3 N96-pi and for the HadSST data. The significant responses in GC3 N96-pi over the North Atlantic and in the Indian Ocean also agree very well with HadSST. Results in GC3 N216-pi and UKESM-pi also show a positive SST difference over the Central Pacific during DJF although not significant. In the case of GC3 N216-pi the strongest SST anomalies over the Central Pacific appear during MAM (not shown) whereas for UKESM-pi the pattern appears during La Niña events with little-to-no response during other phases of ENSO (not shown).

In summary, this section presented the seasonal mean response in precipitation to the phases of the QBO. The main responses in the models were the ITCZ shifts over the Pacific and Atlantic Oceans, but robust signals also suggest wetter conditions in the Indian Ocean and the Caribbean Sea during QBOW compared to QBOE. The results in this section suggest a strong variation of the response with the seasons and with ENSO phase and little overall effect over land regions. For this reason, the following two sections more closely examine the effect of the QBO over the ITCZs in the East Pacific and Atlantic ITCZs, the Indian Ocean Dipole (IOD) and land-averaged precipitation over monsoon regions.

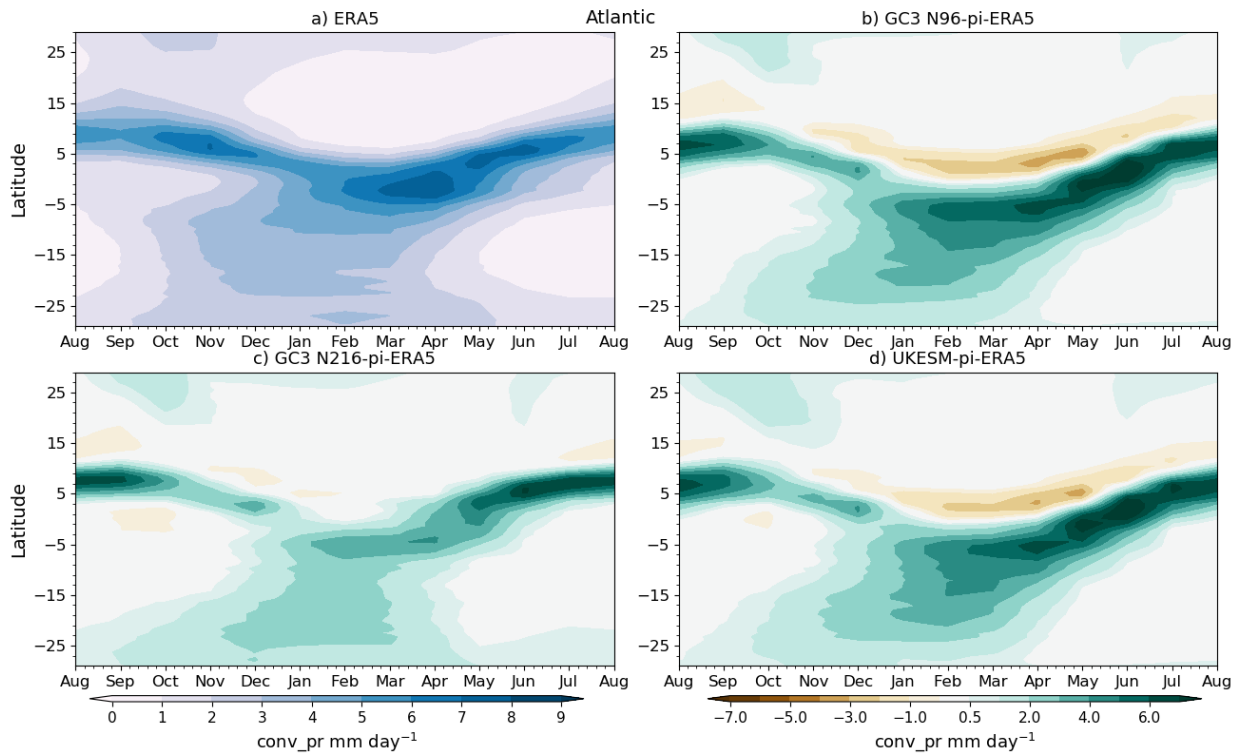


Figure 7.8: (a) Monthly and zonal-mean convective precipitation in ERA5 in the Atlantic sector [60°W-20°W]. (b-d) Biases in GC3 N96-pi, GC3 N216-pi and UKESM-pi.

7.3.2 Impacts over the ITCZ and the monsoons

This section examines more closely changes to the ITCZ position and strength associated with the phase of the QBO, specifically over the Central Pacific and Atlantic sectors. Note that the biases in the representation of the ITCZ in these models (characterized in Chapter 4) are considerable and could mean that the simulated interaction between the QBO and the ITCZ are different in the model than in the real-world. For example, Figure 7.8 shows the seasonal march of convective precipitation in the Atlantic sector in ERA5 and the biases in the three simulations with respect to ERA5. The Atlantic ITCZ in these simulations is not well represented, as shown in previous sections, as the models show a southward bias particularly in DJF and overestimates the maximum precipitation rate at the ITCZ location. In the Central Pacific sector (not shown), the models do not show a bias in the position of the ITCZ but rather a bias in the magnitude of convective precipitation, as all the models overestimate the amount of convective precipitation throughout all the seasons.

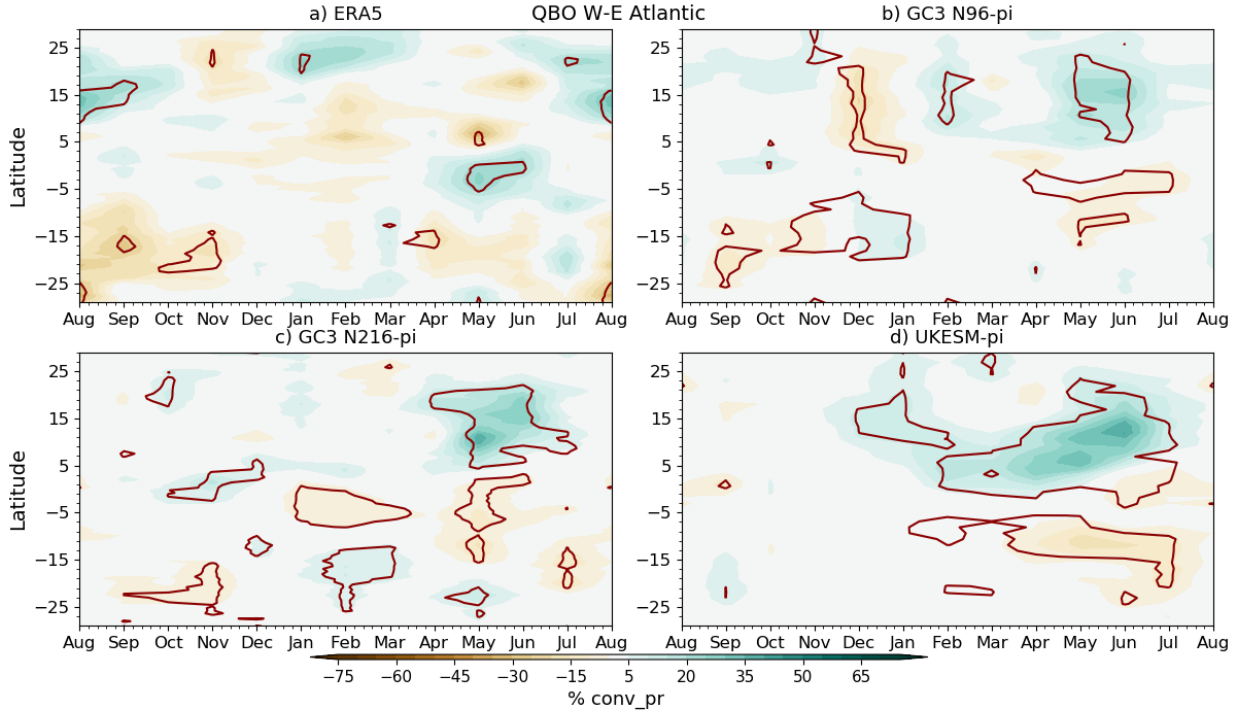


Figure 7.9: Zonal mean QBO W-E differences in convective precipitation rates in the Atlantic sector per month, shown as percent (%) where the difference is weighted by the climatological value at each latitude and month. The line-contour (red) depict differences that are statistically significant to the 95% level according to a bootstrapping test.

Figures 7.9 and 7.10 show the time-latitude difference in convective precipitation to the phase of the QBO in the Atlantic and Pacific sectors, respectively. The northward shift of the ITCZ during QBOW in the Atlantic sector highlighted in previous sections is confirmed in Figure 7.9. In all the simulations, but specially in UKESM-pi, there are two significant responses observed from March to July, one wet anomaly north of 5°N and a corresponding dry anomaly south of 5°S. The southern negative difference is weaker (-20%) than the positive response north (+40%). The response in ERA5 shows a relatively less robust response, with few significant patterns.

The southward shift of the ITCZ in the Central Pacific, reported in previous observational studies (Gray et al., 2018), is confirmed by Figure 7.10 which shows that in ERA5 a southward shift of the Central Pacific ITCZ is observed in DJF. The simulations agree well with this southward shift, particularly GC3 N96-pi during DJF. However, the southward shift response of the Central Pacific ITCZ is also observed in other seasons, for example, from May to

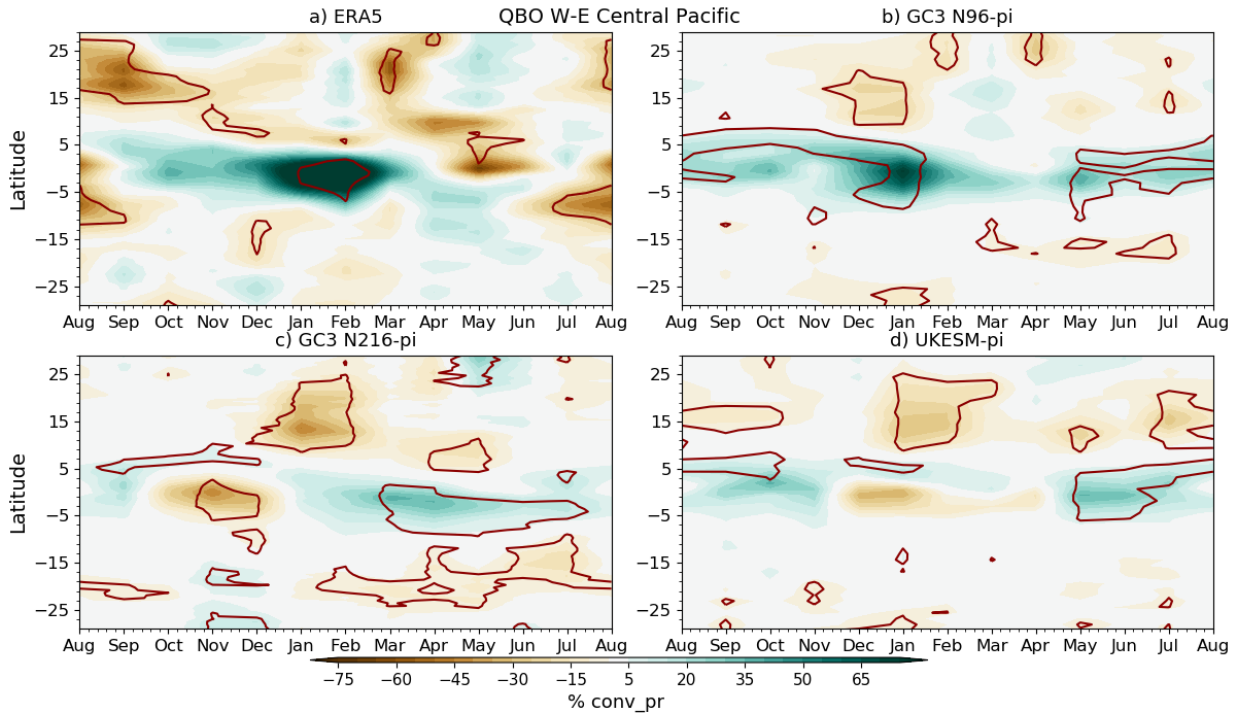


Figure 7.10: As in Figure 7.9 but for the Central Pacific sector [180°W-140°W].

September in UKESM-pi and GC3 N96-pi, whereas in GC3 N216-pi the southward shift response is seen from February to July.

These results suggest that the response to the phase of the QBO may depend on the climatological representation of the ITCZ position and strength. Nevertheless, these three simulations which exhibit slightly different representations of the ITCZ as well as of the QBO, agree on the southward shift of the Pacific ITCZ and the northward shift of the Atlantic ITCZ as the main difference between the phases of the QBO.

In spite of the multiple lines of evidence that suggest a modulation of the QBO over convective activity in land monsoon regions, the results in the previous section show little-to-no effect of the QBO on precipitation over land in these simulations. In order to investigate the precipitation response over land more closely, the global monsoon regions are defined within each simulation. A monsoon region is defined as where over 55% of the total annual rainfall is observed or simulated in the respective summer season and the summer-winter rainfall rate difference is higher than 2 mm day^{-1} (Wang and Ding, 2008; Wang et al., 2017, 2021).

The local summer convective precipitation differences between QBO phases in monsoon

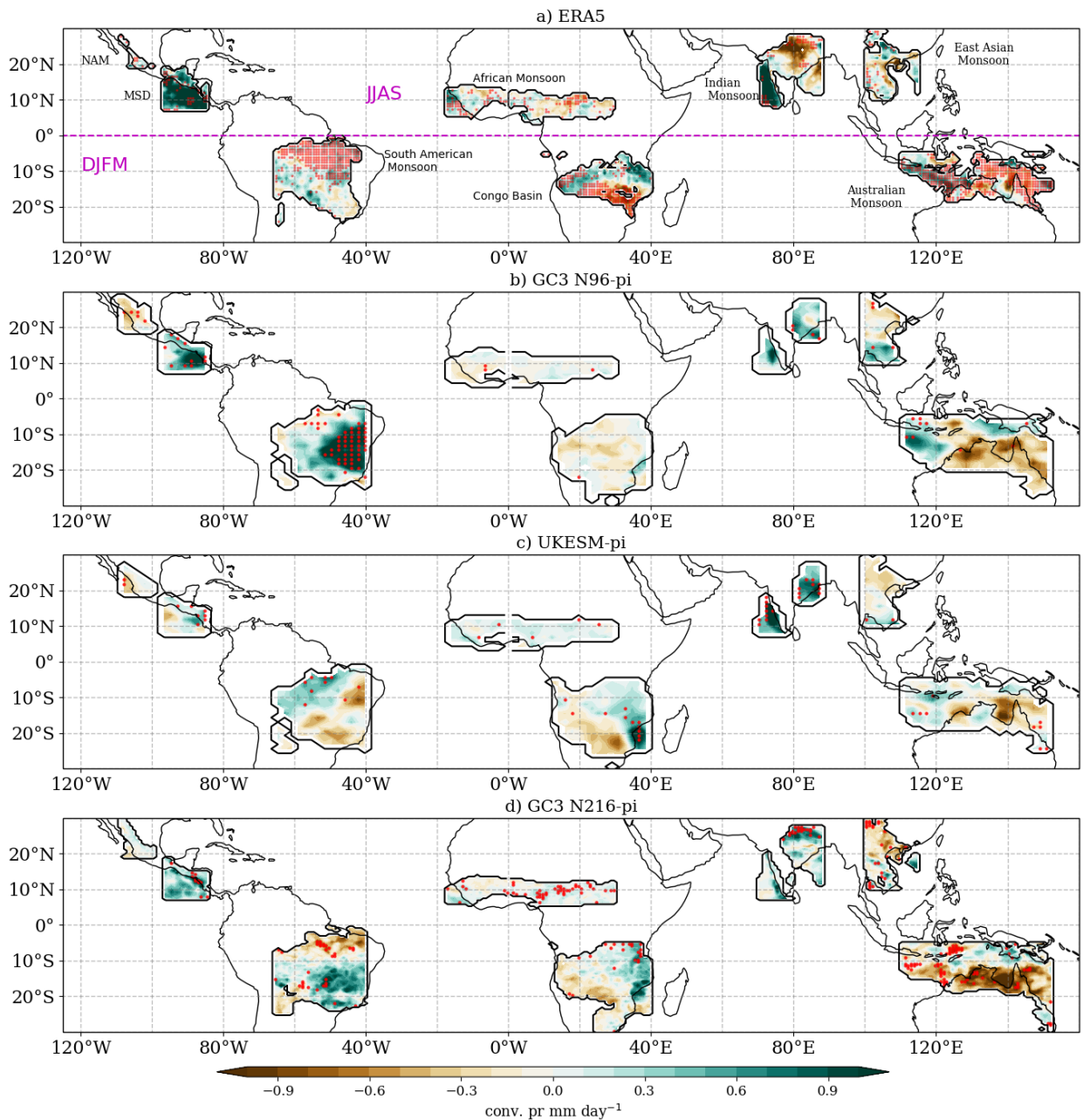


Figure 7.11: Convective precipitation differences in monsoon regions between QBO W-E phases during Neutral ENSO months for a) ERA5, b) GC3 N96-pi, c) UKESM-pi and d) GC3 N216-pi. For monsoon regions in the Northern hemisphere, differences are shown for the JJAS period, whereas for Southern Hemisphere monsoons, results are shown for DJFM. Red dots indicate differences that are statistically significant to the 95% level according to the bootstrapping test.

regions (Figure 7.11) shows that there is no region where a clear, robust and region-wide effect is observed, even when the influence of ENSO is removed by considering months where ENSO was in a neutral state. Monsoon regions like the Congo Basin, the East Asian and

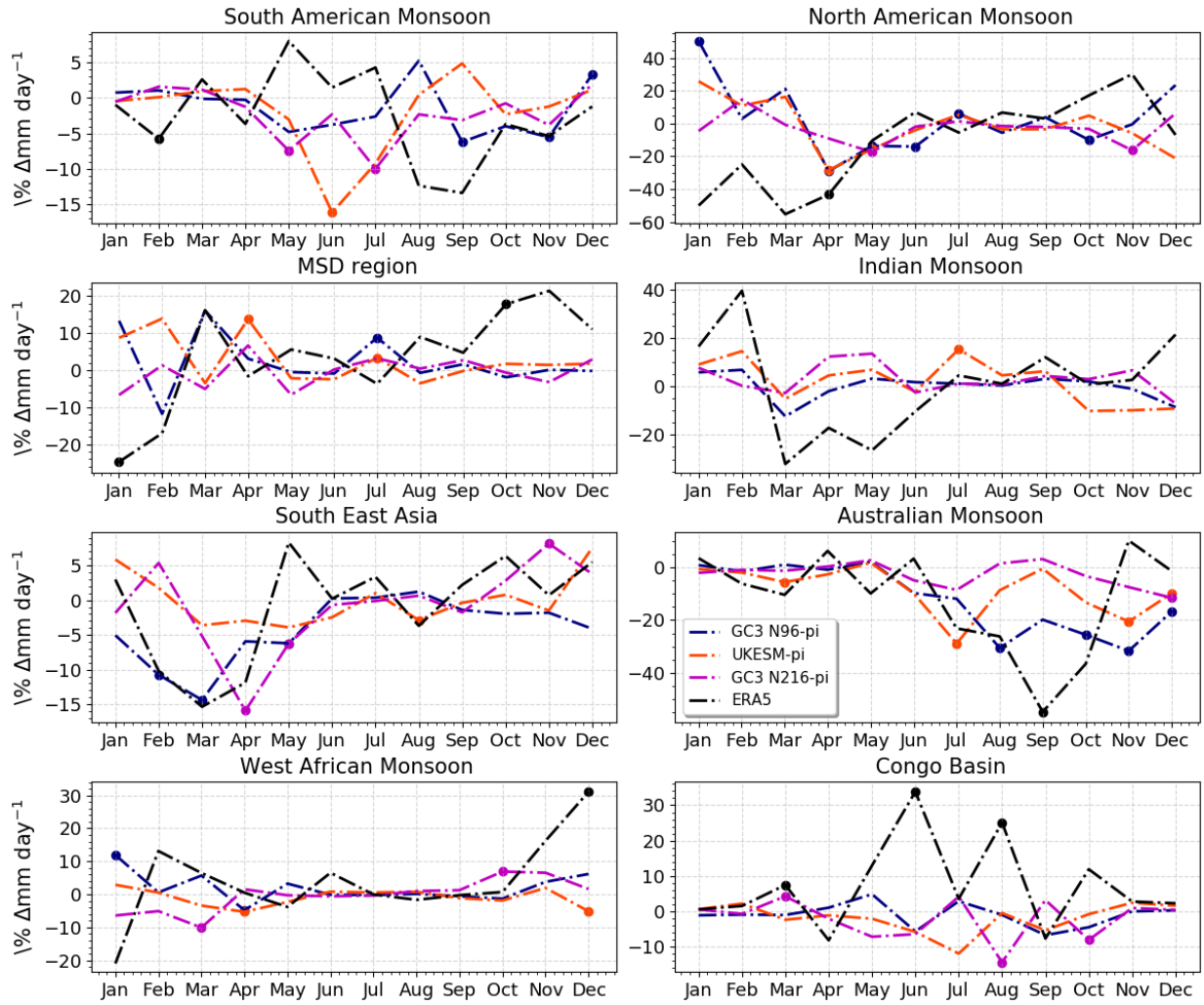


Figure 7.12: QBO W-E difference in convective precipitation in monsoon regions separated per calendar month. Dots overlaying lines indicate differences that are statistically significant to the 95% level according to the bootstrapping test.

Australian monsoons show both positive and negative responses within the domain of their regions, suggesting a rather heterogeneous response, and perhaps suggest that the QBO effect over a monsoon region is also modulated by the dynamics of the regional monsoon.

However, some features appear to be robust, as some differences are significant in all three simulations. For example, a positive response is observed in the MSD and northern Indian monsoon regions and a dry anomaly is seen over the Australian monsoon, although the latter is only widely significant in GC3 N216-pi. In the South American monsoon region, a dipole of wet and dry anomalies are observed in UKESM-pi and GC3 N216-pi, but these two simulations show an opposite pattern. The impacts over the southeastern coast of Brazil

in all the three simulations may suggest an effect over the South Atlantic Convergence Zone, which may further modify the dynamics of the monsoon. The implication of these results is that feedbacks with the dynamics of the monsoons may be more important than the effects of the QBO over the mass flux and convective activity at the grid-point scale.

To understand the temporal variability of these effects, Figure 7.12 shows the difference in area-averaged convective precipitation between QBO phases for monsoon regions for each calendar month. There is no clear signal of the QBO over any monsoon region for a large part of the year. For example, all three simulations agree in a negative QBO W-E difference in the Australian monsoon region for November and December, and this response is significant; however, the response in Jan-Mar is weak and not significant. This means that the effect of the QBO over the Australian monsoon region is found only in the early local summer season.

Similarly, over the Mesoamerican MSD region, all three simulations agree on a wet anomaly during the local summer, but this response is constrained to the month of July (the drier period of the rainy season) and is only significant in two out of the three simulations. In the Indian Monsoon region, UKESM-pi shows a significant wet anomaly, in agreement with the seasonal mean results found in the previous section, however, the other models show a weak and not significant difference. Significant relationships are found for other monsoon regions in specific months but no consistent relationship is found in any monsoon region across all three models, which agrees with the lack of robust seasonal-mean patterns presented in the previous section.

7.3.3 ENSO, the IOD and the Walker circulation

The previous section showed that the strongest precipitation responses to the QBO phase in the tropics are found in the Pacific and Indian Oceans, regions that are connected through the overturning Walker circulation and ENSO teleconnections (Cai et al., 2019). For that reason, this section investigates whether the Indian Ocean state and the frequency of ENSO events varies between QBO phases, as well as whether the mean state or variability of the Walker circulation is impacted by effects related to the QBO.

The Indian Ocean Dipole (IOD) is a coupled ocean-atmosphere feature of the tropical Indian Ocean characterized by a zonal gradient of SSTs that peaks in boreal fall (Saji

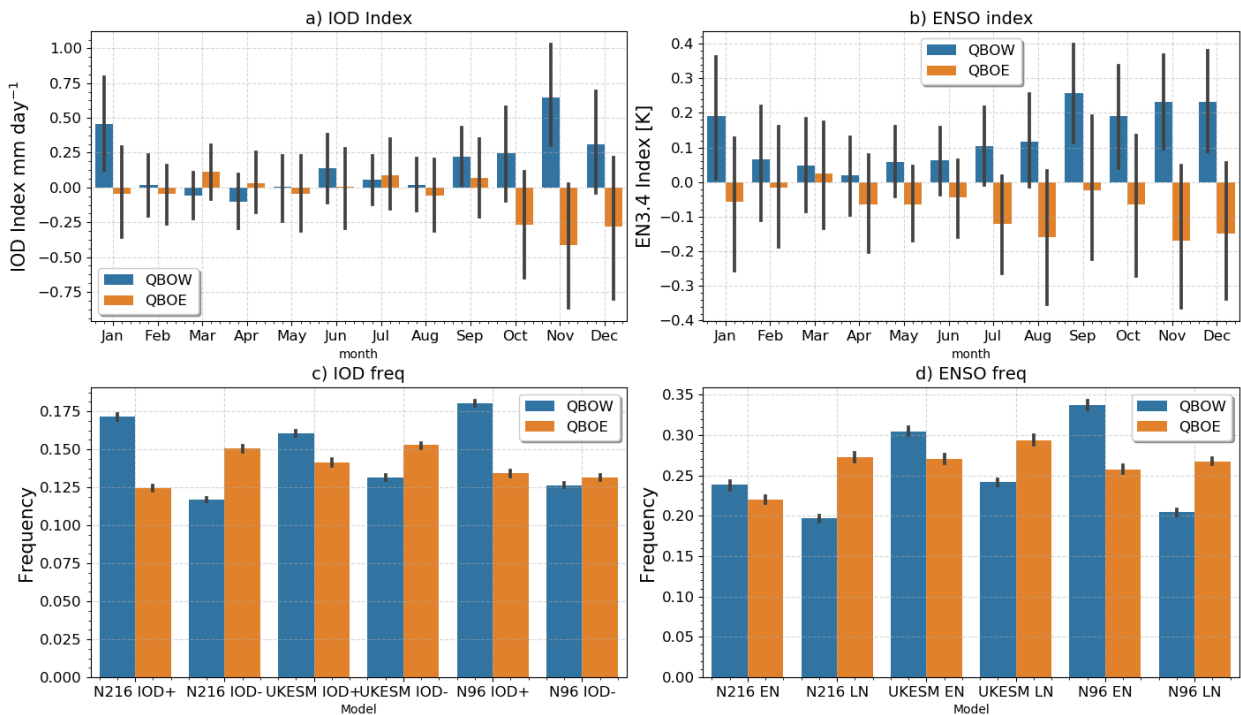


Figure 7.13: Monthly-mean (a) IOD-prc and (b) EN3.4 index separated per QBO phase in GC3 N96-pi. (c,d) Bar plots of the frequency of event occurrence for each model for (c) El Niño (EN) and La Niña (LN) and for (d) positive and negative IOD events based on the convective precipitation index. In c,d the count of events in each QBO phase is normalized per total months in each QBO phase so there is no effect associated with an uneven frequency of QBOW versus QBOE events. The error bar show the 95% confidence interval using a distribution obtained using bootstrapping test where 36 year periods were sampled from the entire run period 10,000 times and N216 and N96 labels refer to GC3 N216-pi and GC3 N96-pi, respectively.

et al., 1999; Wang and Wang, 2014; McKenna et al., 2020). IOD events are affected by ENSO events but IOD changes can also have independent long-distance effects through the Walker circulation (Wang and Wang, 2014). The previous section showed a zonal gradient in the precipitation response to the QBO during boreal fall (SON) in the three simulations (Fig. 7.4). However, in these models there was no significant SST response during this to the canonical IOD definition.

The computation of the standard IOD index, a measure of the SST gradient between the western tropical Indian Ocean and the Java-Sumatra region, results in little-to-no correlation with the QBO phase and IOD events defined using this index showed the same frequency under QBOW than during QBOE (not shown). Alternatively, a convective precipitation index of the zonal gradient in the Indian Ocean (convective IOD Index), can

be defined as the difference of the deseasonalized area-averaged convective precipitation between the western [50-70°E] and eastern [80-100°E] equatorial [10°S-10°N]. Using this convective precipitation index, IOD events are defined as in previous studies using a 1 standard deviation to define positive and negative events.

The relationship between the mean ENSO and convective IOD indices, as well as the frequency of ENSO and IOD events, and the phase of the QBO is then investigated, see Figure 7.13. The mean IOD Index and the EN3.4 SST index in GC3 N96-pi are significantly different depending on the QBO phase in GC3 N96-pi. In particular, the mean IOD Index is positive in QBOW and negative in QBOE months from September until January. The EN3.4 index also shows a non-zero mean when separated by QBO phase, with positive mean values found during QBOW and negative values during QBOE. The GC3 N216-pi and UKESM-pi results are very similar (not shown) and the differences are also significant; the only notable difference is the month in which the strongest response in each model is observed for each index.

The frequency of El Niño (EN) and La Niña (LN) months is robustly linked to the QBO phase in the three simulations (Fig. 7.13c). EN months are more frequent during QBOW phases than during QBOE phases, and in contrast, more LN events are diagnosed during QBOE than during QBOW. Similarly, the number of IOD+ events is increased in the westerly phase of the QBO, whereas negative event frequency is increased during QBOE (Fig. 7.13d) for all the three models. The confidence interval in Fig. 7.13c-d is provided by a bootstrapping test sampling the simulations into 36 yr samples and suggest that this result is robust to internal variability within the model.

In addition, several tests were done to evaluate whether changes in the frequency of IOD events were associated with known connections between the IOD and ENSO. Results show that the changes to the frequency of IOD events remain unchanged when only Neutral ENSO months are considered so there is no aliasing with the influence of ENSO on the IOD. Similarly, these changes in the frequency of IOD events are seen in the three simulations in each month from September to January, so there is no aliasing of the seasonality of the QBO within the model and the seasonality of IOD events. Note that these results do no provide any evidence of cause and effect between the QBO and IOD and ENSO indices and only evaluate the nature of these relationships within the model.

The previous results showed that there is an uneven frequency of ENSO events in the different QBO phases and that within these experiments, the QBO impacts may depend on the phase of ENSO. Linear-regression analysis was used by Gray et al. (2018) to investigate the spatial and temporal variability of the surface impacts of the QBO in tropical precipitation using a multivariate-regression model that accounts for the relationship between ENSO and precipitation. For these reasons, simple and multivariate regression analysis has been performed using the EN3.4 SST index, the 70 hPa zonal wind QBO index and deseasonalized convective precipitation. Other indices such as solar, volcanic and greenhouse forcings are omitted in this analysis because in these runs external forcings are constant.

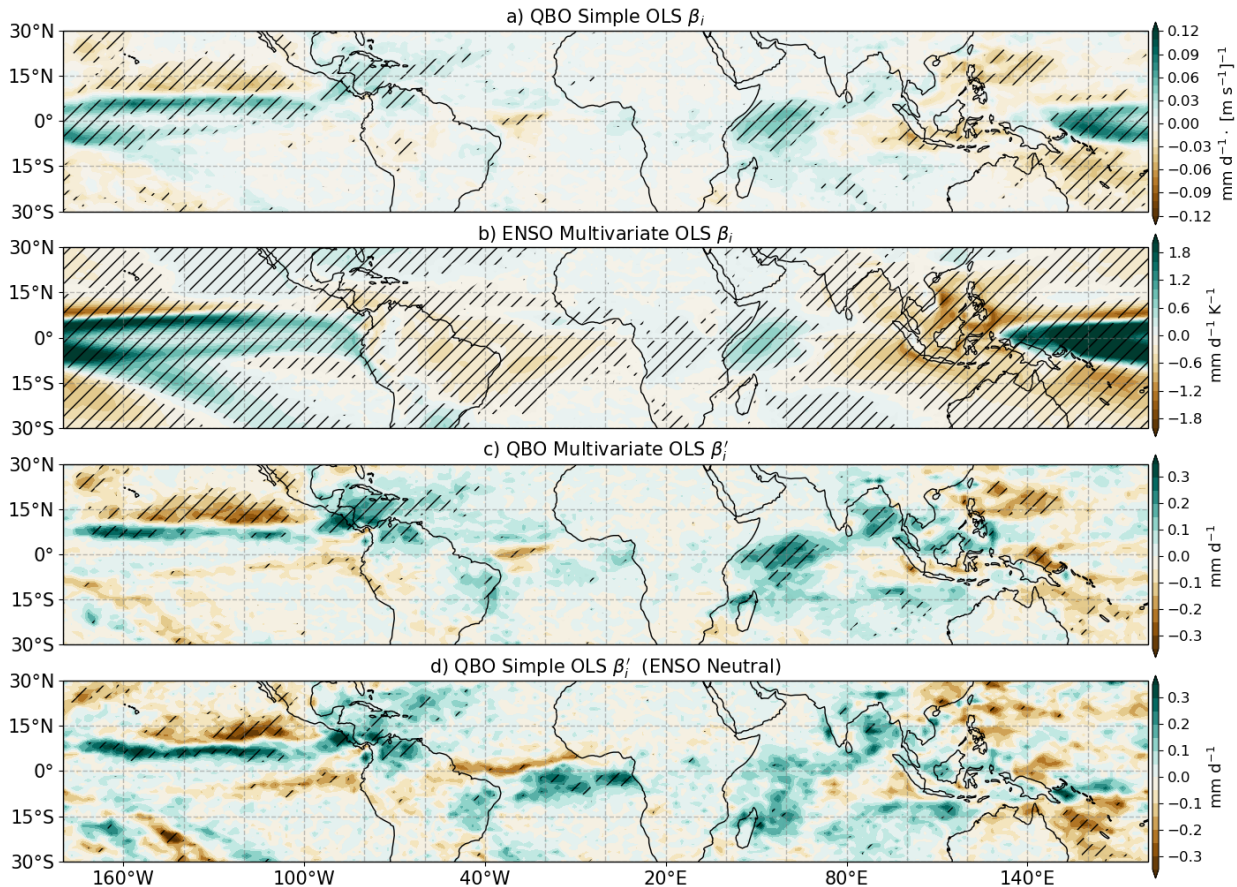


Figure 7.14: Regression model results in GC3 N96-pi. (a) Regression coefficients (β_i) from a simple ordinary least-squares (OLS) regression model with the QBO index, (b, c) the regression coefficients resulting from a multivariate regression model using the ENSO and QBO indices for the (b) ENSO and (c) QBO predictors. In (c) the regression coefficients are rescaled by multiplying the regression coefficients with the ratio of maximum amplitude and standard deviation of the QBO index. (d) Rescaled regression coefficients from a simple OLS model with the QBO index, but using time-series where ENSO was classified as in a Neutral state using the EN3.4 index.

Figure 7.14 shows results from the regression analysis of GC3 N96-pi. A simple regression model using the QBO 70 hPa index (Fig. 7.14a) shows very similar results to the composite mean differences described in the previous section. The results from the multivariate regression model implemented using the QBO and ENSO indices, show that the spatial distribution of significant regression coefficients for the EN3.4 time-series (Fig. 7.14b) is somewhat similar to results for the QBO in the simple regression model, suggesting the possibility of aliasing between ENSO and QBO indices.

The rescaled regression coefficients for the QBO, obtained using the multivariate regression model (Fig. 7.14c), i.e., the model where the influence of ENSO has been regressed-out, are broadly similar to the simple OLS model, except in the equatorial west Pacific. These regression coefficients suggest that the precipitation response of the QBO is a southward shift of the East Pacific ITCZ, as well as a wetter Caribbean Sea and western Indian Ocean for QBOW phases. A simple regression model using the QBO index during Neutral ENSO months (Figure 7.14d) shows very similar results, except in the Atlantic ITCZ region, confirming that the influence of ENSO needs to be closely examined and removed before analysing the influence of the QBO over the tropics.

The seasonal-mean results could possibly be aliasing effects of ENSO and the regression results have removed the influence of ENSO. A different question, however, is whether the QBO could modify the teleconnections of ENSO in the tropics. An analysis of the DJF

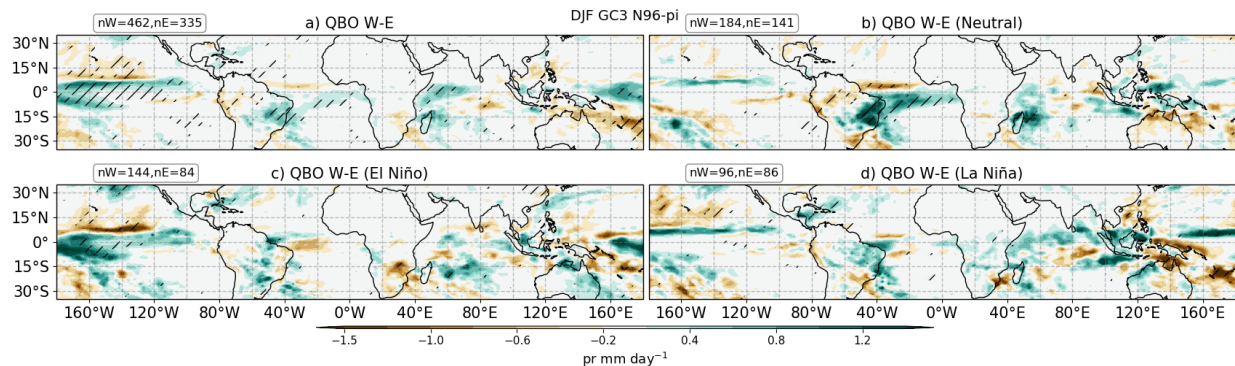


Figure 7.15: DJF QBO W-E precipitation differences in GC3 N96-pi for (a) all the events, (b) Neutral ENSO conditions only, (c) El Niño and (d) La Niña conditions. The sample size of each composite is noted in the top left corner of each panel.

mean response to phase of the QBO separated also by ENSO phase (Figure 7.15) shows that the surface response depends on both the QBO and ENSO phase.

The wet anomaly pattern in the southern equatorial (15°S - 0°) Central Pacific observed in the mean DJF response is only observed during El Niño events, not during Neutral or La Niña months. In turn, the dry anomaly in the Central Pacific at 10°N - 20°N is observed during both La Niña and El Niño seasons but not during Neutral conditions. Over the Atlantic ITCZ region and eastern Brazil, the strongest response is observed during Neutral conditions, suggesting that the pattern observed in panel a) is likely the closest to a true QBO response independent from ENSO and that this response is characterized by a southward shift of the ITCZ during QBOW.

Similar results are found other seasons (MAM and SON) and simulations, which confirms that within these simulations, the teleconnections of ENSO can be different depending on the QBO phase. One implication of these results may be that ENSO teleconnections are themselves a function of the QBO state and that the impact of the QBO may be different for La Niña than for El Niño, an effect that would be masked by the regression analysis presented above.

Results in Chapter 4 and in this chapter suggest a link between QBO, ENSO and the Walker circulation. For that reason, an analysis of the zonal streamfunction, zonal wind and vertical velocity in the deep tropics is now presented to better characterise whether the QBO has any possible influence on the mean-state and variability of the zonal overturning in the tropics. The zonal streamfunction (Yu and Zwiers, 2010; Bayr et al., 2014) is defined as:

$$\psi = 2\pi \frac{a}{g} \int_0^p u_D dp, \quad (7.4)$$

where ψ is the zonal streamfunction, u_D is the divergence part of the zonal wind, a is the Earth's radius, p is the pressure coordinate and g the gravitational constant. The streamfunction is calculated by first averaging in the equatorial band of 10°S - 10°N and integrated to the top level within the model.

Results in previous sections show that the boreal winter and early spring exhibit the strongest responses in the Pacific region and in boreal fall in the Indian Ocean. For that

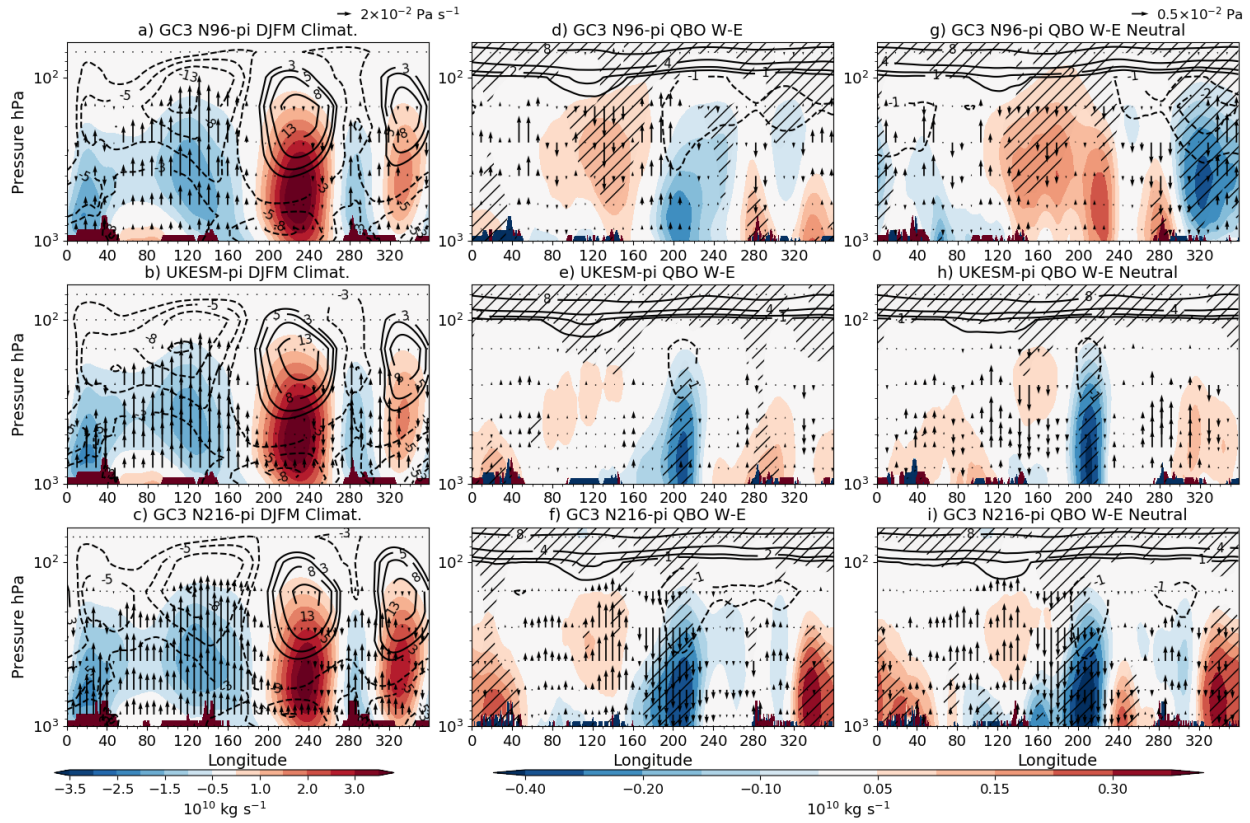


Figure 7.16: (a-c) Climatological mean-state of the Walker circulation, depicted through the zonal streamfunction (ψ) in shading, the zonal wind (contours), and vertical velocity (ω [Pa s^{-1}], vectors) during the DJFM season in the three simulations. (d-f) show W-E composite differences, during DJFM, for the same variables only that hatching represents statistical significance to the 95% confidence level for differences in the streamfunction, and only statistically significant differences in the zonal wind and ω are shown. (g-h) are as in (d-f) but considering Neutral ENSO periods only. Example vector for ω are given in the top right corners of a and g.

reason, the QBO response of the Walker circulation is illustrated for DJFM and SON in Figures 7.16 and 7.17. The streamfunction mean values are higher in DJFM than in SON, indicative of a stronger Walker circulation during boreal winter.

Composite differences in DJFM show that the streamfunction from 180-240°E is significantly weaker during QBOE than during QBOW in all three simulations. The zonal wind at upper-levels (300-100 hPa) is also weaker during QBOW at 200°E. In GC3 N216-pi, this negative ψ difference is accompanied by descending motion anomalies in the 190-220°E region, whereas anomalous ascent is observed in the Maritime continent and Indian Ocean. Vertical velocity (ω) anomalies in the other simulations are weaker in the Central-Eastern Pacific. These results suggest a weaker Walker circulation during QBOW compared to QBOE seasons.

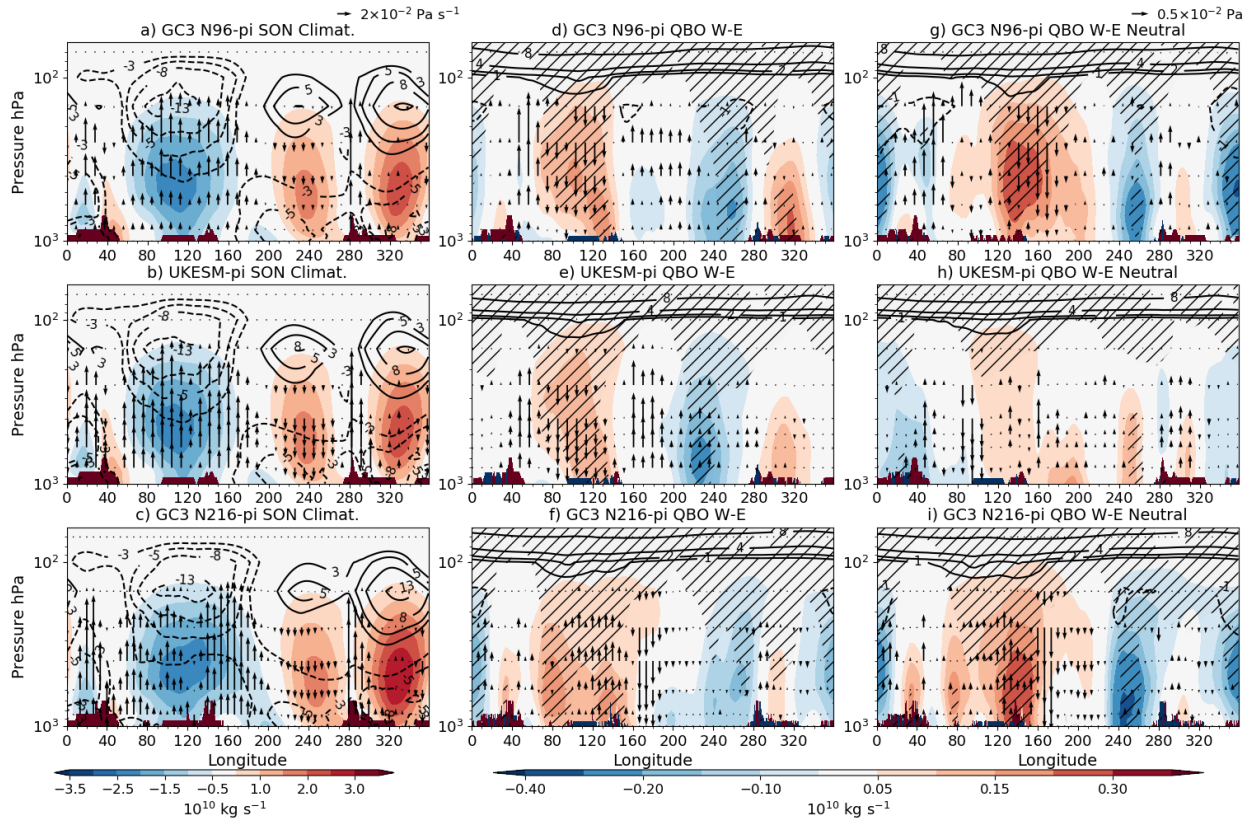


Figure 7.17: As in Figure 7.16 but for SON.

The rightmost panels in which only Neutral ENSO months are removed, suggest that this relationship between the QBO and the Walker circulation occurs regardless of ENSO events.

In boreal fall (Fig. 7.17), the mean Walker circulation is weaker and ascent is mostly concentrated in the Indian Ocean and Maritime continent, as well as in South America. Positive streamfunction differences are found to be significant over the Indian Ocean in all three simulations, associated with anomalous descent on the eastern Indian Ocean and ascent over the western Indian Ocean. These results agree well with the results using convective precipitation index for the IOD, described in the previous section, which found more rainfall in the western Indian Ocean than in the east during QBOW than during QBOE.

Furthermore, in SON, significant negative differences in the streamfunction are found in the Eastern Pacific and Atlantic Oceans and positive differences over South America, although in both cases differences in ω appear very small or not significant. These results suggest that there are possible links between ascending and descending motion in the Indian

Ocean, as described through the IOD in the previous section, and the Central and Eastern Pacific, and Atlantic Oceans through the boreal fall Walker circulation.

7.4 Summary and discussion

This chapter investigates the tropical route of QBO teleconnections in the pre-industrial control experiments of the MOHC from HadGEM3 and UKESM1. Results in this chapter confirm observational evidence (Collimore et al., 2003; Liess and Geller, 2012; Gray et al., 2018) that there is a QBO impact over tropical precipitation, mainly over the tropical ocean in the East Pacific and Atlantic ITCZs.

The position of the East Pacific and Atlantic ITCZs is significantly different between the two phases of the QBO in the three experiments; however, the season of strongest influence varies for each model. For example, the southward displacement of the East Pacific ITCZ in QBOW compared to QBOE phases (as previously reported, e.g., by Gray et al., 2018) is confirmed but in GC3 N216-pi this shift of the ITCZ is strongest in MAM whereas in GC3 N96-pi the most pronounced shift is in the DJF season. The position of the Atlantic ITCZ is found further northward during QBOW than during QBOE periods in all the simulations; the strongest response is found during late boreal spring and early summer in UKESM-pi.

For most land-monsoon regions, little evidence was found of robust impacts on the local summer monsoon precipitation associated with the QBO, in spite of observations from satellite-derived and gridded station data suggesting otherwise (Collimore et al., 2003; Liess and Geller, 2012; Gray et al., 2018; Lee et al., 2019). For example, the South American monsoon region exhibited different responses in eastern Brazil than in the southernmost part of the monsoon. The surface response over land also varied notably from model to model. One hypothesis for the lack of a spatially coherent signal over land is the differences in the representation of the monsoon dynamics and feedbacks between the three models UKESM-pi, GC3 N96-pi, GC3 N216-pi that may represent the land-surface processes and moisture transport differently, so that any grid-scale impact of the QBO on the convective profile may produce different dynamic responses in the lower troposphere.

The influence of the QBO over the Indian and Pacific Oceans was confirmed through multi-variate regression analysis, suggesting an independent effect of the QBO from ENSO in these ocean basins. However, the QBO-related differences over the Atlantic and East Pacific ITCZ appear to also depend on the phase of ENSO, suggesting a non-linear interaction between the ITCZs, ENSO and the QBO which may be confounded when using regression analysis. The observed relationship between the QBO and ENSO is confirmed in this chapter in the CMIP6 experiments, as more frequently El Niño events appear during QBOW than during QBOE and the opposite for La Niña.

A zonal gradient of convective precipitation in the Indian Ocean appeared in all the simulations, and this signal maximised during SON. This zonal gradient was further diagnosed through an index that was found to be significantly sensitive to the QBO phase, the index was found to be positive during QBOW and negative during QBOE, indicative of wetter conditions in the western Indian Ocean than in the eastern Indian Ocean during QBOW and the opposite during QBOE. To our knowledge, these results are the first suggestions of a surface impact of the QBO associated with the IOD during SON.

The zonal asymmetry in the QBO surface impacts in the tropics documented in observations (Collimore et al., 2003; Liess and Geller, 2012; Gray et al., 2018; Lee et al., 2019) is also observed within these simulations. Regional effects that depend on the longitude suggest that there is not a clear single effect of the QBO over precipitation, in contrast to early suggestions (Gray, 1984) that in general more precipitation would be observed during one phase of the QBO. This chapter proves that the relationship between the QBO and tropical convection is not likely only relevant at the grid-box scale, but the large and regional scale dynamics in the tropics play a role such that zonal asymmetries appear when analysing these responses.

The hypothesis that the QBO may influence the mean-state of the Walker circulation suggested by previous observational studies to explain zonally asymmetric responses (e.g. Collimore et al., 2003; Liess and Geller, 2012) is confirmed as the Walker circulation varies up to 10% between QBO phases, even when the effect of ENSO events is taken into account. Specifically, the Walker circulation is found to be weaker during QBOW than during QBOE. In DJF, this anomaly of the overturning circulation in the Pacific is likely linked to the

East Pacific ITCZ shifts, and in SON, the changes to the overturning are likely linked to the ascending and descending motions in the Indian Ocean.

The relationships found between the QBO, the Walker circulation and ENSO frequency could potentially be causally linked with the QBO variability being the driving mechanism. Changes to the mean state of the Walker circulation are known to modify the frequency of El Niño events and La Niña events. A weaker state of the Walker circulation could more likely trigger an El Niño event during QBOW than during QBOE, and similarly, a stronger Walker circulation during QBOE could more likely trigger a La Niña event, which would be consistent with the results of this chapter.

The results of this chapter are one of the few analyses of the tropical route of QBO teleconnections within a fully coupled GCM. The length of the pre-industrial control experiments (500 yr) was useful to adequately evaluate the statistical significance of the relationships between the QBO and tropical climate features. Furthermore, the fact that most of the impacts diagnosed in this chapter are very similar in the three simulations, despite their differences in resolution and inclusion of Earth System processes provides robustness to the results. Nevertheless, the dynamical core of all the simulations is the same, so the parametrisation schemes such as the convective and gravity-wave scheme are identical. Further work needs to evaluate these relationships in different models from CMIP6.

However, the direction of causality cannot be interpreted from the regression or composite analyses presented in this chapter. For example, the ENSO-QBO relationships could be explained by anomalous tropical wave activity associated with ENSO modifying the downward propagation of the QBO (Schirber, 2015) or alternatively, the QBO temperature variability affecting convection in various regions and modifying the tropical circulation. Further experiments are needed to separate the mechanisms that could explain these relationships and that could separate the directions of influence between the tropical stratosphere and troposphere.

8

QBO Teleconnections in the UM with a nudged stratosphere

The previous chapter describes tropical teleconnections associated with the stratospheric quasi-biennial oscillation (QBO) in the MOHC CMIP6 pre-industrial control experiments. One could reasonably hypothesize that those relationships are the result of a control of tropical convection by the QBO. This chapter tests this hypothesis by constraining the zonal winds in the tropical stratosphere, eliminating any possible influence of the troposphere on the stratosphere. The relaxation experiment design is described and results are presented and a discussion on how the nudging modifies the teleconnections found in the free-running CMIP6 experiments is given at the end of the chapter.

8.1 Introduction

The tropical route of QBO teleconnections remains relatively less understood than the polar and subtropical routes. The observational evidence available (e.g. Collimore et al., 2003; Liess and Geller, 2012; Schirber, 2015; Gray et al., 2018) cannot answer questions such as whether the observed relationship between tropical convection and the QBO are causally linked and if so, is the QBO the driving mechanism or is a result of convective active influencing the QBO.

The use of GCMs to address these questions is limited due to the fact that only some recent models are able to reproduce a sufficiently reasonable representation of the QBO. Still, some CMIP6 models produce highly unrealistic QBO features and some require a relaxation of the model towards an observed state of the QBO, i.e., artificially generating a QBO (Richter et al., 2020). For example, observed relationships between the QBO and the Madden-Julian Oscillation (MJO) (e.g. Son et al., 2017; Wang et al., 2019) have not been found in GCMs (Lee and Klingaman, 2018; Kim et al., 2020; Martin et al., 2021) and the leading hypothesis is due to the underestimation of models of the upper-troposphere lower-stratosphere (UTLS) temperature variability associated with the QBO.

These biases have led several studies to perform experiments in which a GCM is relaxed towards an observed or idealized state where the model is forced to reproduce an observed or idealized or a state of the stratosphere (Gray et al., 2020; Richter et al., 2020; Martin et al., 2021). The nudging technique has proven useful because the relaxation can prove causal pathways and test specific hypotheses regarding the mechanisms that play a role in stratosphere-tropospheric coupling.

This chapter first makes a case for nudging experiment, described the experimental configuration and the goals and hypotheses that we aim to test using these simulations. Then, a description of the experimental setup is given and finally, results comparing runs using the nudging technique versus the free running model are presented and discussed highlighting the possible mechanisms at play for the tropical route of QBO teleconnections.

8.2 The case for nudging

The number of GCMs with a full stratosphere have increased notably from CMIP3 to CMIP6 which means that features such as the QBO are increasingly better resolved with each iteration of the CMIP (Bushell et al., 2020; Richter et al., 2020). Nevertheless, several aspects of the QBO are still not well represented by state-of-the-art climate models, such as the period and amplitude of the QBO (Schenzinger et al., 2017; Richter et al., 2020). These biases increase uncertainty in teleconnections diagnosed from these models, because these

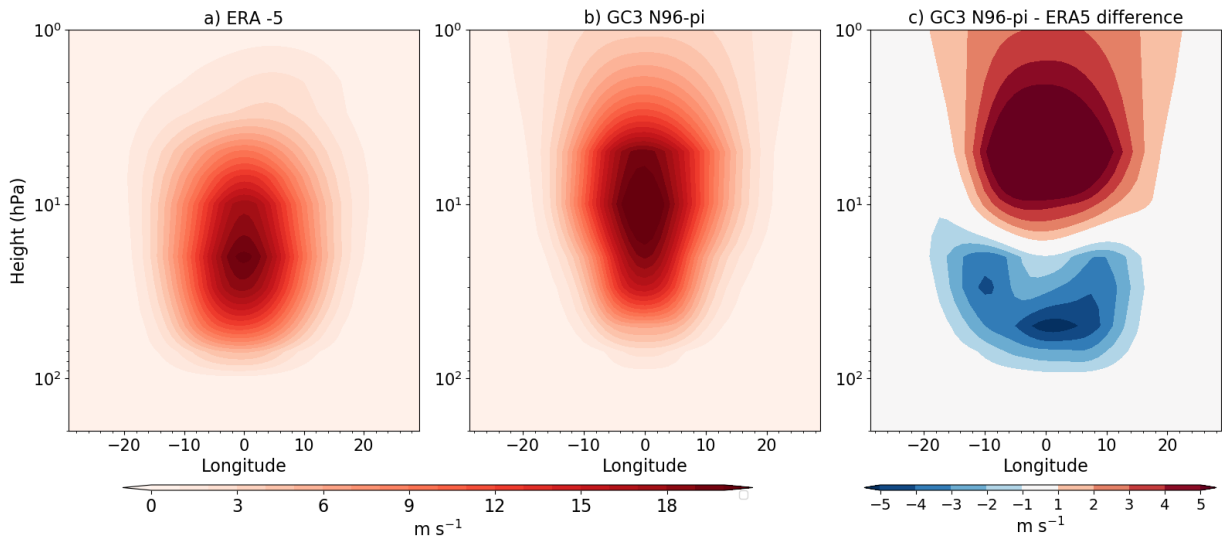


Figure 8.1: Latitude-pressure plot of the amplitude [m s^{-1}] of the QBO. Obtained from the zonal mean zonal wind fourier spectrum magnitude within the QBO periods, as in Schenzinger et al. (2017).

biases could make the models misrepresent processes that are observed in the real-world between the tropical stratosphere and troposphere.

8.2.1 The importance of biases in the UTLS for stratosphere-tropospheric coupling

One key stratospheric bias in most of the existing climate models relates to the representation of the QBO in the lowermost stratosphere. Figure 8.1 illustrates this bias in GC3 N96-pi by comparing the variation of the QBO amplitude with height and latitude with ERA5; the amplitude is obtained using the method in Schenzinger et al. (2017). The amplitude of the QBO in the lowermost equatorial stratosphere is much smaller and extends to the subtropics less in the model than in ERA5, in agreement previous studies (Schenzinger et al., 2017; Richter et al., 2020; Bushell et al., 2020). The implication of this bias is that if the QBO signal is too weak in the lower part of the stratosphere in the model, the simulated meridional circulation will also be weaker, and any temperature anomaly associated with this residual circulation will also be smaller near the tropopause.

The main hypothesis suggested in the literature to explain observed relationships between the QBO and tropical convective diagnostics is the temperature variability in the tropopause

layer and its influence on the upper-level static stability (Collimore et al., 2003; Liess and Geller, 2012; Nie and Sobel, 2015; Gray et al., 2018). Models that simulate a weaker than observed variance of the temperature near the tropopause associated with the QBO may dampen any processes that relate the QBO to tropical convection. Due to the fact that most models underestimate the variability of the temperature associated with the QBO in the UTLS region, several studies have argued in favour of performing numerical experiments with a GCM where the stratosphere is relaxed towards an observed or idealized state (e.g. Lee and Klingaman, 2018; Martin et al., 2021) to correct this bias.

Chapter 7 described a number of robust signals in convective features associated with the QBO within the CMIP6 experiments that have an internally generated QBO. Figure 8.1 shows that the signal that may be responsible for these relationships is too weak within these models. One might reasonably then expect that if the models simulate a stronger temperature variability associated with the QBO, then the surface response to the phase of the QBO would also increase. The remainder of this chapter describes the experimental design and results of simulations that aim to alleviate the biases in the QBO in the lower stratosphere and compare the surface response in these experiments with those of simulations with a free-running stratosphere with an internally generated QBO.

The following section describes a nudging protocol using the Met Office Unified Model. The aim of these experiments is to investigate how the tropical route of QBO teleconnections is modified when the representation of the QBO is improved, and whether nudging is a good tool for this purpose.

8.2.2 The nudging protocol

This section describes the experimental setup for the nudging experiments. The GC3.1 configuration of the UM model is used (model version 11.4), using an atmospheric horizontal resolution of N96 (corresponding to the low-resolution version of the simulations of the MOHC submitted to CMIP6). Both atmosphere-only and ocean-atmosphere coupled experiments were conducted, in all cases spanning the period 1981-2015, using a present-day climate setup where all forcings are set constant to those of the year 2000, so there is no variation in, e.g., greenhouse gases within these simulations.

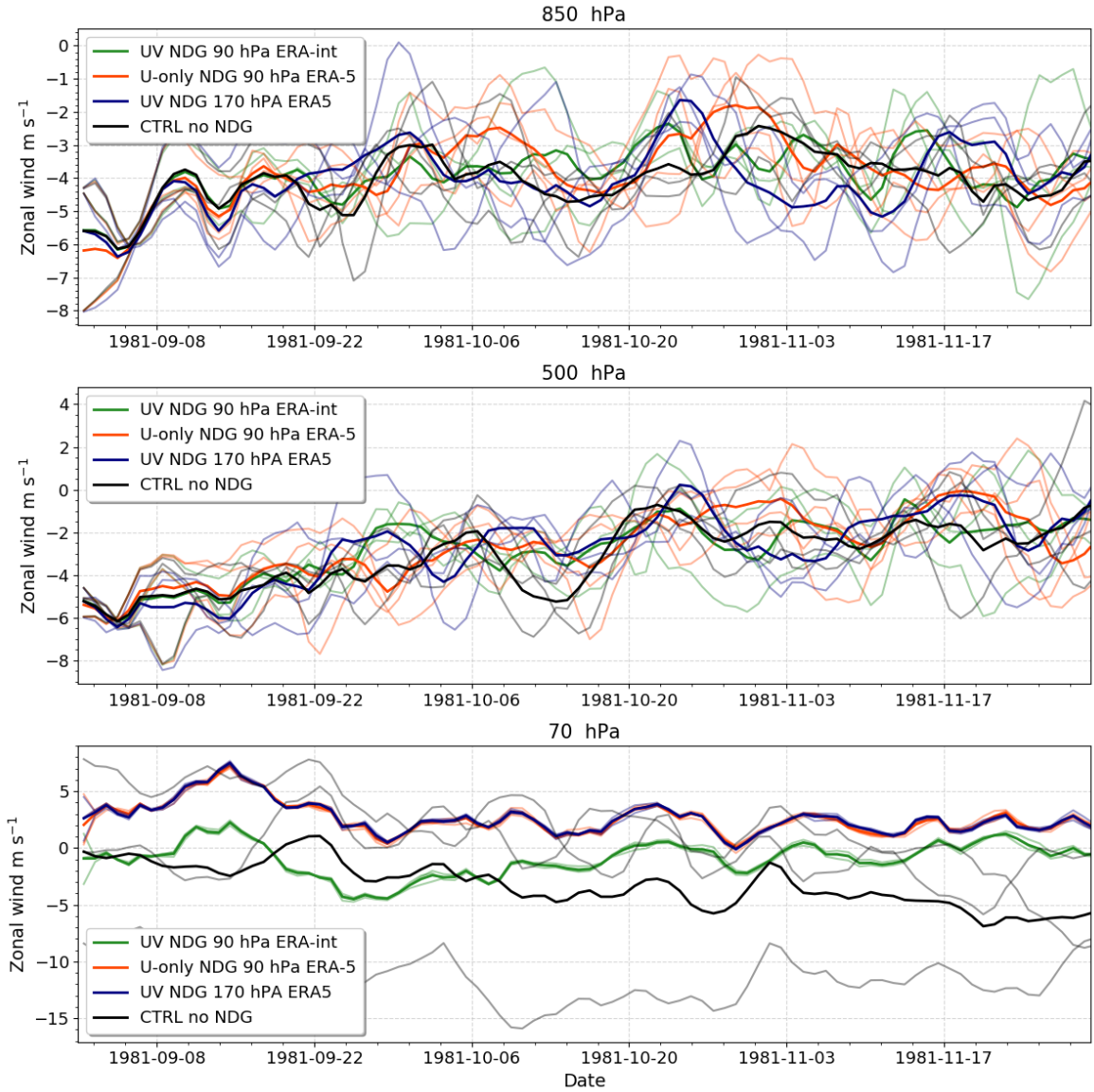


Figure 8.2: Time-series of the zonal-mean zonal wind in the 10°S - 10°N band at the 850 hPa (upper), 500 (middle) and 70 hPa (lower) levels. Results are from atmosphere-only simulations without nudging (CTRL no NDG), with nudging applied to both u and v up between 90 and 4 hPa using ERA-interim data (UV NDG 90 hPa ERA-int), with nudging between 170 hPa and 4 hPa nudging u and v using ERA5 data and finally, nudging only u from 90 to 4 hPa using ERA5 data. For each kind of the simulation, each ensemble member is shown (faint line) and the ensemble mean (solid line) is shown.

Nudging refers to the relaxation of a variable within the model to a specified state, and is a technique that has recently been used for several purposes such as investigating the MJO-QBO relationship in a climate model (Martin et al., 2021) and the role of the upper stratosphere for forecasting sudden stratospheric warming events (Gray et al., 2020).

In the UM setup, three variables can be relaxed, air temperature (T) and the zonal and meridional components of the wind (u and v). The relaxation is applied towards reanalysis data or towards an idealized state at each grid-point, in contrast to the setup in other models (e.g. Martin et al., 2021) where the relaxation is performed in a zonal-mean sense. Furthermore, the nudging can be performed between specified vertical levels and in selected latitude/longitude regions. To find the experimental setup that resulted in an improvement in the representation of the QBO without over constraining the model's climatological state we conducted several sensitivity tests using an atmosphere-only setup to test the effect of nudging all u , v and T compared to just one, as well as the model levels and latitudes where the nudging was applied.

Figure 8.2 shows the time-series of the zonal-mean zonal wind at different levels for the different sensitivity experiments performed. Three ensemble members were performed first for a control simulation with no nudging, a simulation where u and v were relaxed towards ERA-interim, and two simulations with ERA5 as the nudging data, one relaxing u between 90-4 hPa and another relaxing u and v between 170 hPa and 4 hPa.

These results show that in the troposphere (850 hPa) all the ensemble members diverge towards different states, whereas in the lower stratosphere, the ensemble members of the nudged simulations converge towards a single state. The nudged simulations at the 70 hPa level differ only due to the nudging data, highlighting the differences in the zonal wind in the equatorial stratosphere between ERA5 and ERA-interim. From this part on, results using only ERA5 nudging data are presented.

Figure 8.3 shows the vertical profiles of temperature and zonal wind in these simulations. The variability of T associated with the QBO, is fairly well represented by all the nudged simulations, compared to the control simulations, even when T was not relaxed towards ERA5. This results proves that the meridional circulation imposed by the shear imposed when relaxing u is enough to force temperature variability within the model through thermal wind balance, as found in Martin et al. (2021).

The climatological zonal mean zonal wind and the variability of associated with the QBO (Fig. 8.3d-f) is much improved in the simulations with nudging, as expected, in the stratosphere. Notably, in the simulations where nudging was applied above 90 hPa, the

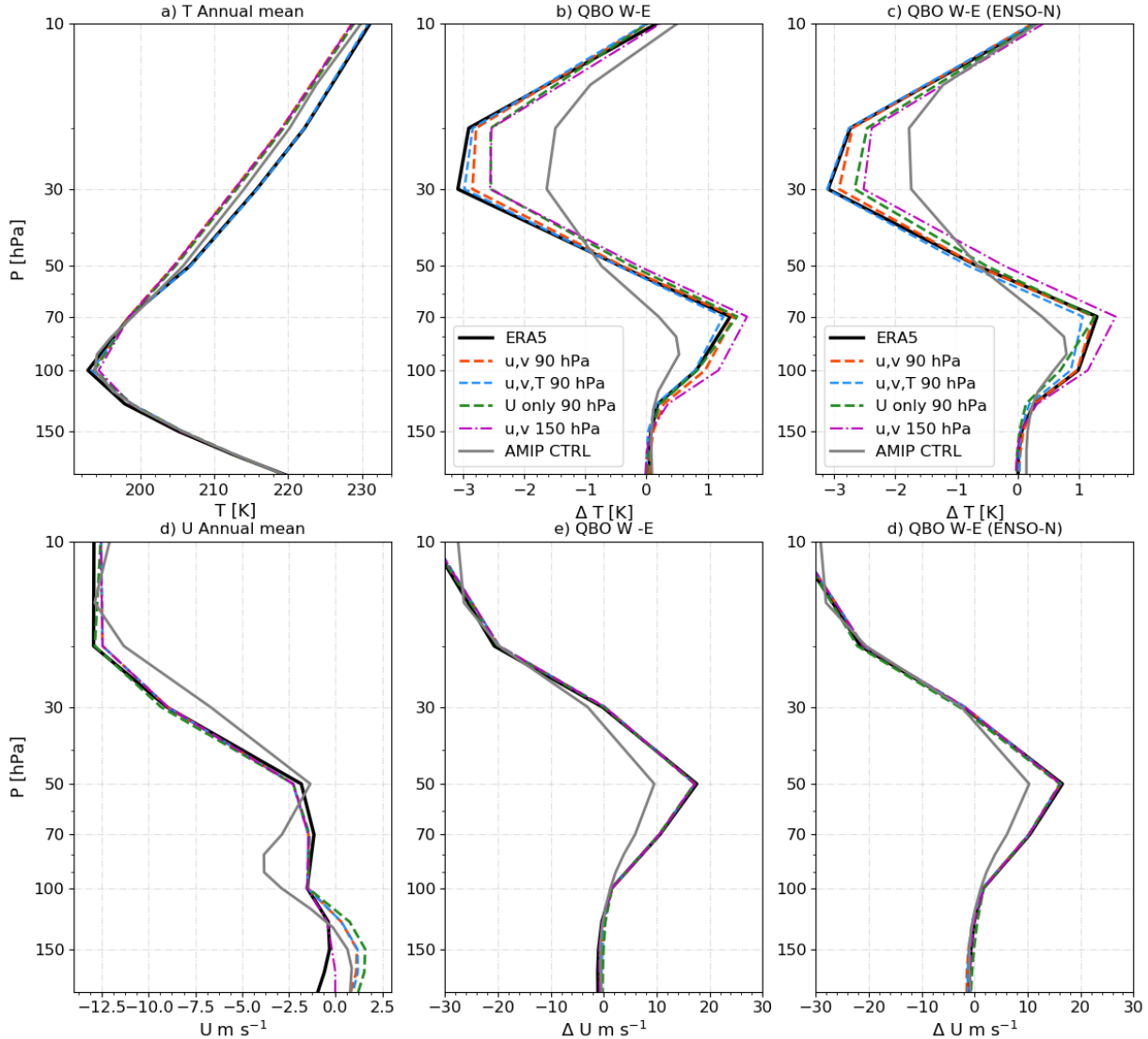


Figure 8.3: Vertical profiles of zonal mean temperature (a-c) and zonal wind (d-f) depicting the climatological state (a, d), the QBO W-E difference (b, e) and the QBO W-E difference during Neutral states of ENSO (c, f). In all the simulations with relaxation, the nudging data was ERA5.

biases lower down in the stratosphere at 150 hPa remain comparable to those of the control simulation, indicating that nudging the stratosphere does not pose a direct effect over the upper-tropospheric climatological state, in a zonal-mean sense.

The final experimental design chosen was to perform the nudging in the model levels 52-72 which roughly correspond to 90 hPa to 4 hPa, with a tapering of 4 levels, which means that full nudging was only working within levels 56-68. The nudging was done at all longitudes in the latitude band of 10°S-10°N with a latitudinal tapering of 10 degrees on

Table 8.1: Experimental setup indicating the model configuration, the period, ensemble members, acronym and relaxation details.

Setup	Period	Ensemble members	Name	Nudging
Atmosphere-only	1981-2015	3	AMIP	ERA5. U-only 90 hPa
Atmosphere-only	1981-2015	1	AMIP-Control	No
Atmosphere-only	1981-2015	3	AMIP-Shifted	ERA5. U-only, 90 hPa. Relaxation shifted -1 year.
Coupled	1981-2015	6	Coupled	ERA5. U-only 90 hPa.
Coupled	1981-2015	2	Coupled Control	No.

both sides. Only the zonal component of the wind (u) was relaxed, so that T and v were not relaxed. The experimental setup aims to reasonably simulate the observed variability of the zonal wind leaving the meridional component of the wind and the temperature to respond freely within the model.

Atmosphere-only and coupled ocean-atmosphere simulations were performed with this nudging setup, with corresponding control simulations in which there was no relaxation of any kind. The atmosphere-only, also referred to as AMIP, experiments were run with observed SSTs from the HadSST dataset. In all cases the nudging of the atmosphere was done only between 90 and 4 hPa and at equatorial latitudes only, whereas the surface boundary SSTs are used at all latitudes. For the nudged experiments several ensemble members were performed, three for the atmosphere-only configuration and six for the coupled ocean-atmosphere configuration. Each ensemble member was initialized from a different ocean/atmosphere initial condition in order to decrease the role that internal variability may have on these simulations.

In addition to the nudged and control coupled and AMIP experiments, we performed another atmosphere-only experiment. In the normal AMIP Nudged experiment, the SST driving data corresponds to the zonal wind in the equatorial stratosphere that was observed in the real-world. To explore possible feedback processes between QBO winds and the SSTs, we performed an AMIP Shifted experiment, where the nudging data was shifted with a -1 year lag from the SSTs. In this experiment, e.g., the model year 1997 was run

using 1997 SSTs but zonal winds in the stratosphere corresponding to 1996 of ERA5. In this way we have minimised any in-phase relationship between the QBO phase and the SSTs. An alternative approach would be to 'shuffle' the SSTs so that each year is run with randomly selected SSTs. However, since we are performing multi-year simulations this has associated issues of how to join the randomly-selected SSTs at the year-boundary, to form a coherent multi-year SST time-series. To avoid this issue we decided to simply shift the SSTs by one year so the QBO phase and SSTs were not aligned.

The following section presents the results of these experiments, first by reporting how the tropical tropopause variability is modified when nudging is applied and then by showing the surface impacts associated with the QBO in the nudged experiments, first in the atmosphere-only configuration and then in the coupled setup.

8.3 Results from nudging experiments

This section investigates the effect of nudging for the representation of the QBO, the variability in the upper troposphere lower stratosphere (UTLS) associated with the QBO, and ultimately, surface impacts driven by QBO effects on tropical convection. First, this section evaluates how nudging modifies the wind and temperature variability in the UTLS region compared to control and CMIP6 simulations.

8.3.1 Tropical UTLS variability

Figure 8.4 shows the zonal mean difference in zonal wind associated with the QBO phase, in a latitude-height sense, in the 500-y CMIP6 GC3 N96-pi and both the AMIP and coupled 35-year (un-nudged) control simulations. The zonal wind variability in the lower stratosphere associated with the QBO is deficient in the GC3 N96-pi and control experiments, principally near the tropopause as the signal is too narrow and weaker than in the reanalysis.

The temperature is able to respond to the nudging within the model freely, Figure 8.5 reveals that nudging the zonal wind can also improve the air temperature variability in the lower stratosphere driven by the QBO shear. The positive temperature anomaly in the equatorial region around the 100 hPa at the tropopause level is much weaker in the

GC3 N96-pi, AMIP Control and Coupled Control compared to the two nudged experiments and to ERA5. The Nudged experiments not only improve the temperature signal in the equatorial lower stratosphere but seem to overestimate this signal around the 70 hPa level.

However, observations show a horse-shoe temperature anomaly pattern in the subtropics characterised by a negative anomaly that extends from 20-40 degrees north and south, a signal that is missing in the GC3 N96-pi, AMIP Control and Coupled Control experiments but is recovered in the Nudged experiments. This means that without nudging further away than 20 degrees north or south, the subtropical signal is obtained by improving the residual circulation associated with the QBO.

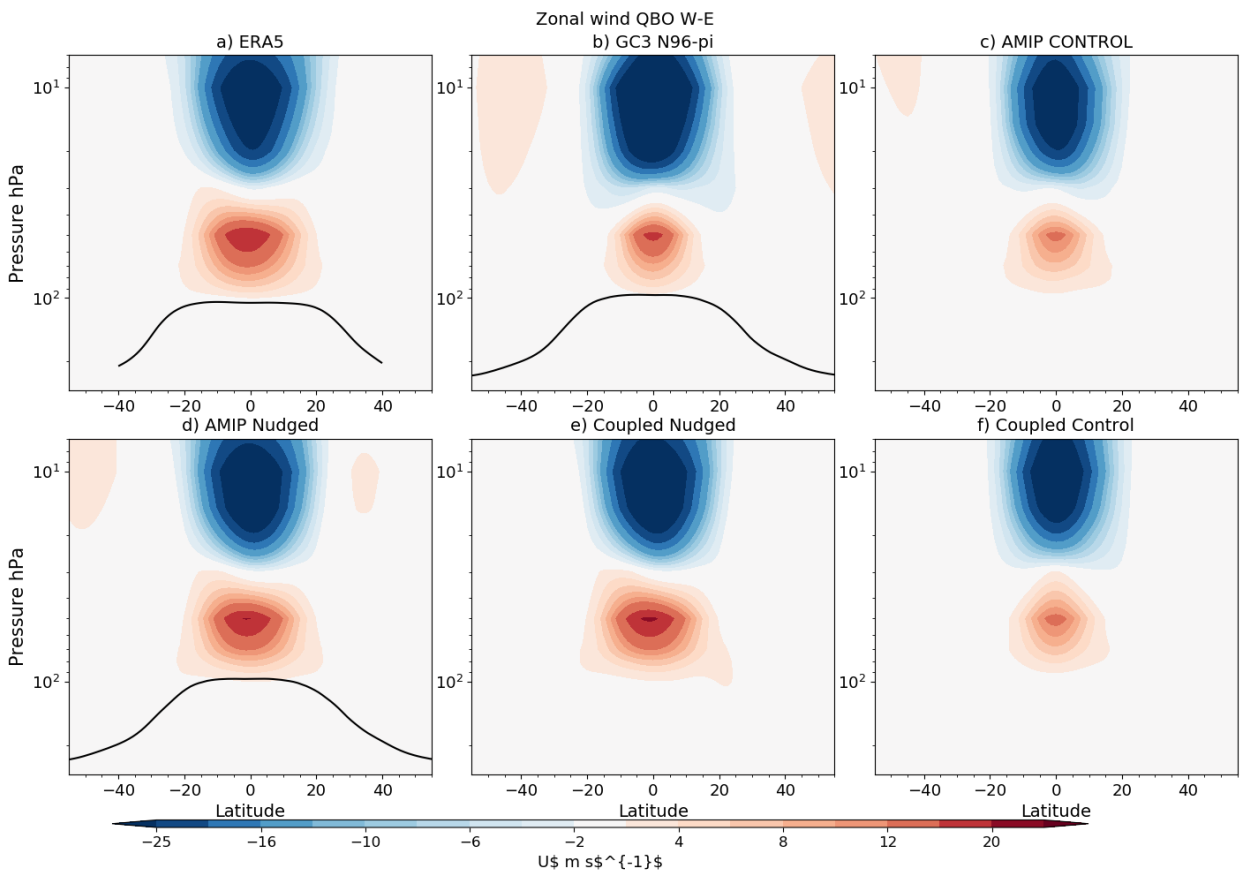


Figure 8.4: Latitude-height plot of the zonal-mean zonal wind differences (QBO W-E) in (a) ERA5, (b) GC3 N96-pi from CMIP6, the control simulations with no nudging in an (c) AMIP and (f) coupled configurations, and the nudged simulations in (d) AMIP and (e) coupled configurations. The black line denotes the tropopause height obtained from the model data in (b, d) and for ERA5 the tropopause height was found through the gradient threshold method. For the nudged experiments, the ensemble-mean is shown.

The spatial distribution of the wind and temperature variability associated with the QBO near the tropopause level (100-hPa level) is shown in Figures 8.6 and 8.7 for ERA5, GC3 N96-pi and control and nudged experiments. These Figures show, first, that the free running model (seen in GC3 N96-pi and Coupled Control) is able to reproduce the zonal asymmetries in the QBO signal (Tegtmeier et al., 2020b) at the 100 hPa level albeit much weaker than the observed signal. The wind differences, for instance, are stronger over the Maritime continent in observations whereas the temperature signal is stronger in the Maritime continent and over equatorial Africa, both features reproduced sensibly by the model without nudging.

The nudging particularly improves the temperature response to the QBO at 100 hPa where the QBO W-E difference is more than twice the amplitude of the un-nudged response. In addition, the temperature signal in the Nudged experiments is improved in AMIP Nudged and AMIP Shifted experiments, indicating that these differences are not associated

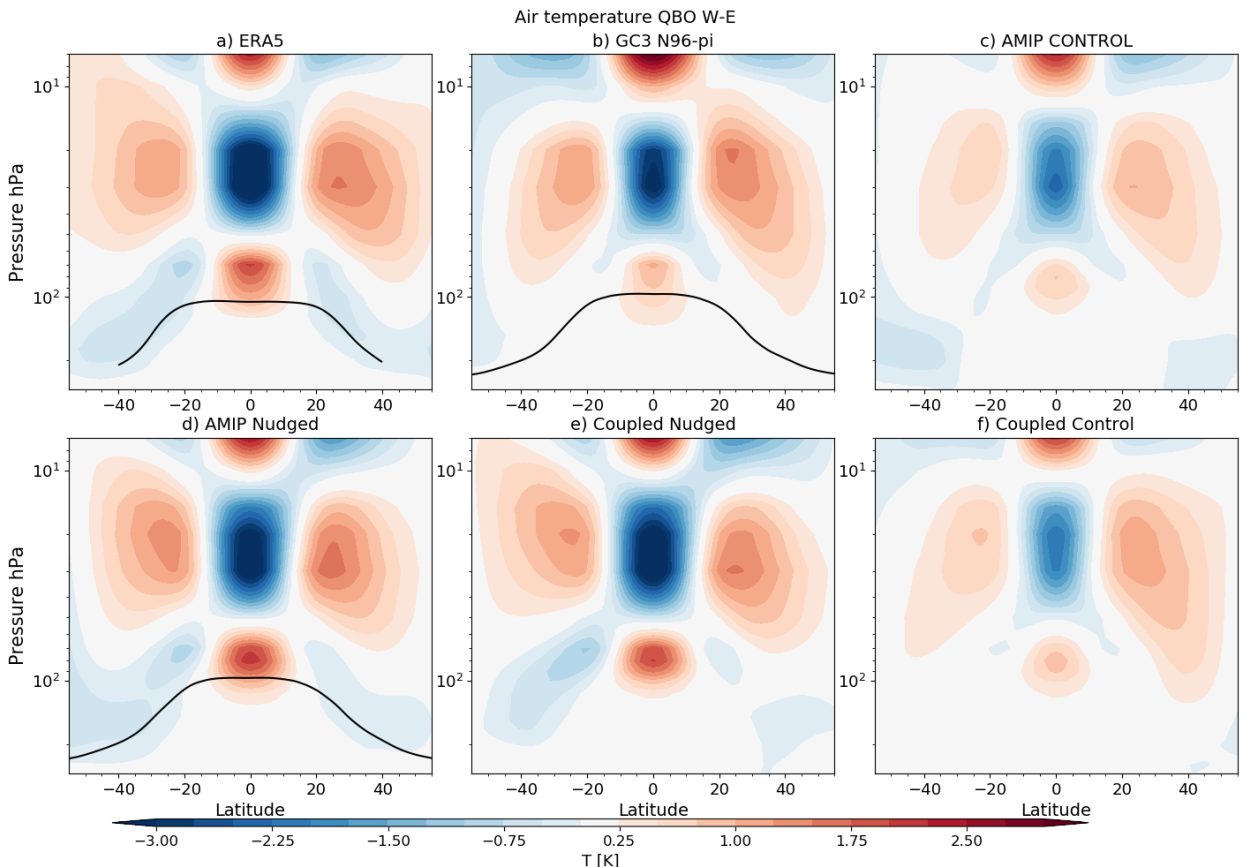


Figure 8.5: As in Figure 8.4 but for air temperature.

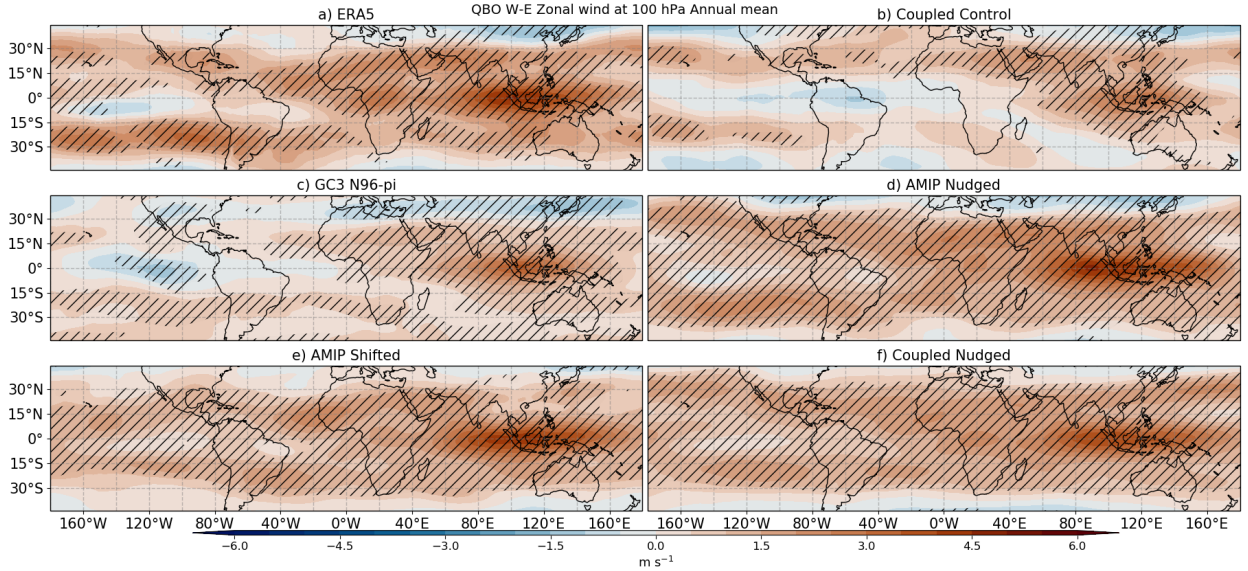


Figure 8.6: Zonal wind difference in QBO W-E at the 100 hPa level. Hatching denotes significance to the 95% level according to a Student's t-test.

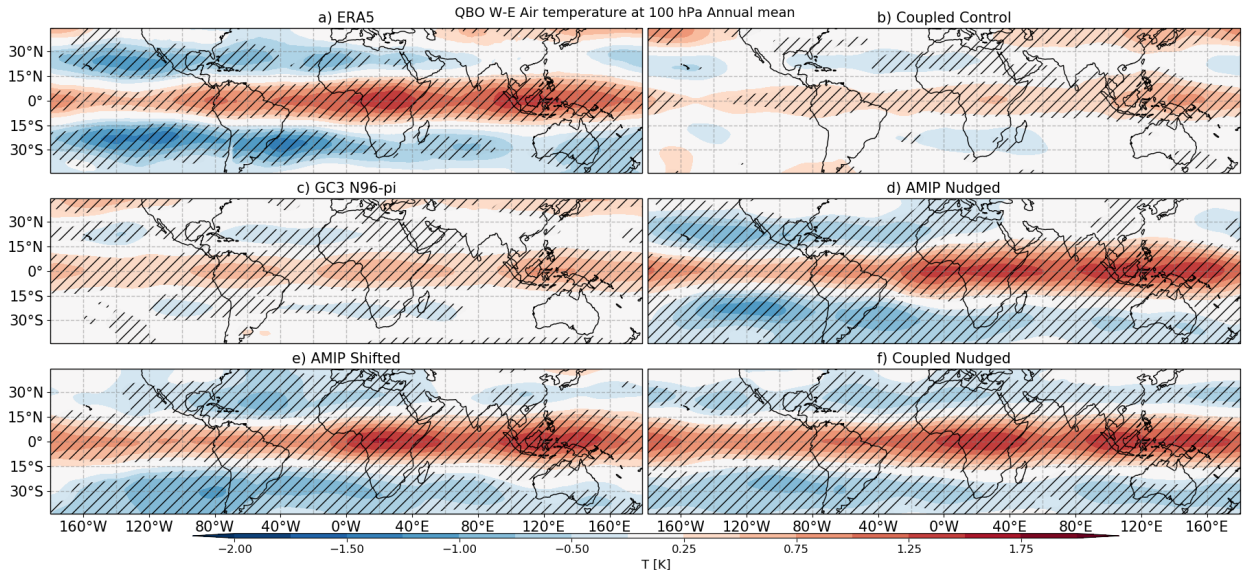


Figure 8.7: As in Figure 8.6, but for air temperature.

with the underlying SST field, rather with the QBO vertical wind shear, which has been improved by nudging. Results found in this analysis also indicate that the tropopause height and temperature exhibits more variability associated with the QBO than in the free-running model (not shown).

This section shows that the UTLS temperature and zonal wind variability are more

realistic in the nudged experiments, and that this variability is not related to the underlying SSTs but rather a result of the relaxation in the equatorial stratosphere. These results indicate that these experiments are suited to investigate tropical teleconnections associated with the QBO. The hypothesis to test is that the processes that link the QBO to tropical convection should be more realistically represented in the nudged experiments than in the control experiments.

8.3.2 Atmosphere-only experiments

This section describes the results of the atmosphere-only experiments: AMIP Nudged, AMIP Control and AMIP Shifted. These simulations use the CMIP6 SST dataset used for AMIP experiments, so that, the SSTs in these runs follow the observed seasonal and interannual variability of SSTs. The effect of nudging on the tropical circulation is first described to evaluate whether nudging has significantly modified the mean state of the Hadley and Walker circulations. Then, the precipitation response to the QBO is compared between Nudged and Control AMIP simulations.

The tropical circulation

The mean state of the Hadley cell in the atmosphere-only configuration is weaker than in ERA5 in the 20°S-0 region (the southern hemisphere branch in Figure 8.8) whereas biases in the upper-level tropical and subtropical troposphere, the model shows an easterly bias. The AMIP Nudged simulation shows an improvement of this bias in the tropical and subtropical stratosphere showing positive zonal wind differences with the Control experiment in the UTLS region, i.e, correcting the easterly biases of the Control experiment. However, no significant differences in the streamfunction over the tropical troposphere are observed. Similarly, no significant differences were found in the mean-state of the Hadley circulation between the Nudged and Shifted experiments, suggesting that the variability of the nudging data is of secondary importance relative to the mean state of the nudging data.

In turn, the Walker circulation biases in the upper troposphere are notably improved in the Nudged experiment (Figure 8.9). The mean state of the Walker circulation is weaker in the AMIP Control simulation compared to ERA5, characterised by a weaker circulation

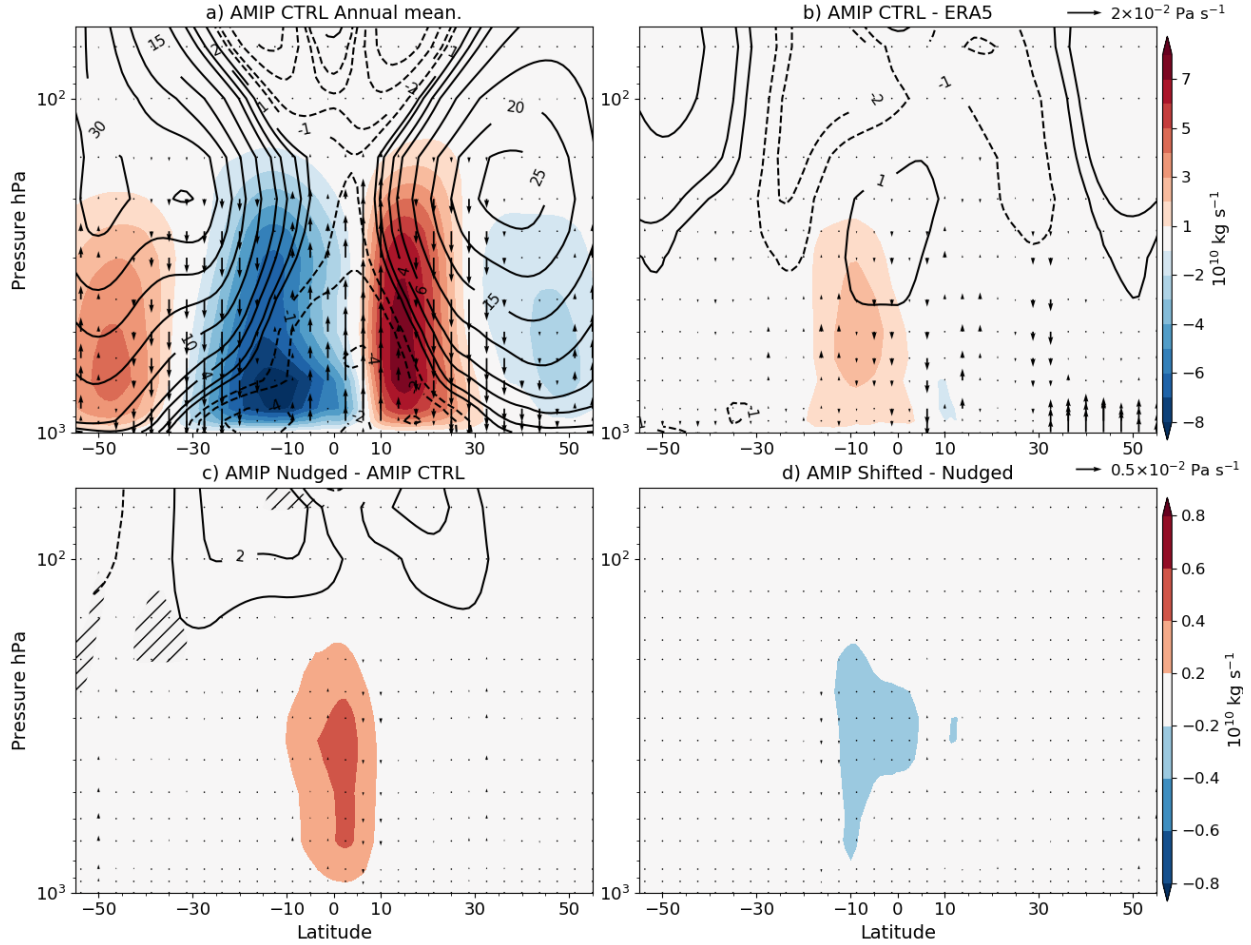


Figure 8.8: Hadley cell meridional mass streamfunction (shading), zonal mean zonal wind (contours in m s^{-1}) and vertical velocity (vectors). (a) Climatological mean in the AMIP Control experiment, (b) Bias in the Control experiment with respect to ERA5, differences between (c) AMIP Nudged-Control and (d) AMIP Shifted-Nudged. Note that the colorbar and scale of the vectors changes from the top to the bottom row. In (c-d), significant differences (95% confidence level according to a Mann-Whitney two-sided test) in the streamfunction are highlighted with hatching .

in the Western Pacific and an easterly bias at upper levels. These two tropospheric biases in the Control experiment are reduced in the Nudged experiments, even though the relaxation is only applied above 90 hPa significant differences in the zonal wind and zonal streamfunction are observed at 200 hPa near the dateline, over South America and over the Atlantic Ocean. However, no significant differences are observed between the AMIP Shifted and Nudged experiments.

The mean state of the Hadley and Walker circulation at upper levels is modified in the simulations when nudging is applied, reducing the biases in the circulation within

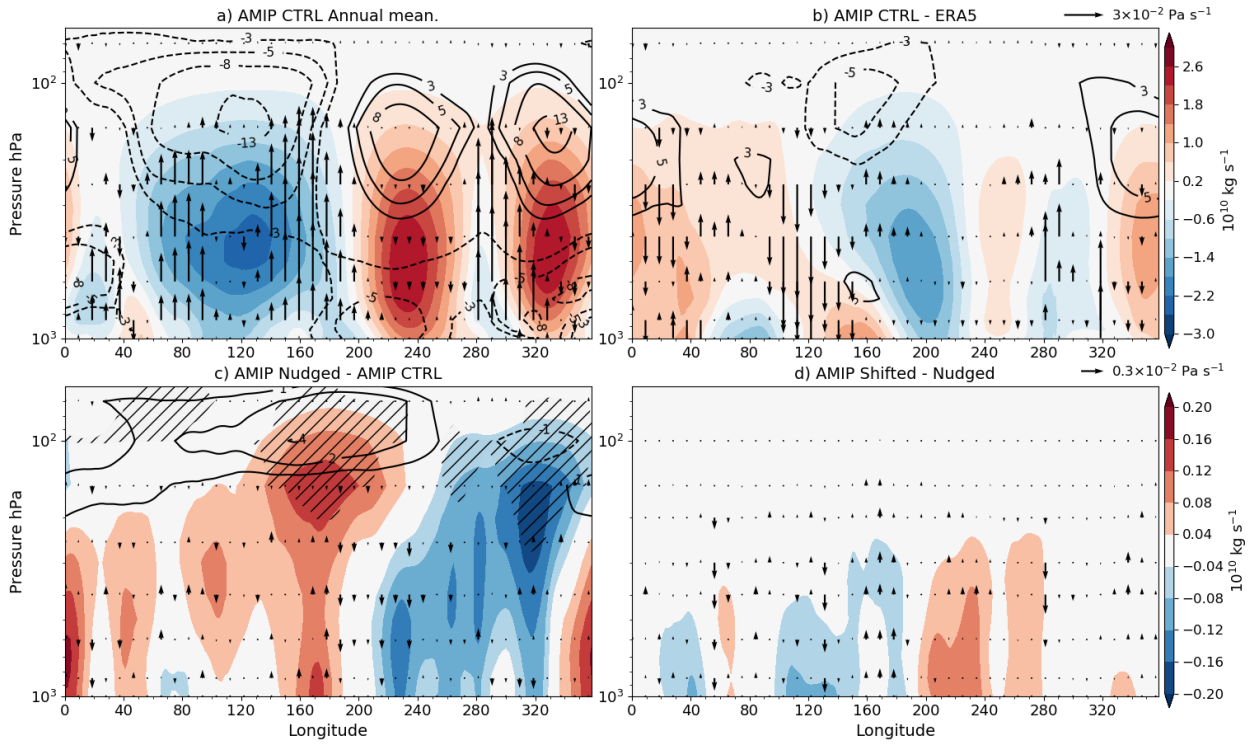


Figure 8.9: Zonal mass streamfunction (ψ in shading), zonal mean zonal wind (contours) and vertical velocity (vectors) averaged over the 10°S - 10°N , as in Figure 8.8.

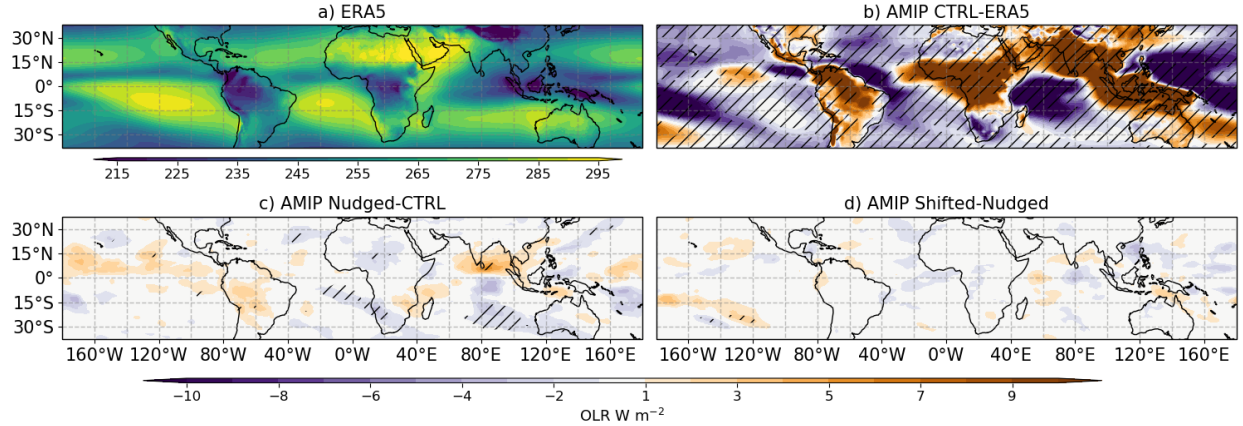


Figure 8.10: (a) Climatological mean OLR [W m^{-2}] in ERA5, (b) climatological biases in the AMIP Control simulation. (c) Differences between AMIP Nudged and Control and (d) between AMIP Shifted and Nudged. Significant (95% confidence level) differences according to a Mann-Whitney U test in (c, d) are highlighted with hatching.

the model. However, these differences, or reductions of the biases, are smaller than the magnitude of the biases themselves, so it is unclear whether these differences are large enough to improve other aspects of tropical climate.

For example, Figure 8.10 shows the biases in the climatology of OLR, and the impact

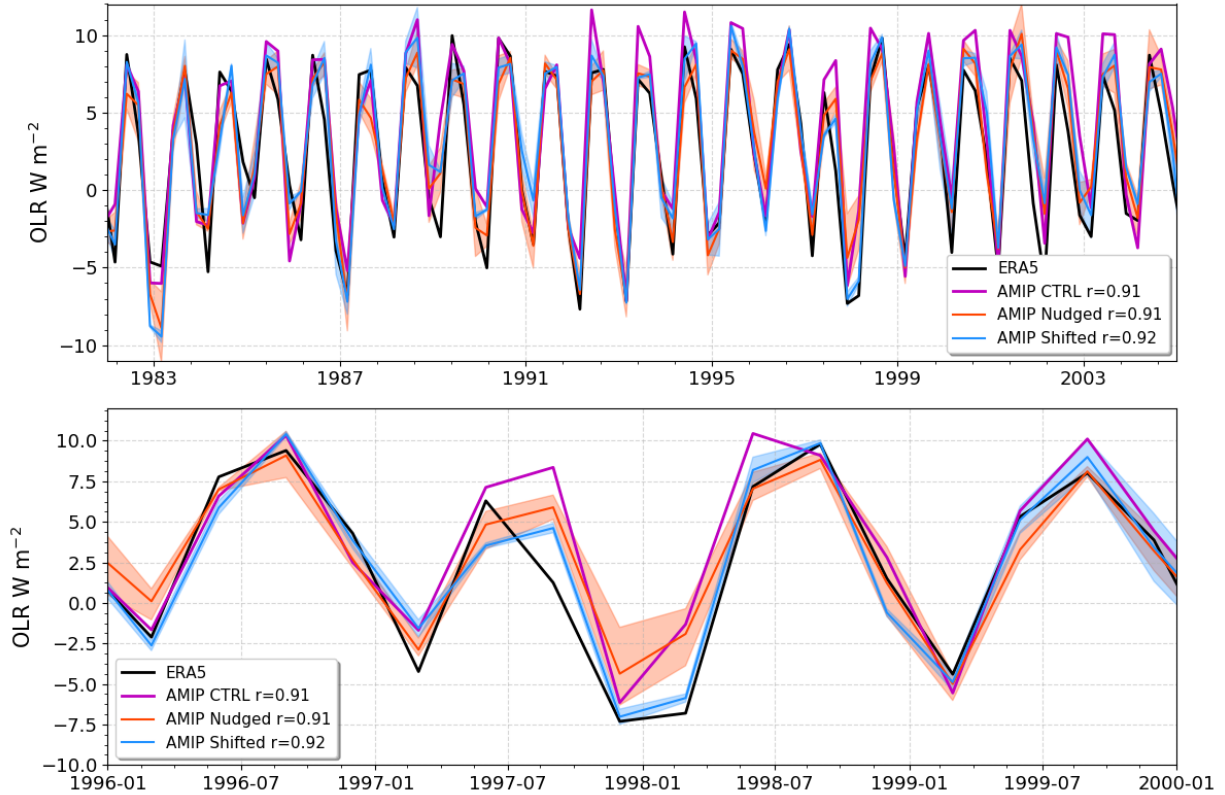


Figure 8.11: Time-series of zonal-mean equatorial [5°S - 5°N] OLR in ERA5 and the three amip experiments for (a) 20 yrs and a (b) 5-yr period around the 1997-1998 ENSO event. For each AMIP experiment the Pearson correlation coefficient between the experiment time-series and ERA5 is shown in the legend.

of Nudging on these biases. Most regions in the tropics exhibit significant and relatively large biases in AMIP Control compared to ERA5, most of which remain unchanged in the AMIP Nudged and Shifted experiments. The small and not significant differences between the two types of nudged experiments suggest a small effect of the relaxation of the zonal winds over the mean state of OLR.

Similarly, Figure 8.11 shows that the zonal-mean OLR time-series averaged over the deep tropics is undistinguishable between the three AMIP experiments, and the time-series of all the experiments have the same correlation coefficient with ERA5. In other words, the tropical mean OLR remains unchanged in the nudged experiments, regardless of whether the relaxation was implemented to match the SST field or whether the nudging data was shifted from the SST time-series. Based on these results alone, it would appear that nudging has made little impact over the interannual variability of the tropical mean OLR. The

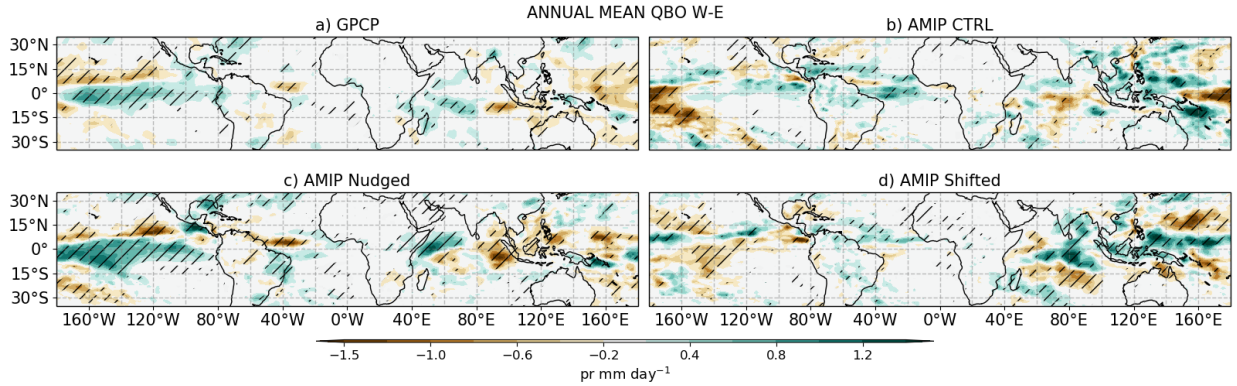


Figure 8.12: Annual-mean precipitation response (QBO W-E) in (a) GPCP, and atmosphere-only experiments: (b) AMIP CTRL, (c) AMIP Nudged and (d) AMIP Shifted.

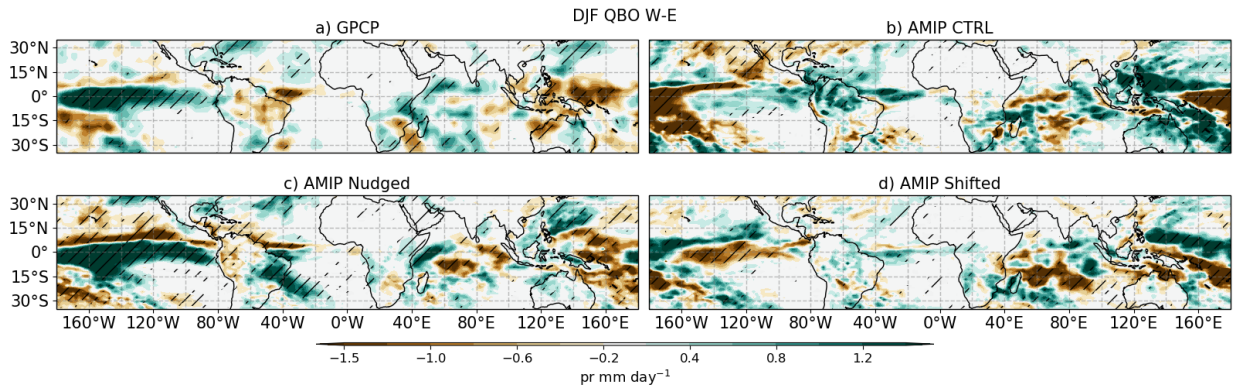


Figure 8.13: As in Fig. 8.12 but for the DJF season.

question of whether the specific variability of OLR and precipitation associated with the QBO is also the same is now investigated in the next section.

Precipitation response to the QBO

The annual-mean difference of precipitation between QBO W and E phases (Fig. 8.12) in the ensemble-mean AMIP Nudged experiment matches closely the results of GPCP, characterised by an El Niño pattern in the Pacific Ocean, a weaker Atlantic ITCZ and a gradient of precipitation in the Indian Ocean during QBO W compared to QBO E. In contrast, the free-running AMIP Control and the simulations with an out-of-phase relaxation of the winds with respect to the SST driving data (AMIP Shifted) show very different responses to the AMIP Nudged experiment and observations.

A similar result is found when the composite differences only include DJF (Fig. 8.13),

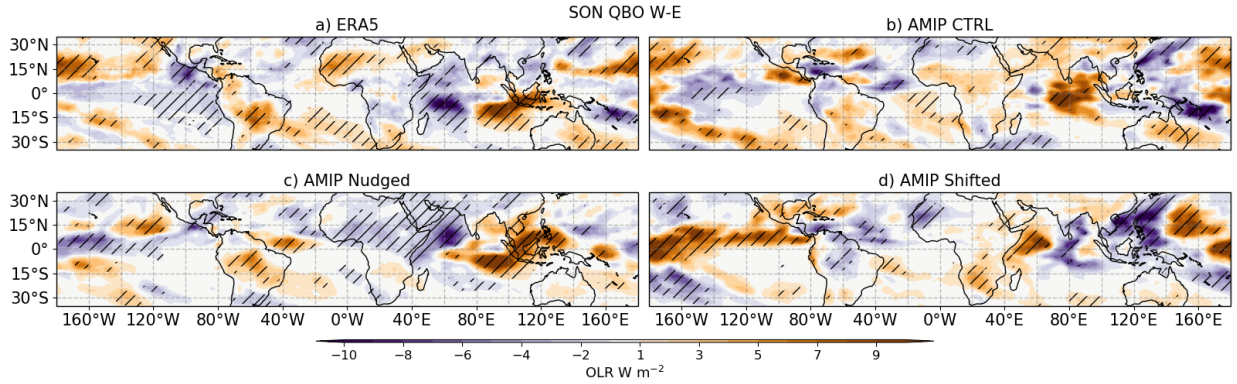


Figure 8.14: As in Fig. 8.12 but for OLR in the SON season.

so that the precipitation response in the simulations where the QBO index and the SSTs match exactly as in observations (AMIP Nudged) produce a very similar response to GPCP, whereas simulations where the QBO winds do not match the same SSTs result in different responses. Results using OLR are very similar, for example, Figure 8.14 shows that a strong response is diagnosed in GPCP in the Indian Ocean which is reasonably reproduced in AMIP Nudged but AMIP CTRL and AMIP Shifted exhibit a very different response in the Indian Ocean and elsewhere.

These results suggest that the QBO winds are secondary to the effect of the SSTs for the precipitation response in these atmosphere-only experiments. The AMIP Shifted experiment has a better representation of the stratospheric variability in temperature and vertical wind shear, however, the response is entirely different to the AMIP Nudged experiments, the difference between these two experiments being the underlying SSTs. These results suggest that improving the representation of the QBO is not enough to replicate the observed response because the SST forcing dominates.

This section shows, first, that relaxing the zonal wind in the stratosphere in atmosphere-only experiments does not modify the mean state of the tropical circulation. Second, that the surface response of precipitation associated with the QBO in observations is largely associated with the underlying SSTs. The tropical mean OLR and precipitation mean state appear to be undistinguishable between Control, Nudged and Shifted experiments, whereas the composite differences between the two phases of the QBO reveal that the observed precipitation response is associated mostly with the SST anomaly pattern. However, whether the QBO

has any effect over the SSTs cannot be answered in this atmosphere-only experiments, which leads to the next section which analyses the coupled nudged experiments.

8.3.3 Coupled experiments

This section presents the results of the coupled ocean-atmosphere experiments with (Nudged) and without (Control) relaxing the zonal wind in the tropical stratosphere. Note that all the individual experiments in this section are the same length (35 yr) and the Coupled Nudged ensemble-mean refers to the mean results of the six ensemble members with nudging. These coupled experiments differ only slightly from the setup used in the CMIP6 piControl experiments, analysed in section 7.3, with the atmospheric resolution of the nudged experiments matching the resolution of GC3 N96-pi and the oceanic resolution of these resolutions being the same of GC3 N216-pi. The forcing is constant in both types of runs, except that in the piControl experiments, the forcing represents conditions of the year 1850 and in the nudged experiments of the year 2000. Due to these similarities, we compare the long-term CMIP6 experiments with the nudging experiments in some instances.

SST response

The previous section shows that in atmosphere-only experiments the SST forcing dominates over any effect of the nudging, indicating that the mechanism by which the QBO influences tropical climate involves the SSTs. In the coupled ocean-atmosphere experiments, the SSTs are able to respond and interact with any atmospheric forcing, and for that reason, this section first presents the annual mean and seasonal mean differences between the two phases of the QBO comparing coupled nudged and control experiments.

The annual mean difference in tropical SSTs between QBO phases in HadSST and each coupled experiment is shown in Figure 8.15. In the HadSST dataset, the differences indicate a warmer East Pacific, and equatorial Atlantic and Indian Oceans. The first control experiment shows a very similar response in the Pacific and Indian Oceans whereas the results of the second control experiment only agree with the HadSST results in the subtropical North Atlantic and in the Western Pacific. The nudged experiments, in turn, show a number of

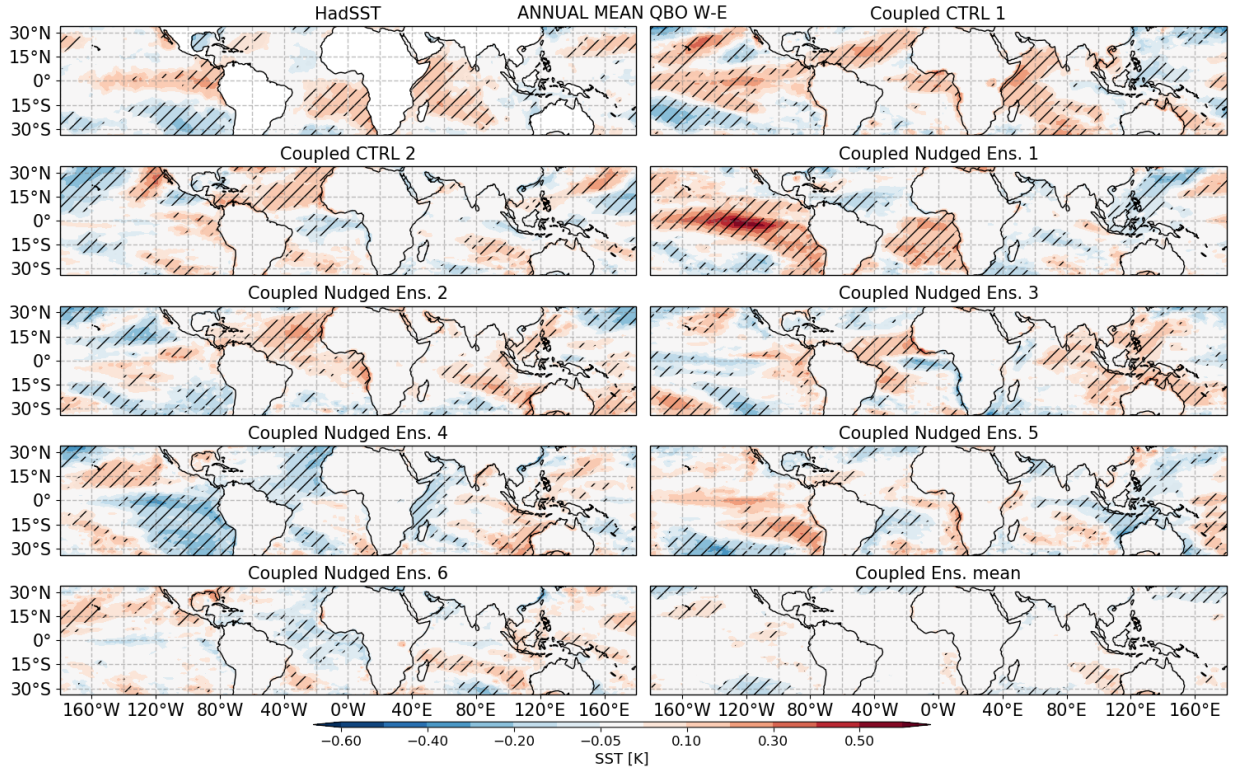


Figure 8.15: Annual mean SST [K] QBO W-E differences in the HadSST dataset and the Coupled Control, Coupled Nudged ensemble members and the Coupled Nudged ensemble mean. Hatching denotes significance to the 95% confidence level according to a bootstrapping with replacement test.

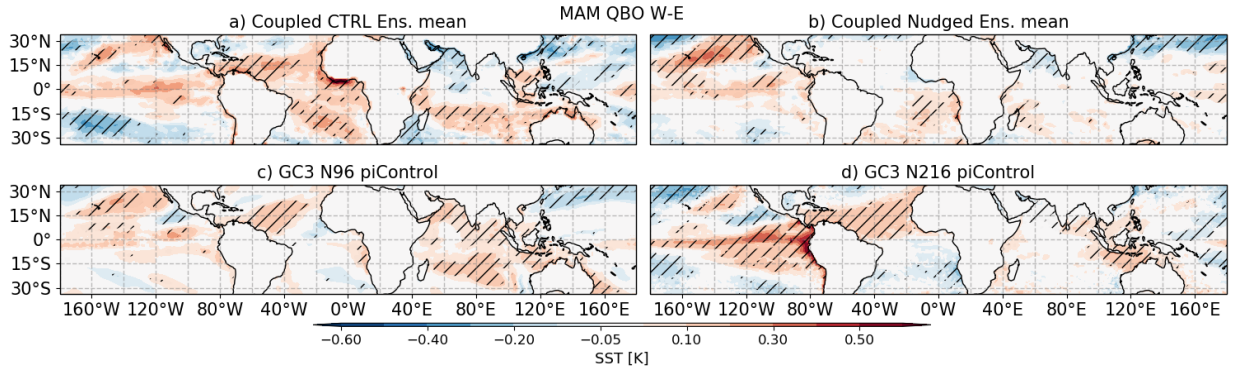


Figure 8.16: SST differences between QBO phases in MAM in (a) Coupled Control ensemble mean (2-member), (b) Nudged Coupled ensemble mean (6 members) and in the CMIP6 (c) GC3 N96-pi and (d) GC3 N216-pi.

different responses, with differences being significant and positive in some regions in one ensemble and of another sign and unsignificant in other ensembles.

The ensemble-mean response shows that averaging over all ensembles results in a weak

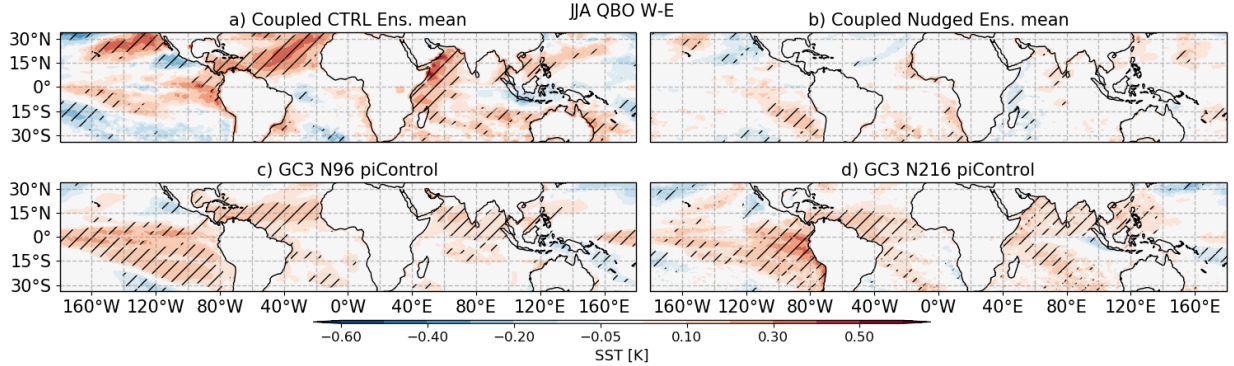


Figure 8.17: As in Fig. 8.16 but for JJA.

mean response, with only some differences being different than zero and significant, for example the positive differences found over the coast of Australia and the subtropical Central Pacific. In specific seasons, such as MAM (8.16), the SST response also appears to be stronger in the tropics in the free-running Coupled Control experiments than in the nudged experiments. In MAM, a positive difference found in the Atlantic, Indian and Pacific Oceans in the CMIP6 experiments is also found in the control experiments but this response is weaker in the ensemble-mean of the nudged experiments. The nudged experiments show a relatively large difference in the eastern subtropical Pacific reaching the coast of California, in agreement with the control experiments.

The pattern of positive anomalies in the equatorial Central and Eastern Pacific, as well as in the Atlantic Ocean, appears in the control and CMIP6 experiments in most months. In boreal summer (Fig. 8.17), the patterns are particularly strong in the Coupled Control ensemble mean in the Atlantic and Indian Oceans. However, the Nudged experiments show a very weak mean response in the tropics, only a warm difference found in the western coast of South America. For the other seasons, SON and DJF, similar results are found (not shown) in which the ensemble mean of the control experiments agrees well with the CMIP6 experiments, whereas weaker responses are found in the nudged experiments.

These results suggest that the SST response to the phase of the QBO in the nudged experiments is not significantly larger in the experiments compared to the control or the CMIP6 experiments, especially in equatorial regions. In other words, the simulations with a stronger temperature signal associated with the QBO show the seemingly weakest response

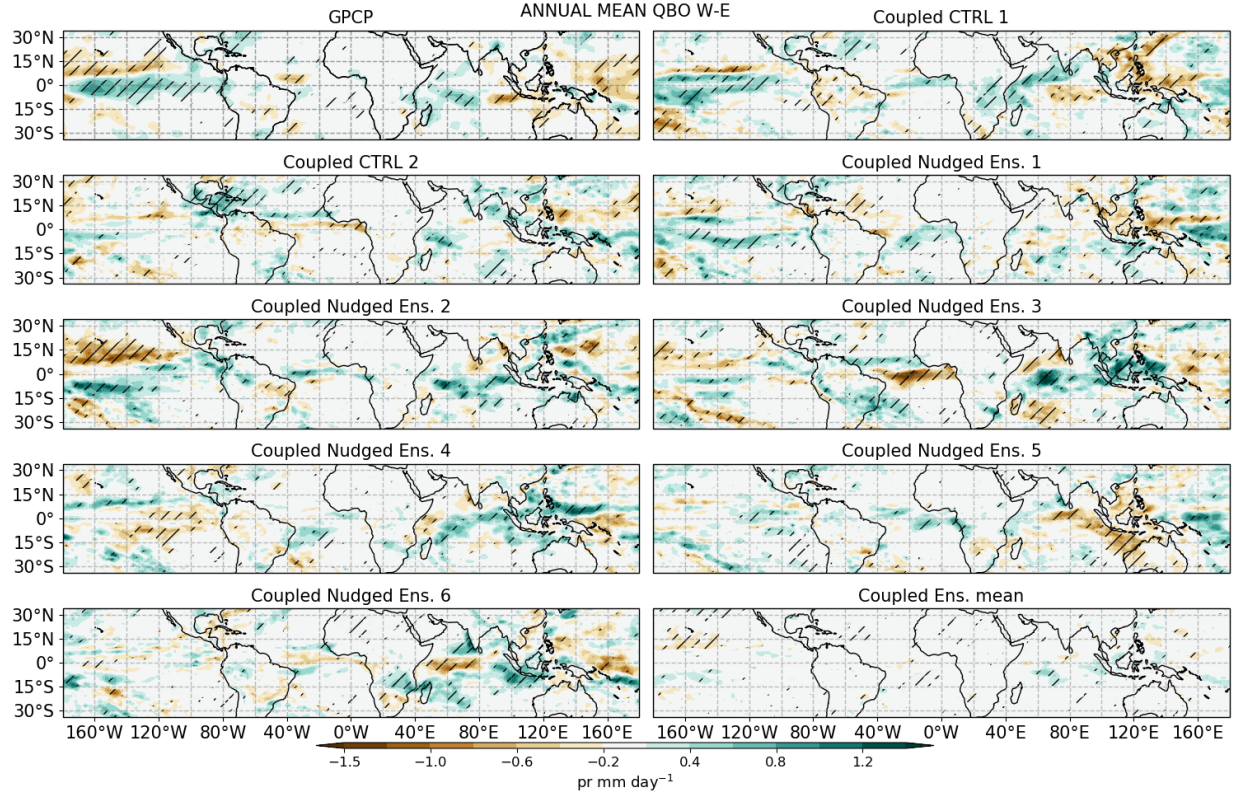


Figure 8.18: Annual mean precipitation QBO W-E differences in GPCP, Coupled Control, Coupled Nudged ensemble members and the Coupled Nudged ensemble mean. Hatching denotes significance to the 95% confidence level according to a bootstrapping with replacement test.

to the phase of the QBO. The lack of robust and large patterns of SST anomalies suggests that the precipitation response may also be weaker in the ensemble mean of experiments with nudging, which is the topic of the next section.

Precipitation response

The annual mean difference between QBO phases (Fig. 8.18) in each coupled experiment reveals a strong variability of the precipitation response, suggesting an important role of long-term variability for these responses. In particular, the control experiments show two significant responses: the first control experiment shows a significant El Niño-like response over the Central and Eastern Pacific Ocean, whereas the second control experiment shows a northward shift of the Atlantic ITCZ and a wetter Caribbean Sea. Precipitation differences in the Indian Ocean and continent are also significant in both of these two coupled

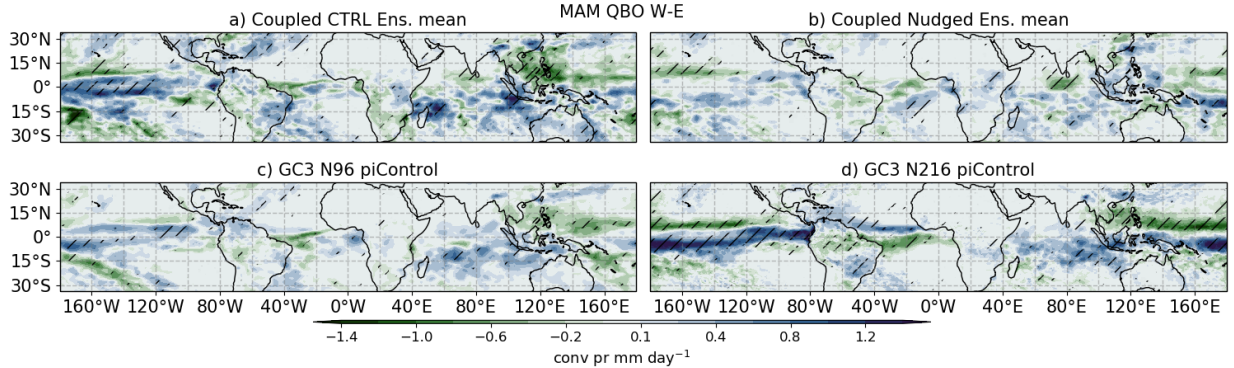


Figure 8.19: As in Fig. 8.16 but for convective precipitation.

experiments, even though the pattern and magnitude of the difference is not a close match, both simulations suggest a wetter western Indian Ocean and continent. Note that these three responses found in the Coupled Control experiments in this setup were also observed over the longer GC3 N96 and N216-pi experiments, described previously in this chapter.

The nudged experiments show various different responses (Fig. 8.18), with several regions showing significant responses of one sign in one ensemble member and another, also significant, response of an opposite sign in a different ensemble just as in the SST differences of Figure 8.15. In most ensemble members, the stronger responses are seen over the ocean rather than over land. The nudged ensemble mean shows regions with a significant response but the difference value in significant regions is too small to be represented by the colorbar, indicating a weak response.

The differences in a specific season are also relatively weak in the ensemble mean of the nudged experiments. For instance, in boreal spring, the differences in convective precipitation (Figure 8.19) show a wetter equatorial Pacific and a drier band at 10°N during QBOW than E in the control ensemble mean and CMIP6 experiments, whereas the nudged experiments only show the dry response. The Coupled Control ensemble mean and CMIP6 experiments also show agreement on the sign and pattern of the response in the Western Pacific and Indian Ocean, characterized by dry anomalies in the Western Pacific ITCZ, the Philippines and the South China Sea, whereas wetter anomalies are observed in the Indian Ocean. In contrast, the composite mean results in the nudged experiments show unsignificant responses in these above mentioned regions.

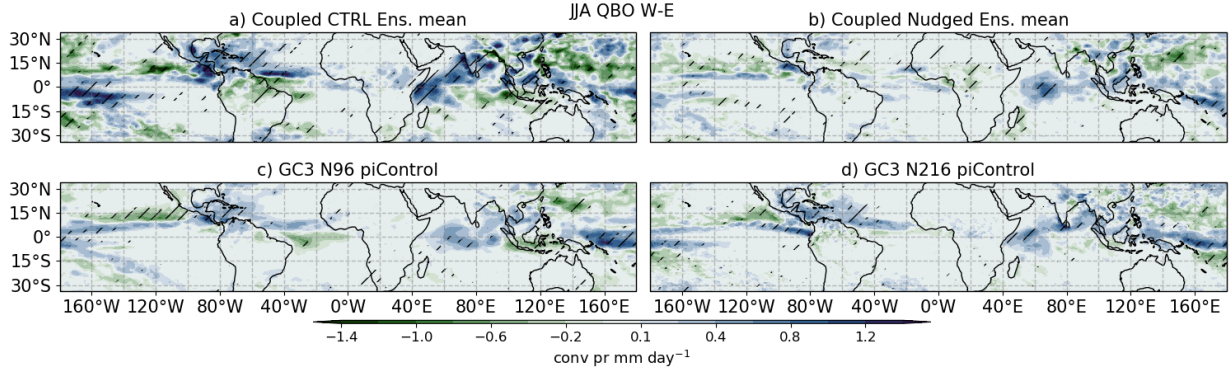


Figure 8.20: As in Fig. 8.19 but for JJA.

In other seasons, the control experiments also match the results of the CMIP6 experiments, whereas the nudged experiments show a weaker or no response. For example, in boreal summer (Fig. 8.20) the CMIP6 experiments and Coupled Control experiments show a northward shift of the Atlantic ITCZ, a wetter Caribbean Sea and Indian Oceans and a drier eastern Pacific. The nudged experiments are in reasonable agreement in the Indian Ocean, indicating wetter conditions during QBO than E. Similarly, the effects over the Indian Ocean in SON found for the CMIP6 experiments in section 7.3, are also seen in the Coupled Control experiments, but not in the nudged experiments (not shown).

The results of the precipitation response agree with the previous results that analysed the SST differences. There is no evidence that the nudged experiments result in a stronger surface response to the phase of the QBO, even though the UTLS temperature variability associated with the QBO has been increased and improved in the nudged experiments. However, whether the mean state and variability of the tropical circulation has been modified could offer an explanation to these results.

Tropical circulation response and the IOD

The variability of the tropical circulation in the atmosphere-only experiments was found to be dominated by the SST forcing in the previous section. However, to the mean state of the upper-level branch of the Walker circulation was slightly different in the AMIP Nudged experiments compared to the Control. To understand whether similar changes to the mean state or variability of the tropical circulation are observed in the coupled

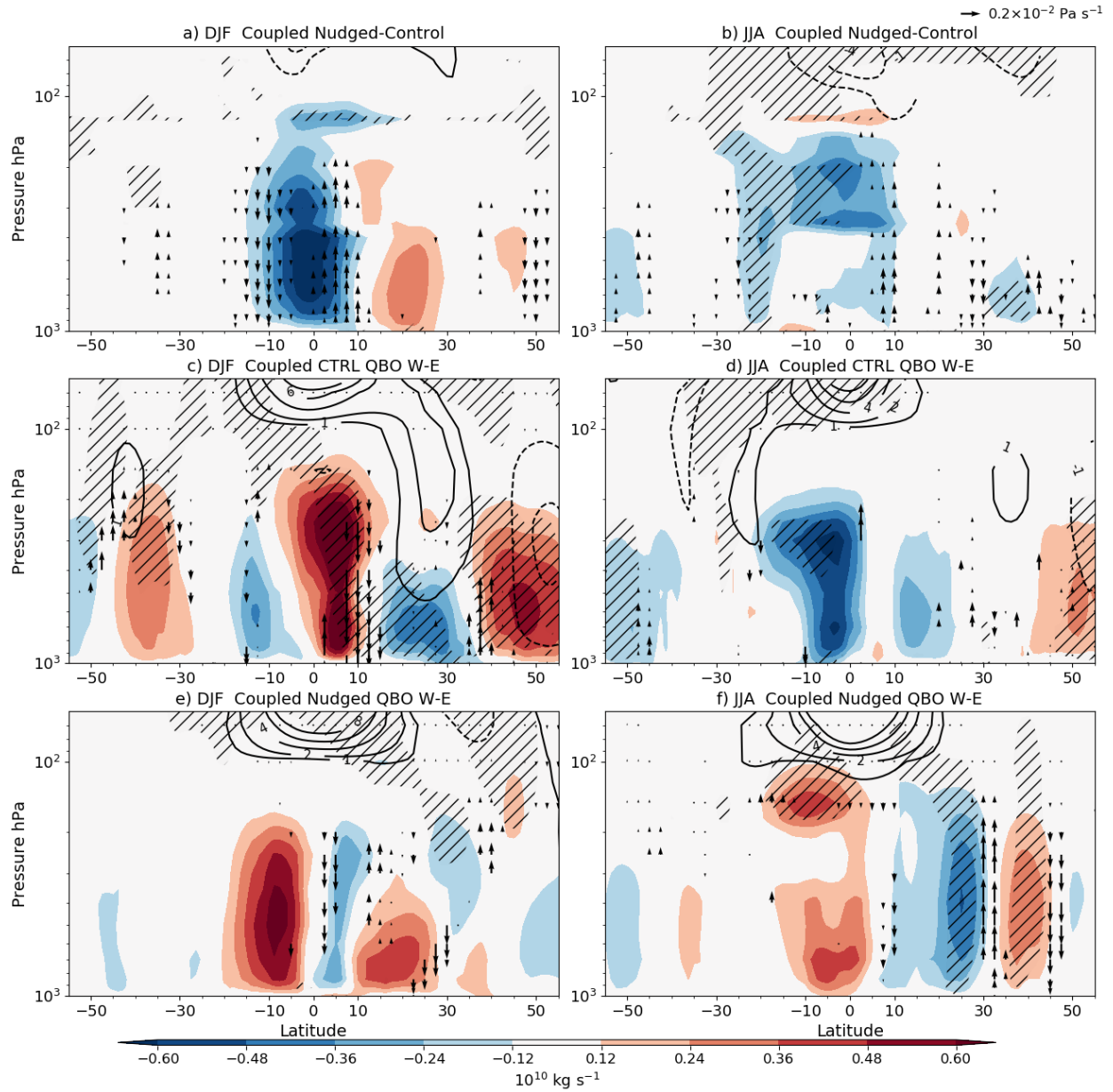


Figure 8.21: Hadley circulation differences in meridional mass streamfunction (shading), zonal wind (contours) and vertical velocity (vectors). (a, b) show the seasonal mean differences between Nudged and Control experiments in (a) DJF and (b) JJA. (c-f) show the QBO W-E differences for the (c-d) Control and (e-f) Nudged experiments for (c,e) DJF and (d,f) JJA. In all panels, hatching denotes significant differences in the streamfunction to the 95% confidence level according to the bootstrapping method, whereas for the zonal wind and omega, only significant differences are shown.

experiments, Figures 8.21 and 8.22 show the impact of nudging on the mean state and variability of the Hadley and Walker circulations, respectively.

The nudging appears to modify the mean state of the Hadley circulation in both

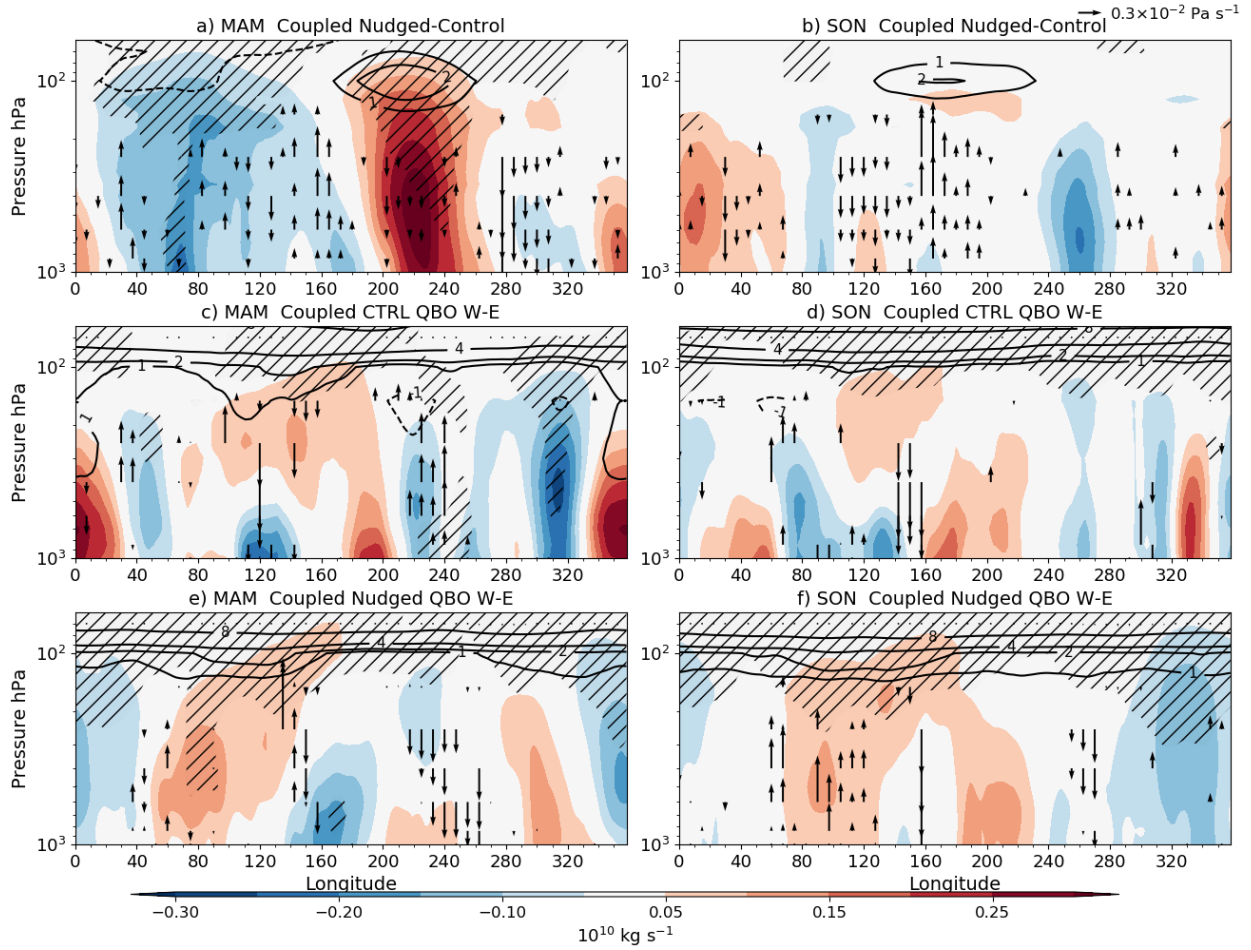


Figure 8.22: Walker circulation differences in zonal streamfunction (shading), zonal wind (contours) and vertical velocity (vectors). (a, b) show the seasonal mean differences between Nudged and Control coupled experiments in (a) MAM and (b) SON. (c-f) show the QBO W-E differences for the (c-d) Control and (e-f) Nudged experiments for (c,e) MAM and (d,f) SON. In all panels, hatching denotes significant differences in the streamfunction to the 95% confidence level according to the bootstrapping method, whereas for the zonal wind and omega, only significant differences are shown.

DJF and JJA seasons (Figure 8.21). Significant changes in the tropical UTLS streamfunction are observed in both seasons, and in DJF changes to the vertical velocity in the tropics suggest a strengthening of the Hadley cell when nudging is applied but very small changes are observed in JJA.

The difference QBO W-E in the tropospheric state of the Hadley cell in both seasons is considerably different between Nudged and Control experiments (Figs. 8.21c-f). In DJF, the Nudged ensemble-mean shows anomalous descent over the 10°N latitude band and significantly higher values of the streamfunction at the equator extending into the lower

troposphere. Similarly, the zonal wind in this season shows a positive anomaly extending as far down as 500 hPa at 20–30°N, indicative of changes to the sub-tropical jet position and strength, documented previously (e.g. Garfinkel and Hartmann, 2010).

Even though the Nudged experiments show stronger zonal wind anomalies in the equatorial stratosphere in both seasons, the response of the northern hemisphere subtropical jet is not observed, and the differences in the streamfunction and vertical velocity appear opposite to that of the Control experiments in DJF. The same contrast is observed in JJA, with the Control and Nudged experiments exhibiting very different responses. Notably, the streamfunction and vertical velocity in the Nudged experiments in this season shows a dipole signal in the Northern Hemisphere with positive and negative anomalies indicating anomalous ascent at 30°N and descent at 50°N.

The mean Walker circulation is also affected by the nudging (Fig. 8.22). As in the AMIP experiments, the upper-level zonal wind and streamfunction is modified by the nudging, only that in the coupled experiments, significant differences are observed in the lower troposphere over the Indian Ocean and the Eastern Pacific. In the UTLS region above the Indian and Pacific Oceans, the nudging is forcing the zonal wind towards ERA5, thus reducing the biases in the model (see e.g. Figure 4.13). In other words, not only biases in the variability of the zonal winds in the lower stratosphere are alleviated by the nudging but also the mean state of the upper-level branch of the Walker circulation. However, the latter may also mean that the variability of the Walker circulation is overconstrained when nudging is applied.

The response of the Walker circulation to the QBO is different in nudged versus control experiments (Fig. 8.22c-f). While in MAM, the control results suggest a weaker state of the Walker circulation or an El Niño-like pattern with anomalous ascent in the Eastern Pacific, the nudged simulations show the opposite. In turn, in SON, while the control experiments show anomalous ascent in the western Indian Ocean, the nudged experiments show ascent over the eastern Indian Ocean.

The nudging appears to modify the mean state and variability of the tropical circulation to a certain extent. However, the differences shown in Figures 8.21 and 8.22 are relatively small compared to the climatological values, but clearly some of these differences are still significant.

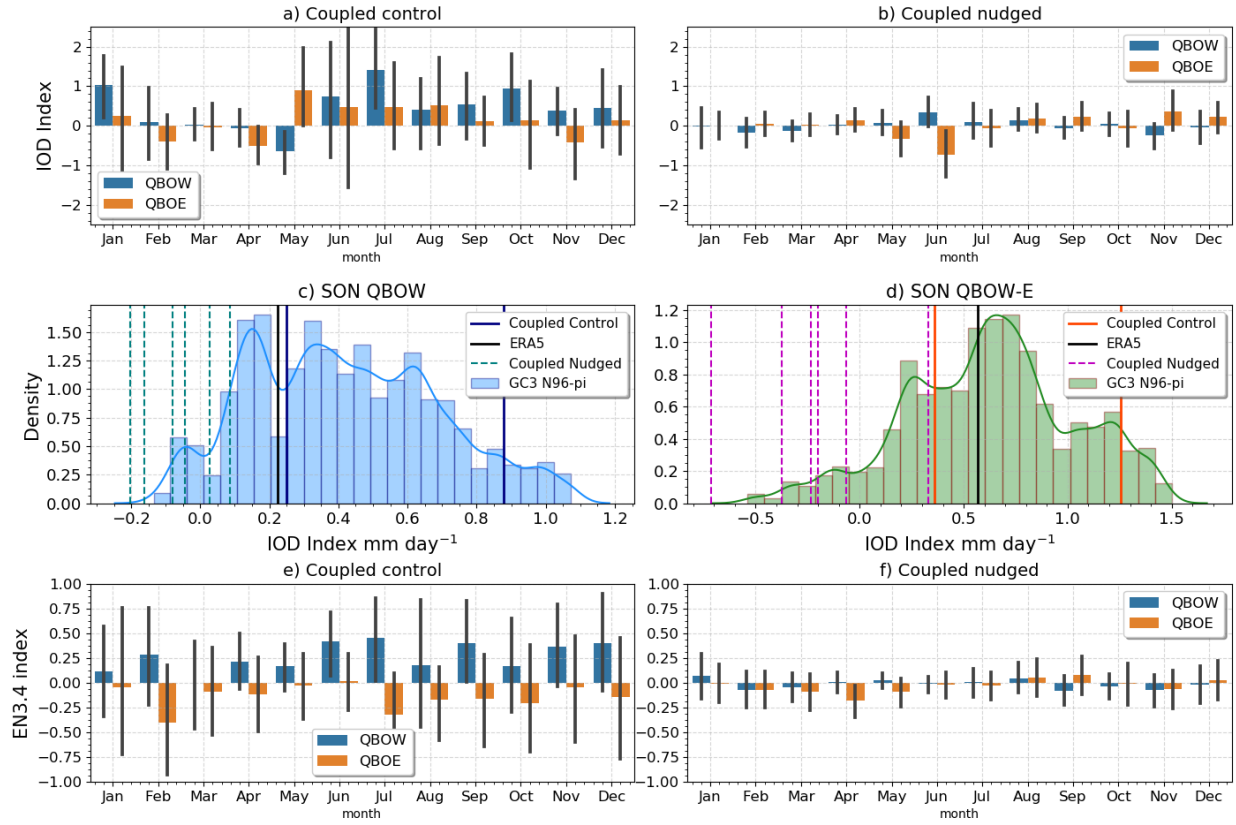


Figure 8.23: (a, b) Monthly-mean IOD convective precipitation index [mm day^{-1}] in coupled (a) control and (b) nudged ensemble-means separated by QBO phase. (c, d) Probability density functions (PDFs) of the IOD convective precipitation index for (c) the mean SON during QBOW months and (d) the SON difference between QBO W-E. The PDF is obtained from the 500 yrs of the GC3 N96-pi by bootstrapping 10,000 times into 35-yr periods and obtaining the averages and differences in each subsample. The mean indices for the Coupled Control and Nudged experiments, as well as for ERA5 are also shown. (e, f) Monthly-mean EN3.4 index [K] in the ensemble mean (e) Coupled control and (f) Coupled Nudged simulations separated by QBO phase.

Results in a previous section demonstrated that in the CMIP6 pre-industrial control experiments a statistically significant relationship is found between the IOD and ENSO, and the QBO (Fig. 7.13). Positive events of the IOD and ENSO are more commonly found during QBOW than E, and a convective precipitation index of the IOD and the SST EN3.4 index are also positive during QBOW and negative during QBOE. Figure 8.23 revisits these relationships in the coupled experiments.

The mean IOD index is positive during QBOW and negative during QBOE in the Coupled Control ensemble in boreal fall and early winter (Fig. 8.23a), in agreement with results from the CMIP6 experiments. In contrast, the mean IOD index is close to zero in the Coupled

Nudged ensemble without any clear relationship between the index and the QBO phase in any month (Fig. 8.23b). These results suggest that no consistent relationship is found across the six ensemble members where nudging was applied in the simulation. However, these results may simple be due to sampling of the ocean-atmosphere state used for the nudged experiments, in other words, possibly due to decadal variability in the GC3.1 configuration.

For that reason, the CMIP6 GC3 N96-pi is used to investigate whether the results of the Nudged and Control experiments are also seen in periods of similar length in that long 500 yr simulation. While this comparison is not perfect due to differences in ocean resolution and forcing, the model setup and parametrisations, and atmospheric resolution is otherwise the same between GC3 N96-pi and these experiments. The simulation is repeatedly sampled at random for 35 yr continuous periods, and the SON IOD index is computed each time to construct a probability distribution.

Figure 8.23c shows that the IOD index during QBOW in GC3 N96-pi is more frequently positive, as shown in the previous section, but in some 35-yr periods a negative mean index during QBOW can be observed in this simulation. The two Coupled Control simulations and ERA5 show a positive mean IOD index during QBOW whereas four out of the six Coupled Nudged simulations show a negative index.

The previous section showed not only that positive IOD indices and events are more frequent during QBOW, but also that the opposite is true for QBOE. Figure 8.23d shows that the difference in the IOD index during SON between the two QBO phases is most frequently positive in GC3 N96-pi. Results from ERA5 and the two Coupled Control simulations also show a positive difference of 0.6 mm day^{-1} for the reanalysis and up to 1.3 mm day^{-1} for one of the control simulations. In contrast, the nudged experiments are found to the left of the mean of the PDF of GC3 N96-pi and the mean of the Control experiments, with a mean negative values in most ensemble members the mean of one member is found to the leftmost end of the PDF.

Finally, the ENSO index is found to be positive in the Control experiments but no robust relationship is found in the Nudged experiments. As with the CMIP6 experiments, the Coupled Control EN3.4 index is positive during QBOW and negative during QBOE throughout most of the year. However, there seems to be no relation between the QBO

and the EN3.4 index in the nudged experiments. Overall, these results suggest that the relationships between the QBO and the IOD and ENSO observed in the CMIP6 or Control experiments are not found in the Nudged experiments, which show little-to-no relationship between these two indices and the QBO phase.

8.4 Summary and discussion

Evidence of tropical teleconnections associated with the QBO are difficult to understand in observations due to the relatively large observational uncertainty and the influence of ENSO. In models, biases in the QBO also complicate the investigation of how the QBO modifies the tropical circulation and the surface, largely because the key aspects of the QBO that are hypothesized to be influential for stratospheric-tropospheric coupling in the tropics are poorly represented by most models. For these reasons, this chapter investigates the influence of the QBO over tropical climate through nudging experiments using the MOHC UM.

The nudging technique results in simulations that exhibit a more realistic representation of the variability of the QBO winds and temperature in the lower stratosphere. In other words, the nudging experiments simulate a stronger response of the UTLS temperature to the QBO. However, in the atmosphere-only setup, the nudging does not seem to significantly modify the variability of precipitation and OLR as the SST variability imposed dominates.

In the coupled experiments, the control simulations largely agree with the results found in the first part of the chapter using the CMIP6 versions of the model. However, in the nudged experiments, the tropical SSTs and precipitation show no consistent difference between the QBO phases across the ensemble-mean. Further evidence in this part of the chapter confirms that there is no indication that the nudging has made the response to the QBO stronger, or indeed closer to the observed response and in any case, the nudging appears to have dampened the surface response.

One explanation for the nudged results may be that the static stability mechanism, the most cited mechanism in the literature (Collimore et al., 2003; Liess and Geller, 2012; Nie and Sobel, 2015; Gray et al., 2018; Lee and Klingaman, 2018), may not be the dominant factor that relates the QBO to the tropical surface. Specifically, in ERA5,

the temperature signal becomes very small at levels lower than 125 hPa, and the 1 K difference at 100 hPa may not be large enough to modify the static stability of the whole convective profile in a significant manner.

An alternative hypothesis is that by nudging we have modified the mean state of the Walker circulation, as was demonstrated in this chapter. Therefore, by nudging the teleconnections operating through the Walker circulation simulated by the model become different in the nudged experiments, either because of the relatively minor mean-state change or because Walker circulation-QBO feedbacks have been cut off by the relaxation. Related to this, another explanation could be that the relationships found in the free-running versions of the model are not due to a causal influence from the QBO downward (top-down) but rather a result of the influence of tropical convection on the phase of the QBO. Studies (e.g. Schirber, 2015; Christiansen et al., 2016) have shown that the tropical wave activity, largely modulated by ENSO, can influence the descent rate and season of phase change of the QBO. Perhaps then, the ENSO-QBO relationship found in the CMIP6 models is lost in the nudged experiments because the forcing of ENSO cannot influence the QBO.

Future work could improve from this chapter in several ways. Firstly, instead of doing a relaxation of the state of the model in any variable, an improvement of the representation of tropical waves associated with deep convection could simultaneously improve the representation of the QBO characteristics as well the teleconnections. One such example is seen in Serva et al. (submitted) which compares simulations with different gravity wave schemes resulting in different properties of the QBO but also precipitation responses in the tropics.

Secondly, the nudging was applied in a relatively coarse resolution configuration (N96) but the results may be different in a medium-resolution (N216) configuration due to the improvement in the tropospheric dynamics that was found in Chapter 4. Additionally, the relaxation in this chapter was done at all grid-points, due to model constraints, however, other types of nudging have been applied, for example by Martin et al. (2021) to the zonal-mean which may allow wave propagation into the stratosphere. Nudging in a zonal-mean sense using a model that can internally generate a reasonable QBO could provide more answers to some of the results in this chapter.